Photoluminescence and Raman spectroscopy of doped nanomaterials.

Fakultät für Chemie und Pharmazie
Institut für Physikalische und Theoretische Chemie

Dissertation
zur Erlangung des naturwissenschaftlichen Doktorgrades der Julius-Maximilian-Universität Würzburg

vorgelegt von

Florian Oberndorfer

aus Schweinfurt

Würzburg, 2022

Eingereicht bei der Fakultät für Chemie und Pharmazie am

.....

Gutachter der schriftlichen Arbeit

1. Gutachter: .....
2. Gutachter: .....

Prüfer des öffentlichen Promotionskolloquiums

1. Prüfer: .....
2. Prüfer: .....
3. Prüfer: .....

Datum des öffentlichen Promotionskollquiums:

.....

Doktorurkunde ausgehändigt am:

.....

Contents

List of abbrevations

1D	one-dimensional
2D	two-dimensional
3D	three-dimensional
BGR	band gap re-normalization
AO	atomic-orbitals
CCD	charge coupled device
CMOS	complementary metal-oxide-semiconductor
CNT	carbon nanotube
CoMoCat	cobalt molybdenum catalyst
CVD	chemical vapour deposition)
DC	direct current
DGU	density gradient ultracentrifugation
DOS	density of states
EPR	elctroparamagnetic resonance
TREFISH	timeresolved electric-field-induced second harmonic
F_4TCNQ	2,3,5,6-Tetrafluoro-7,7,8,8-tetracyanoquinodimethane
FWHM	full width at half maximum
HiPCO	high pressure carbon monoxide
HOMO	höchstes besetztes Molekülorbital (*engl.* highest occupied molecular orbital)
ITO	Indiumzinnoxid (*engl. indium tin oxide*)
LUMO	niedrigstes unbesetztes Molekülorbital (*engl.* lowest unoccupied molecular orbital)
MWNT	mehrwandige Kohlenstoffnanoröhre (*engl.* multi-wall carbon nanotube)
NIR	naher Infrarotbereich
OD	Optische Dichte

MWNT	mehrwandige Kohlenstoffnanoröhre (*engl.* multi-wall carbon nanotube)
OD	Optische Dichte
NIR	naher Infrarotbereich
PFO	Poly(9,9-di-n-octylflourenyl-2,7-diyl)
PFO-Bpy	Poly(9,9-di-n-octylflourenyl-2,7-diyl)-bipyridine
SDS	Natrium-deoxycholat (*engl.* Sodium-deoxycholate-salt)
SWNT	einzelwandige Kohlenstoffnanoröhre (*engl.* single-wall carbon nanotube)
UV	Ultraviolett
VIS	sichtbarer Spektralbereich (*engl.* visible)

Im Folgenden werden englische Begriffe, sofern sie in der wissenschaftlichen Fachsprache etabliert sind, nicht ins Deutsche übersetzt.Dies gilt für nachstehende Bezeichnungen:

sonicator	Ultraschalldesintigrator
surfactant	grenzflächenaktive Substanz
nanobeads	Nanokügelchen
forward-bias	Durchlassrichtung
backwards-bias	Sperrrichtung
built-in field	intern aufgebautes Feld
Homojunction	p-n Übergang mit nur einem Halbleiter-Material
Heterojunction	p-n Übergang mit zwei Halbleiter-Materialien

1 Introduction

Semiconductor technology forms the basis of modern society. As described by Moore's law, the exponential increase of our computational capabilities has transformed both science and everyday life. What would have been considered a supercomputer just 30 years ago is now a commonplace personal device. Meanwhile, other semiconductor technologies like photovoltaics transform our energy grids, moving away from centuries of fossil fuel-powered economies. These processes are driven by ever more refined manufacturing techniques of silicon devices. However, this trend can not continue indefinitely. As the scale of our devices approaches quantum-mechanical limitations, new materials will be required to advance beyond silicon. One of the most promising of these new material classes are low-dimensional semiconductors.
The first compounds of this class of materials to be discovered were carbon-based. Graphene, an allotrope of carbon, is a sheet with the thickness of a single atom and was the first fabricated two-dimensional material in 2004 [1]. A discovery which was honoured with the Nobel Prize in physics in 2010 [2]. Another significant breakthrough was the discovery of single-walled carbon nanotubes (SWNT) in 1991, a structure that, due to its tremendous length to diameter ratio, is considered a quasi-one-dimensional material. Research has revealed the exciting and promising properties of these materials. From the extraordinary material strength of graphene and carbon nanotubes to the emission properties of quasi-two-dimensional semiconductors or even superconductivity in the graphene[3]. SWNTs also can, in principle, outperform silicon in size and efficiency as transistor material[4–6].
However, despite the promising properties of carbon allotropes, research into alternative materials to elemental carbon has not stopped. If carbon compounds show such intriguing characteristics when reduced to their low-dimensional form, why shouldn't other materials do the same? The preparation technique used to produce the first graphene sheet has been used to reduce compounds like boron-nitride or transition metal dichalcogenides to single sheets of their crystal structure. Just like SWNTs, both metallic and semiconducting properties have been observed in the various low-dimensional compounds [7]. Boron nitride has also been used to synthesize nanotubes with an analogous structure to SWNTs. While progress in these systems individually has been considerable, another venue for discoveries has presented itself in hybrid systems, which combine two or more low-dimensional materials[8, 9].
However, investigating these systems can be challenging due to the difficulties of preparing and probing individual nanoscale objects. Both single-walled carbon nanotubes (SWNT) and two-dimensional transition metal dichalcogenide (TMDC) layers require careful preparation to acquire the low defect density necessary for meaningful measurements. Furthermore, the electronic properties of low-dimensional materials change considerably upon interaction with their environment, resulting from their large surface to volume ratio. These interactions include the introduction of charge carriers, which are stabilized by Coulomb interactions with counter-ions on the surface[10]. A vastly different mechanism of doping compared to substitutional doping in

three-dimensional semiconductor crystals. How these low-dimensional materials interact with their electronic environment is still not completely understood, which severely limits their potential applications. After all, silicon is rarely used without first altering its electronic properties via doping. If low-dimensional materials are to supplement or supplant silicon-based semiconductors, the changes in their electronic properties when implemented in their respective operating environment needs to be thoroughly understood. Aiming to further our understanding of these issues, this thesis had three main objectives:

1. Preparation high-quality SWNT suspensions with a low defect density and long tube length.

2. Development of a PL microscopy setup that can probe a wide range of low-dimensional materials to investigate Hybrid-structures.

3. Investigation of the charge carrier behavior in doped SWNTs.

Chapter 2 elaborates on the theory necessary to understand the experiments and their interpretation in this dissertation. This includes the physical properties of low-dimensional materials with a particular focus on SWNTs as well as photoluminescence microscopy and Raman spectroscopy.
In chapter 3 the experimental methods to produce SWNT suspensions are introduced. The effects of the different preparation steps on the photoluminescence quantum yield, which is a good proxy for the sample quality, is quantified. These preparation techniques were also used to produce the samples for all the other experiments in this dissertation.
Chapter 4 presents the photo-luminescence microscope that was set up for this dissertation. This setup has been used to image SWNT/hBN structures as well as SWNT/MoS_2 structures. The effect of contacting MoS_2 with SWNTs on the PL spectra is discussed.
In chapter 5 various experiments that aim to investigate the behaviour of introduced charge defects in SWNT are presented. The experimental results in the chapter were often recorded by cooperation partners. A brief introduction to their respective experimental techniques is provided, where necessary. These experiments include resistance measurements on interdigitated electrodes, EPR spectra of doped SWNTs, Raman spectra of doped SWNTs, time-dependent absorbance, and TREFISH on SWNT/PCBM blend films.
Finally the results are summarized in english and german in the chapters 6 and 7.

2 Theoretical background

The following chapter aims to overview the relevant properties of all low-dimensional materials used in this dissertation, including single-walled carbon nanotubes (SWNTs) as well hexagonal boron nitride (hBN) and molybdenum disulfide (MoS_2). Furthermore, the theoretical background for the main spectroscopic tools employed shall be provided.
The first section focuses on single-walled carbon nanotubes, their electronic properties and the effects of chemical doping on the tubes. Secondly, two dimensions (2D) materials are introduced, focusing on the significance of the electronic environment on their properties. Later, the theoretical background of the two main spectroscopic tools used in this dissertation and the involved cooperation partners are elaborated on: Photoluminescence microscopy, Raman spectroscopy and EPR spectroscopy. Unless otherwise specified, vectorial terms in equations are in **bold** font, while scalars remain in standard font.

2.1 Single-walled carbon nanotubes

SWNTs are an allotrope of carbon in which all atoms are sp^2 hybridized and form a cylindrical shape. This compound has several remarkable properties: SWNTs can both be metallic as well as semiconducting while having a tensile strength similar to carbon fibers[11]. The extraordinary properties of single walled carbon nanotubes (SWNT) result from their quasi-one-dimensional (1D) structure. Its geometry and electronic properties can be derived from graphene since SWNTs essentially are rolled-up graphene sheets [12–14] As a thought experiment rolling up a graphene sheet can produce numerous different SWNT types, depending on the roll-up angle and diameter. The roll-up vector can uniquely identify all SWNT structures, which also enables the prediction of its electronic properties via tight-binding simulations. The following chapter elaborates on this classification method and explains how the resulting electronic structure and properties emerge from this approach. Unless otherwise referenced, the information in this chapter is based on a textbook by Saito et al. [15].

2.1.1 Molecular and electronic structure of SWNTs

2.1.1.1 Geometric structure and Nomenclature

The geometric structure of SWNTs can be derived by rolling up a single quasi-two-dimensional layer of graphene. Based on this idea, a nomenclature has been developed, which can identify all possible forms of SWNTs [12, 13, 15]. In order to produce the structure of SWNTs from graphene, two base vectors, $\boldsymbol{a}_1$ and $\boldsymbol{a}_2$, are defined, which move along the C-C bond axis, as illustrated in figure 2.1.

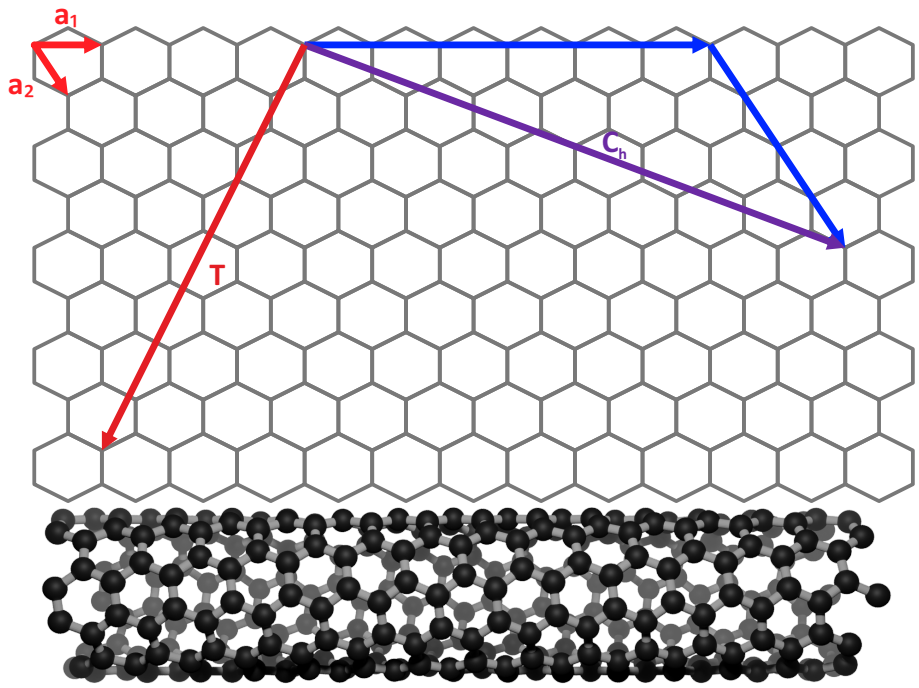

Figure 2.1: Illustration of SWNT nomenclature, derived from figuratively rolling up a graphene sheet. The base vectors $\boldsymbol{a}_1$ and $\boldsymbol{a}_2$ form the base vectors for constructing every possible SWNT. In this example, the blue vectors show how a (6,4) tube is obtained. The resulting roll-up vector $\vec{C}$ and translation vector $\vec{C}$ can be directly derived. Below is a 3D rendering of the resulting (6,4) tube.

The length of both base vectors is identical, since they both move along one sp^2 C-C bond. The lattice constant can be described as:

$$|\boldsymbol{a}_1| = |\boldsymbol{a}_2| = a_0 = \sqrt{3} \cdot 1.42\,\text{Å} = 2.46\,\text{Å} \tag{2.1}$$

The length of these vectors is derived from the distance of neighbouring C-Atoms in graphene 1.42 Å [14]. These base vectors can be used to define the roll-up vector $\boldsymbol{C}_h$ for a carbon nanotube which is described by the following formula:

$$\boldsymbol{C}_h = n_1 \cdot \boldsymbol{a}_1 + n_2 \cdot \boldsymbol{a}_2 \tag{2.2}$$

The Integers n_1 and n_2 denote how many C-atoms to move alongside the base vectors. This methodology defines every possible SWNT and provides all basic geometric information like diameter, translation vector, and the primitive cell of the nanotube. Swapping the descriptor-pair results in enantiomers of a given tube. However, since it is not possible to distinguish between enantiomers under most experimental circumstances the descriptor pair is usually used with the nomenclature (n_1, n_2) with the requirement $n_1 > n_2$. Consequently, tubes defined this way are also referred to as the chirality of an SWNT, encompassing both possible enantiomers. The diameter d_{SWNT} is derived as follows:

$$d_{SWNT} = \frac{|\boldsymbol{C}_h|}{\pi} = \frac{\sqrt{3} a_{CC} \sqrt{n^2 + nm + m^2}}{\pi} \tag{2.3}$$

where a_{CC} is the distance between neighboring C-atoms (1.42 Å in graphene). Unlike a 3D crystal structure, longer SWNTs are derived by translation solely along the translation vector, which can be expressed using the base vectors $\boldsymbol{a}_1$ and $\boldsymbol{a}_2$.

$$\boldsymbol{T} = t_1 \boldsymbol{a}_1 + t_2 \boldsymbol{a}_2 \equiv (t_1, t_2) \tag{2.4}$$

The translation vector is normal to $\boldsymbol{C}_h$ so by using $\boldsymbol{C}_h \cdot \boldsymbol{T} = 0$, the following expressions for t_1 and t_2 can be obtained:

$$t_1 = \frac{2m + n}{d_R}, t_2 = -\frac{2n + m}{d_R} \tag{2.5}$$

Translation of this unit cell along the tube axis allows the geometrical construction of an arbitrary long tube, resulting in its characteristic quasi 1D structure. A (6,5) tube for instance has a diameter of 0.81 Å [16]. Using common preparation techniques, the average tube length is generally above 0.5 µm [17], resulting in a length to diameter ratio of over 7000:1. Beyond just being an unusual geometric property, this also has a profound impact on the electronic properties of SWNTs, as will be discussed in the following chapter.

2.1.1.2 Electronic structure of SWNTs

As mentioned in section 2.1.1.1, the geometric structure of SWNTs can be derived by understanding the tube as rolled-up graphene sheets. The same principle also applies to their electronic properties. The graphene energy dispersion, as obtained by tight-binding calculations, can be used to determine the energy bands of SWNTs. By rolling up the graphene sheet, the chiral

vector $\boldsymbol{C_h}$ enforces a periodic boundary condition. Thus the wave-vector associated with $\boldsymbol{C_h}$ becomes quantized, while the translation vector $\boldsymbol{T}$ remains continuous, assuming infinitely long tubes. Consequently, the energy bands of an SWNT consist of a set of one-dimensional energy dispersion relations derived of cross-sections of the energy dispserion of graphene.
Describing electronic properties of graphene and SWNTs is simpler in reciprocal space. Therefore the reciprocal lattice vectors $\mathbf{K_1}$, along the circumferential direction and $\mathbf{K_2}$, running along the tube axis, are introduced. They can be defined by the relation $\boldsymbol{R_i} \cdot \boldsymbol{K_j} = 2\pi\delta_{ij}$, where $\boldsymbol{R_i}$ and $\boldsymbol{K}_j$ are the lattice vectors in real and reciprocal space respectively. δ_{ij} is the Kronecker delta. $\boldsymbol{K_1}$ and $\boldsymbol{K_2}$ satisfy the relations:

$$\boldsymbol{C}_h \cdot \boldsymbol{K}_1 = 2\pi, \quad \boldsymbol{T} \cdot \boldsymbol{K}_1 = 0, \quad \boldsymbol{C}_h \cdot \boldsymbol{K}_2 = 0, \quad \boldsymbol{T} \cdot \boldsymbol{K}_2 = 2\pi \tag{2.6}$$

From this follows that $\boldsymbol{K}_1$ and $\boldsymbol{K}_2$ can be written as

$$\boldsymbol{K}_1 = \frac{1}{N}(-t_2\boldsymbol{b}_1 + t_1\boldsymbol{b}_2), \quad \boldsymbol{K}_2 = \frac{1}{N}(m\boldsymbol{b}_1 - n\boldsymbol{b}_2) \tag{2.7}$$

where $\boldsymbol{b}_1$ and $\boldsymbol{b}_2$ are the reciprocal lattice vectors of a graphene layer.
Figure 2.2b) and c) shows the energy contours of the graphene π-bands in the first Brillouin zone. The optical transitions usually occur near the K points, where the conduction and valence bands are energetically closest to each other. The boundary conditions that result from the quantization of $\boldsymbol{C_h}$ can be represented as cuts through the graphene band structure in reciprocal space. Figure 2.2 a) shows how those cuts would be aligned, for the example of a (4,2) carbon nanotube.

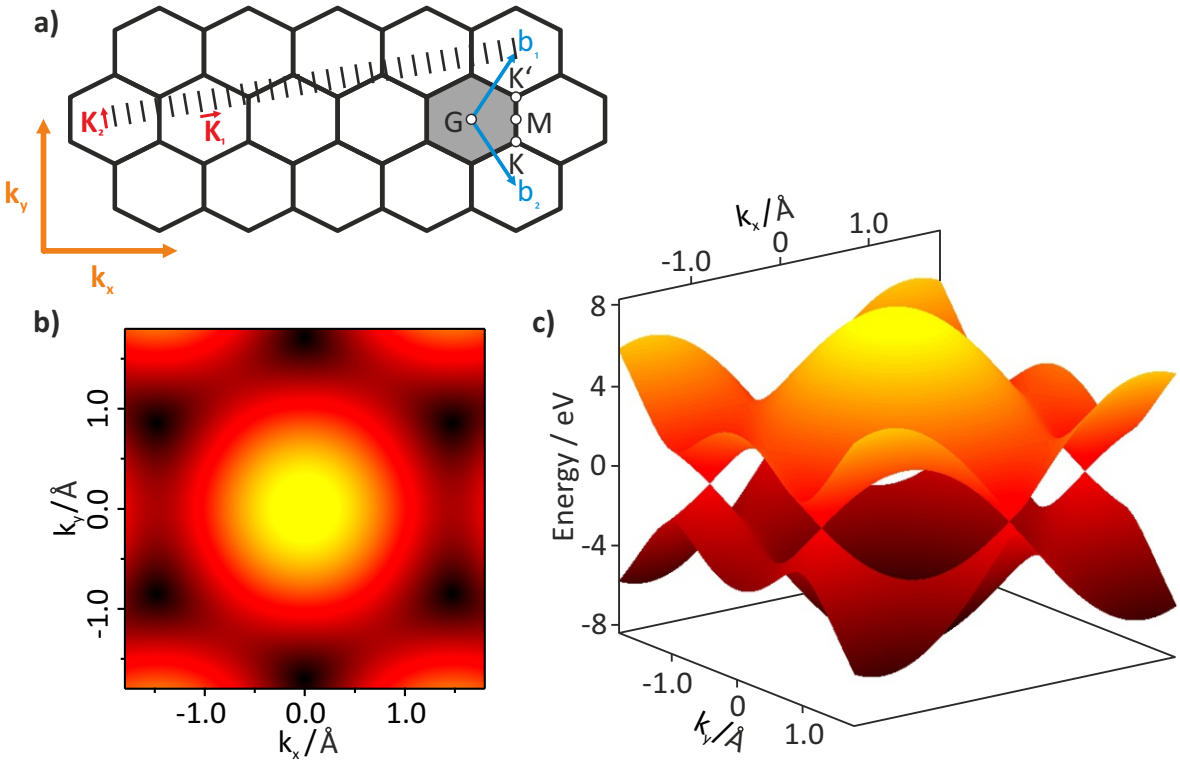

Figure 2.2: a) Equidistant parallel cuts in reciprocal space. The cutting lines in this example would result in the energy structure of a (4,2) tube. The base vectors k_x and k_y are identical in all three images. b_1 and b_2 mark the reciprocal lattice vectors. M, K and Γ mark high-symmetry points in the Brioullin-zone, indicated by the grey area. b) 2D representation of the energy dispersion of graphene, based on π-band tight-binding calculations. The colour scale indicates the energy level. c) 3D representation of the graphene band structure. Conduction and valence band are symmetrical to the Fermi energy level.

Following this methodology, SWNT can be metallic or semiconducting, depending on the roll-up vector. The energy dispersion of graphene is approximately linear near the K point and can be calculated as follows:

$$E_G = \frac{\epsilon_{2p} \pm \gamma_0 \cdot w(\vec{k})}{1 \pm s \cdot w(\vec{k})} \tag{2.8}$$

where $\epsilon_{2p} = 0$ is the $2p_z$ orbital energy and $s = 0.129$ is parameter describing the asymmetry of the bonding and anti-bonding π/π^* orbital band. γ_0 is the transfer integral of the nearest neighbor and typically has a value of $\gamma_0 = 3.033$ eV [15]. This linear relation leads to a conical energy surface, referred to as Dirac cons, which is illustrated in figure 2.3.

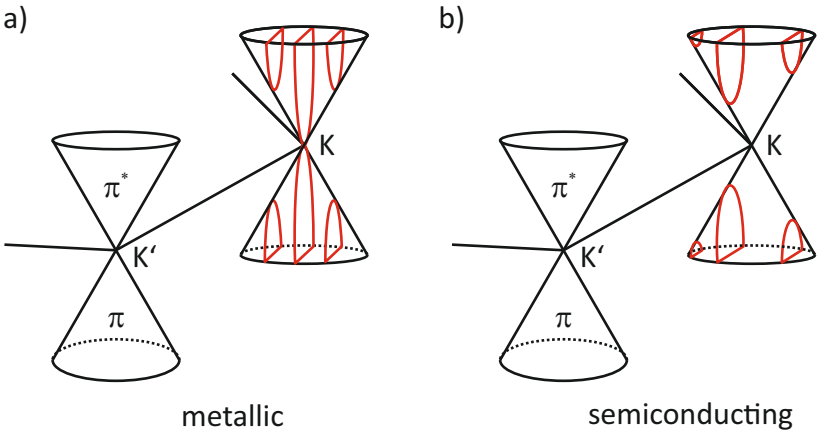

Figure 2.3: Cuts through Dirac cones which approximately represent the energy dispersion of graphene near the Fermi level can be used to determine the energy bands of SWNTs. Cutting along the circumferential vector can result in metallic tubes (a)) without bandgap since the cut produces no gap in the density of states at the Fermi level. Alternatively, cuts can produce a bandgap (b), resulting in semiconducting SWNTs. Drawn after Weisman and Kono [18]

In semiconducting CNTs like the (6,5) chirality, the cuts do not go through the K point, leading to a bandgap and thus its semiconducting properties. Conversely, a SWNT becomes metallic only when the cuts go through the K point, which occurs for tubes if $2n + m$ or $n - m$ is a multiple of 3. Beyond the intuitive understanding that Dirac cones may provide, the tight-binding method can be used to calculate the Brillouin-zone of graphene and derive the complete band structure of an SWNT [15]. Figure 2.4 shows the calculated band structure of a (6,5) single-walled carbon nanotube, based on tight-binding calculations.

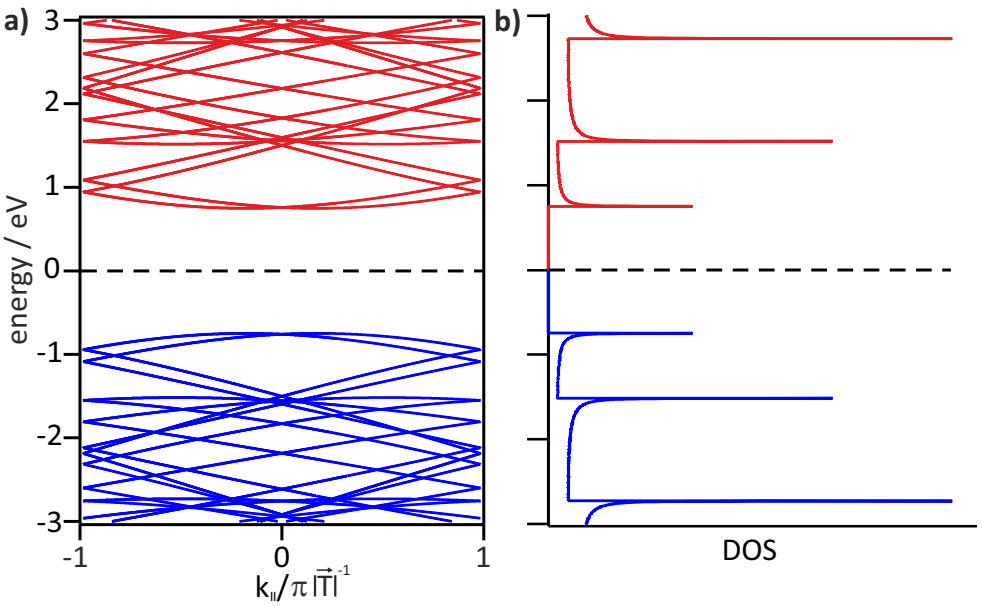

Figure 2.4: a) Band structure of a (6,5) SWNT as obtained by tight-binding calculations. γ_0 = 4.1 eV reproduces the experimentally observed bandgap of $\approx$ 1.55 eV b) The corresponding density of states to band diagram.

The density of states (DOS) is derived from the band structure. Particularly noteworthy are peaks in the DOS, so-called van-Hove singularities. They are an expected feature of a one-dimensional system [19]. Electronic transitions usually occur between states at these singularities. However, unlike most 3D crystals, electronic excitation does not result in a transition between the first two sub-bands (E_{11}). The one-dimensional character of SWNTs causes excitonic transitions to be considerably more pronounced, which significantly impacts their optical properties, as is elaborated on in the following chapter.

2.1.2 Photophysical properties of SWNTs

2.1.2.1 Excitons and trions in SWNTs

Excitons

Compared to 3D materials, interactions with the dielectric environment have a large impact on the electronic properties in low-dimensional materials. Particularly noteworthy is the impact on the excitonic transitions. The electric field mediating the exciton binding energy extends into the surrounding medium. Since the Coulomb interaction between holes and electrons are not nearly as strongly screened by air or vacuum compared to bulk crystal material, the exciton binding energy in 1D semiconductors is strongly increased [20, 21]. As an example (6,5) SWNTs show, depending on the environment an exciton binding energy of 300 meV to 400 meV [22–24], compared to the one of bulk silicon of 15 meV [25]. As a result, oscillator strength is shifted from free-electron excitations towards excitonic transitions, as schematically illustrated in figure 2.5. Due to the decreased screening, electron-electron interactions are more pronounced, increasing the conduction band's energy. The resulting increase in bandgap is referred to as bandgap renormalization.

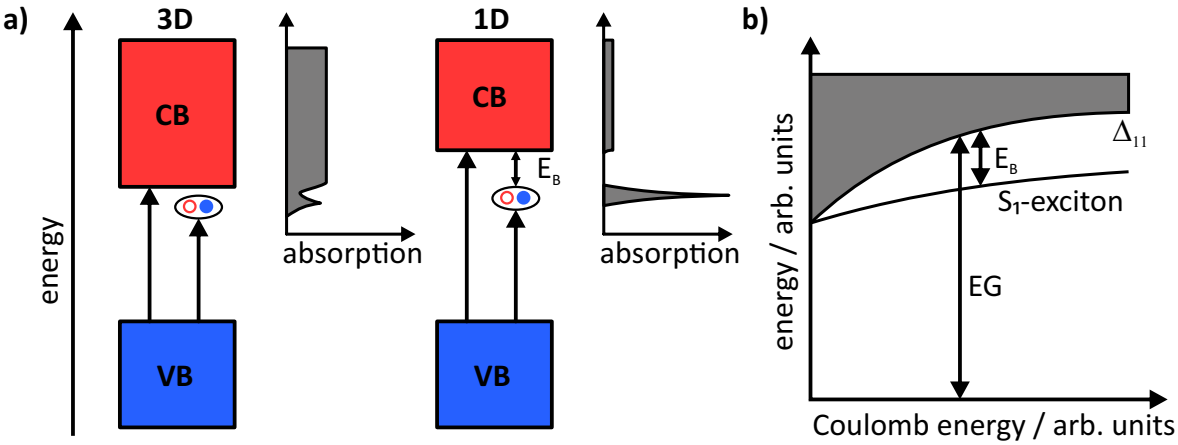

Figure 2.5: a) Qualitive illustration of the the changes in band structure moving from three dimensional to one-dimensional systems. The exciton binding E_B increases, as well as the bandgap. The insets illustrate the effects on the absorption spectra of the respective materials. b) Effects of increasing Couloumb energy on band gap and exciton binding energy.

As a consequence, excitonic transitions dominate the optical spectra of SWNTs [26]. In the instance of (6,5)-CNTs at 1.24 eV, the transition occurs in the NIR-spectrum. However, the exciton structure is SWNTs is significantly more complex than just a single strong excitonic state. Theoretical calculations by Spataru et al. [27] elucidate a more complex electronic structure. In the band structure, shown in figure 2.4, the two highest valence bands and the two lowest conduction bands are each degenerate. Therefore there are four possible excitons, of which only one represents a dipole allowed excitation, due to symmetry considerations [27, 28]. The optically inactive excitons are usually referred to as "dark" [29–33], while the active one is described as "bright" [34]. Aside from the active bright excitons, there are 15 dark excitonic states due to spin and valley degeneracy [35]. Furthermore, the bright exciton can be differentiated by its spin configuration, with one singlet and four triplet excitons. Unless otherwise specified, excitonic transitions in SWNT usually refer to the dipole allowed singlet S_1 exciton and the photoluminescence spectra of SWNTs are dominated by this transition. However, dark excitons are nonetheless important for PL considerations since they significantly reduce the quantum efficiency of SWNTs.

Trions

The increased stability found in excitons also applies to charged excitons, another quasi-particle called trions. Trions are usually denoted by $X^{\pm}$ and are a common feature of doped semiconductor materials, including SWNTs [36, 37]. They were first proposed by Lampert [38] as "excitonic ions", analogous to H_2^+. However, in 3D crystals, the binding energy of trions is minuscule, making their observation only possible at cryogenic temperatures. Even in doped Cadium-Telluride quantum wells, the binding energy only amounts to a couple of meV [39]. However, in SWNTs, the binding energy of singlet trions was predicted to be significantly stronger at 20 meV to 80 meV [40, 41], making them stable at room temperature. Consequently, an additional trionic signal can be observed in the absorption and photoluminescence spectrum of SWNTs if additional charges are added to a carbon nanotube. For (6,5) SWNTs this new feature is visible at 1.08 eV, significantly red-shifted to the excitonic band [42]. Interestingly the experimentally determined value for the trion binding energy is 175 meV [36], far exceeding theoretical predictions. Matsunaga et al. [36] explains this discrepancy via the splitting of singlet and triplet excitons, which results from strong exchange interactions and electron-hole correlation. It can amount to up to 100 meV [36].

2.1.2.2 Photoluminescence of SWNTs

Photoluminescence of semiconducting SWNTs was first reported in 2002 by O'Connell et al. [43]. After excitation into excitonic states, there are various deactivation pathways. A radiative one from the S_1 state into the ground state as well as nonradiative deactivations via heat dissipation. The most relevant activation and deactivation pathways are illustrated in the Jablonski diagram 2.6.

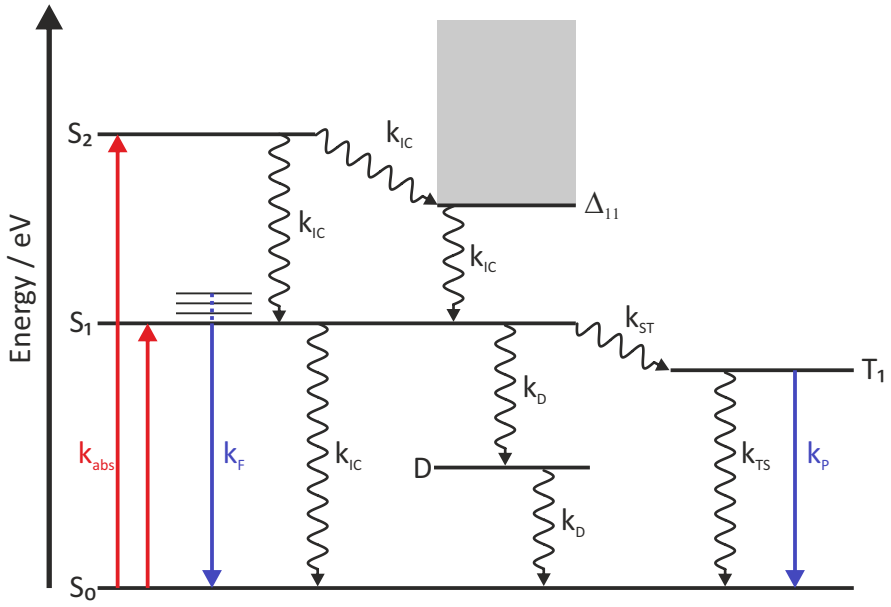

Figure 2.6: D indicate defect states. Straight lines indicate transitions involving absorption or emission of photons, while wavy lines indicate dark transitions. S marks singlet states, while T marks triplett states. Reproduced from Harris [44]

As discussed in section 2.1.2.1 the optical absorption of SWNTs are dominated by excitonic transitions, here designated as the first and second excitonic state (S_1 and S_2). The internal conversion from the S_2 state into the S_1 is extremely fast and is reported to occur within only 40 fs [45]. As a consequence ,this process is also very efficient, approaching nearly quantitative yields [45–47]. Consequently excitations into the S_2 state result almost exclusively in S_1 emission. The reported fluorescence lifetime varies considerably with the experimental conditions and ranges between 10 ps to 250 ps [48–52]. Due to non-radiative deactivation processes, the fluorescence lifetime is 3-4 orders of magnitudes lower than the bright exciton lifetime at 1 ns to 6 ns [34, 48].
Non-radiative decay can occur by the interaction of an exciton with defect sites on the carbon nanotube, which leads to the intermediate defect state D. From this state, the system relaxes into the ground state without emitting a photon. Furthermore, an intersystem crossing into the triplet state T_1 is possible. Due to the change in multiplicity, this process is considerably slower than k_F or non-radiative decay, so most of the emission occurs directly from S_1 into the ground state.
The photoluminescence quantum yield (PLQY) is the ratio of emitted photons to absorbed photons. It can also be expressed by the ratio of the rate of radiative decay k_r to the sum of all radiative and non-radiative decay rates (k_nr):

$$PLQY = \frac{N_{Pl}}{N_{Abs}} = \frac{k_r}{k_r + k_{nr}} \approx \frac{k_r}{k_{nr}} \tag{2.9}$$

The approximation applies to most SWNT samples since the PLQY is typically 1 % [53–56], mainly due to non-radiative decay via dark excitons. Furthermore, the PLQY is very sensitive to an increase in defect density since it increases the nonradiative decay rate k_D immensely. The reason for this very high sensitivity lies in the diffusion of excitons along the tube axis and how they come into contact with defects. The following chapter explains this mechanism in more detail and its impact on exciton lifetime and quantum yield.

2.1.2.3 Diffusion limitation

One challenge associated with SWNTs as a photo-emitter is their low PLQY compared to other fluorophores, ranging from 10^{-4} to 10^{-2}, although state of the art preparation techniques usually yield a PLQY at the higher end of that spectrum [54, 57–64]. As mentioned in section 2.1.2.2 defect states are one significant non-radiative decay pathway. The reason for this is found in the quasi-free movement of excitons in SWNTs across the tube axis. Since the exciton wave function encompasses the entire tube diameter, the exciton can only move one dimensionally. As mentioned in section 2.1.2.2 the PLQY is determined by the likelihood of exciton recombination relative to non-radiative decay. The probability for the defect deactivation pathway is primarily determined by the probability that an exciton interacts with a defect site localized on tube [65–67]. These defect sites can be sp^3-defects, covalent functionalization, or the tube ends themselves. As illustrated in image 2.7 both the defect density as well as the average tube length are a factor in the PLQY of SWNTs.

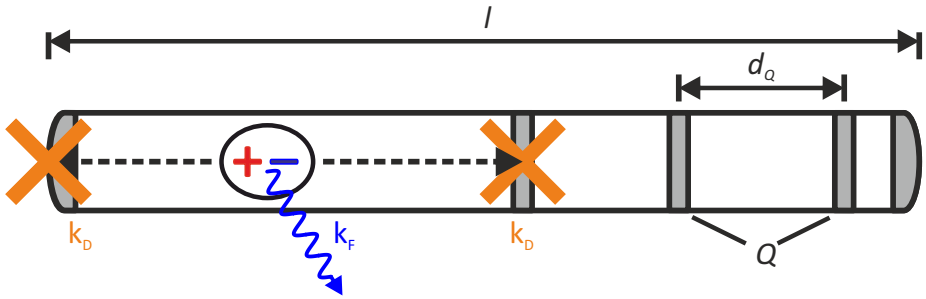

Figure 2.7: Illustration of Photoluminescence Quenching in SWNTs. Excitons diffuse across the length of the SWNT. The grey areas indicate a defect site (*Q*). If they hit a defect site or a tube end, a non-radiative decay occurs. The tube ends also represent a defect in SWNT structure, making the tube length ([l]) important when considering defect density. The average distance between two defects is designated as d_Q

Consequently, the photoluminescence quantum yield (PLQY) of SWNTs is fundamentally diffusion-limited [54, 68]. The exciton diffusion length across the SWNT-axis is defined as:

$$L_D = \sqrt{D \cdot \tau_{PL}} \tag{2.10}$$

where D is the diffusion constant of the exciton and τ_{PL} the PL lifetime. Reported values for L_D range between 100 nm to 600 nm, depending on the experimental conditions. Values for the diffusion coefficient D range between 0.1 $cm^2\ s^{-1}$ to 11 $cm^2\ s^{-1}$ [30, 54, 69–72]. Using this kinetic model for the exciton diffusion in (6,5) tubes results in the following scaling of the PLQY (Φ_{PL}), with the defect density (*Q*) and the diffusion coefficient D[54]:

$$\Phi_{PL} \propto [Q]^{-2} D^{-1} \tag{2.11}$$

As a result, SWNTs-PLQY is highly sensitive towards defects. Consequently, PL experiments benefit from long, defect-free tubes to minimize the likelihood of non-radiative decay and thus an increase in PLQY and thus signal intensity. The PLQY can also be used to gauge the defect concentration, including intentionally introduced defects like doping, as will be discussed in the following section.

2.1.3 Doping of SWNTs

In contrast to bulk semiconductors, SWNT doping, in this instance, is not achieved by substituting atoms in the crystal lattice with other elements. Instead, redox chemicals are used to introduce additional charges unto the SWNT, with a counter-charge carrying ion near the surface of the nanotube [10]. The effects on the spectral behaviour of SWNTs is identical when using redox chemistry as well as electrochemical gate-doping [22, 73]. The spectrum of an SWNT changes considerably with increasing doping levels, making it possible to determine the doping level of a given SWNT sample via absorption spectroscopy. The following chapter focuses on p-doping since the changes in spectral behaviour is almost identical to that of n-doping in (6,5)-SWNTs, due to the high degree of electron-hole symmetry in near-armchair carbon nanotubes [41, 74, 75].

When it comes to changes in spectral behaviour, absorption spectroscopy has proven one of the most effective tools for investigating doping. Doping introduces defects into the SWNT, which quenches most of the PL signal, even at low doping levels [69], limiting its usefulness for investigating doping. The absorption spectra changes considerably with increasing doping level, but the overall oscillator strength remains sufficiently high to gather valuable insights into the doping process. The changes in absorption behaviour of (6,5)-SWNTs are illustrated in figure 2.8.

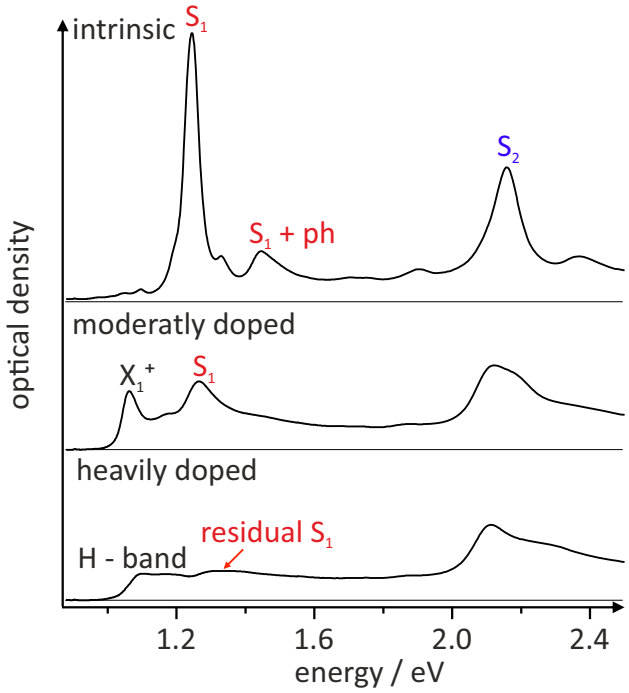

Figure 2.8: Spectra of doped (6,5)-SWNTs. The intrinsic spectrum shows all typical signal components: the first excitonic S_1 band, the phonon sideband S_1+ ph and the second excitonic transition S_2. In the moderately doped regime, the excitonic transition is bleached while the trionic signal X_1^+ forms. Furthermore, line broadening, probably from a new signal component, occurs at the S_2 transition. In the heavily doped regime, the trionic signal is quenched as well, leaving behind the featureless H-band. Reproduced from Eckstein et al. [76]

In its intrinsic state, the typical observation features mentioned previously are present. The S_1 signal corresponding to the first excitonic transitions at 1.24 eV [24, 77–79] and its phonon sideband at 1.45 eV [80–82]. As the doping level increases and we move into the moderate doping regime, the excitonic transition loses oscillator strength, while a new signal the X_1^+ band emerges. This signal has been identified as charged excitonic state (or trion) [22, 36, 37, 42, 64, 83–88]. Furthermore the transition energies of exciton bands are blue-shifted with increasing doping-level of up to 80 meV [22, 86, 89, 90]. This blue shift has been attributed to a bandgap renormalisation, following the depletion of binding orbitals after p-doping [86, 89, 90]. Doing so assumes that the changes introduced by doping are homogeneously distributed across the SWNT, like in 3D bulk semiconductors like silicon. There are alternative explanations to this rather simple model, which the following sections will elaborate on.
Further doping the SWNT leads to a decline of the X_1^+ band as well. What remains is a featureless band like spectrum called the H-band. Increases the doping beyond this point can bleach even this remaining spectrum, leaving no distinguishable features [76]. The physical reason for these spectral changes is a more contested subject matter. There are two functional models that correlate the absorption behaviour to localised and homogeneous charge distributions.

2.1.3.1 Phase space filling model

The exciton bleach observed in transient absorption spectroscopy has routinely been explained using a phase space-filling (PSF) model [91–93]. Using a modified version of the same model, the exciton bleach of doping can be correlated to the charge density on the nanotube. Under the assumption of homogeneous doping, absorption behaviour strongly correlates to the exciton size. If the exciton is formed using a small distribution of momentum states, then, following the Heisenberg uncertainty principle, the exciton itself is more narrowly localized. Doping first depopulates the conduction or valence band states nearest to the Fermi level (see figure 2.9). Consequently, there is a smaller window from which oscillator strength can contribute to exciton formation [94]. This is also why the first few doping steps have the largest impact on the absorption spectra.

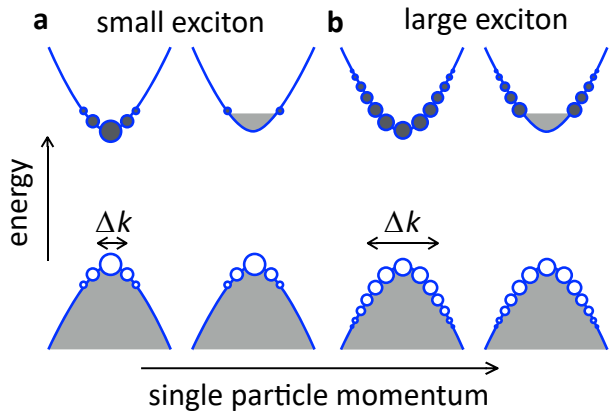

Figure 2.9: Illustration of the effect of different exciton sizes on the participation of k-states to the exciton wave function for doped and intrinisc nanotubes. Drawn after Eckstein et al. [94].

This model was initially devised to interpret the nonlinear optical spectroscopy of SWNTs and assumes that an electron and a hole state are simultaneously removed from the coherent superposition of wavefunctions [91, 95, 96]. It was shown that the exciton bleach χ is given by [70, 96]:

$$\chi = \frac{f_0 - f}{f_0} = \frac{\sum_k [f_e(k) + f_h(k)]\Psi(k)}{\sum_k \Psi(k)} = \frac{N}{N_s'} \tag{2.12}$$

where f is the oscillator strength, f_0 the oscillator strength in the intrinsic state, $f_{e,h}(k)$ the electron and hole distribution functions and $\Psi(k)$ the envelope of the 1D exciton motion orbital wave function in the reciprocal space. N is the exciton density and $N_s = (2.05\zeta)^{-1}$ the saturation exciton density, with the exciton size ζ. In order to interpret the effects of p-doping, only the reduction of valence band states is modelled. Furthermore, screening effects are neglected, under the assumption that mainly the reduction of available states drives exciton bleach. From this follows:

$$\chi = \frac{\int_{-\infty}^{+\infty} f_h(k)\Psi(k)\mathrm{d}k}{\int_{-\infty}^{+\infty} \Psi(k)\mathrm{d}k} = 2c^{-1}\int_0^{\infty} f_h(k)\Psi(k)\mathrm{d}k \tag{2.13}$$

where the integrals replace the sums, $f_h(k)$ is the Fermi-Dirac distribution function for holes in the valence band (VB) and $c = 2\zeta^{-\frac{1}{2}}\pi^{\frac{3}{4}}$ is the solution of the denominator integral. With a known exciton size and this model makes it possible to determine the charge density at a given exciton bleach value.

2.1.3.2 Confinement Model

Recently this homogeneous picture of SWNT-doping has been into question. There is experimental evidence that suggests that charges are instead localized, and the changes in spectral behaviour can also be accurately modelled with a localized charge distribution [76]. Using a redox reagent will typically involve transferring an electron from the SWNT to the reagent. However, the observed level of doping correlates primarily with the concentration of counter-ions rather than with other reaction products [10]. Furthermore, analysis of temperature dependence of PL spectra shows that excitons show a $T^{(-1/2)}$ dependence, which reflects characteristic behaviour for one-dimensional excitons. However, trions show no temperature dependence, suggesting localization [97, 98]. In the localized model of doping, a counter-ion remains in the Helmholtz-layer of the SWNT, which via Coulomb-interactions stabilizes a trapped charge on the SWNT. A schematic illustration of this is shown in figure 2.10.

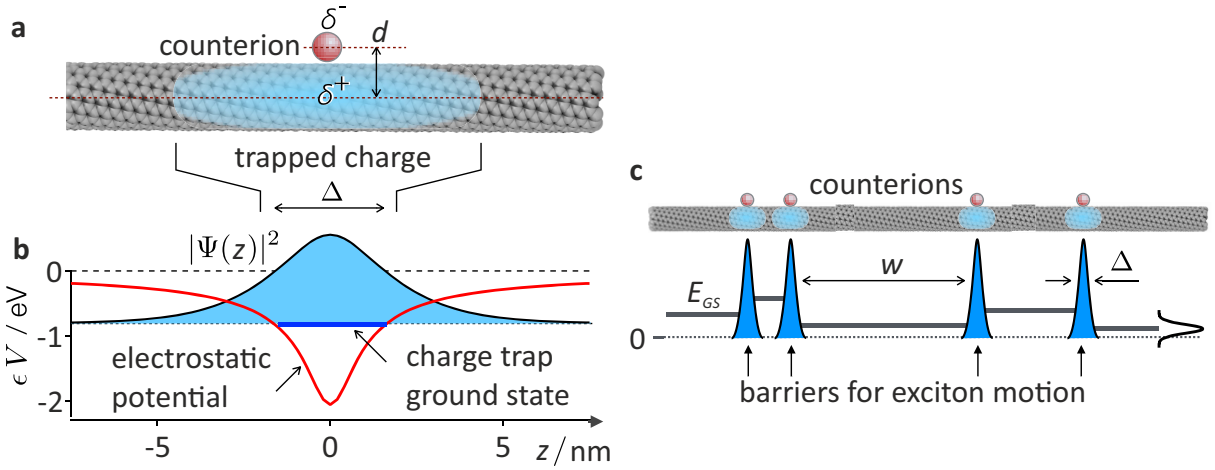

Figure 2.10: a) The interaction with the external counter-ion traps charge carriers on the SWNT. b) Electrostatic potential induced by the counterion and the corresponding electronic ground state. c) Effect of spacing between charge-traps shifts the ground state energy E_{GS} Reproduced from Eckstein et al. [76]

This field-induced charge-localization can be estimated using the local electrostatic potential surrounding the counter-ion: $V(z) = -e^2/4 * \pi\eta_0\eta(d^2 + z^2)^{1/2}$, assuming a homogeneous dielectric constant η at a counter-ion distance d from the nanotube axis and an axis displacement of z. The charge distribution in this potential well can be described by the one-dimensional Schrödinger equation with the Hamiltonian $H = -\hbar^2\nabla^2/2m_{eff} + V(z)$ The ground-state energy of excitons is increased since the counter-ions act as barriers, resulting in a particle in a one-dimensional box situation. The ground state energy of a particle in a box is given by:

$$E_{GS}(w) = \pi^2\hbar^2(2Mw^2)^{-1} \tag{2.14}$$

where w is the spacing between a pair of barriers and M is the effective mass of an exciton. The distribution of spacings is expected to follow a Poisson distribution with the probabilities $p_{\bar{w}}(w) = \bar{w}^{-1}e^{-w/\bar{w}}$ with $\bar{w}$ being the mean barrier spacing. If the line shape is assumed to follow a Voigt profile, a shape function $f_w(E)$ can be fitted to the intrinsic excitonic SWNT band. For doped samples, the following line profile can be calculated:

$$T(E) = \frac{1}{\bar{w}}\int_0^\infty p_{\bar{w}}(w')w' f_{w'}(E)\mathrm{d}w' \tag{2.15}$$

where w' and $\bar{w}^{-1}$ weigh the spectral contribution of a given SWNT segment, depending on its length and normalize the function so that total oscillator strength is conserved. The change in oscillator strength is modelled by phase space filling. To that end a width Δ is assigned to every barrier. Doing so, the distribution function $p_{\bar{w}}(w)$ changes to $\tilde{p}_{\bar{w},\Delta}(w) = \bar{w}^{-1}e^{-(w+\Delta)/\bar{w}}$. With this model the line shape and peak shift are solely controlled by the mean barring spacing $\bar{w}$. This provides another pathway to link charge concentration on a tube with the changes in the absorption spectra.

2.1.3.3 Charge quantization via optical spectroscopy

Both the band-filling and the confinement model can correlate changes in the absorption spectrum to a concentration of charges on an SWNT. By comparing the predicted changes with experimentally obtained absorption signals, a charge concentration for an SWNT can be determined. Figure 2.11 sums up the results for both models.

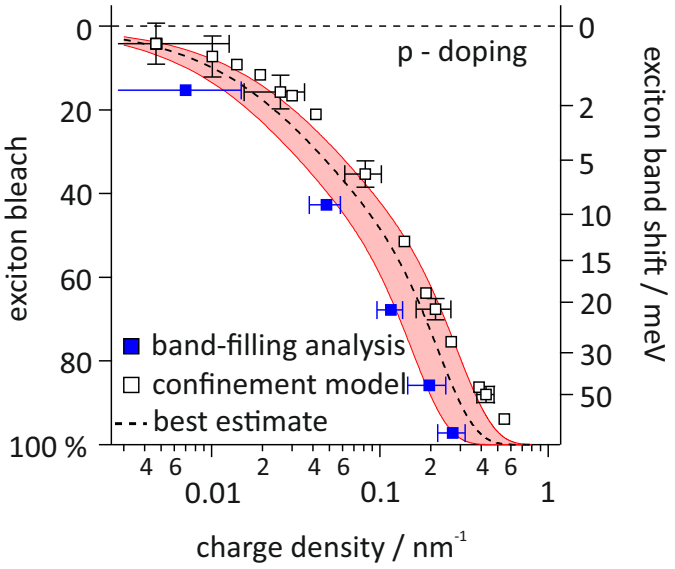

Figure 2.11: Bleach of the excitonic signal and excitonic E_{11} band-shift with increasing doping level. The observed drop in excitonic oscillator strength and exciton band shift are plotted are against charge densities as obtained by analysis via a band-filling model (blue solid squares, field-doped) and confinement model (black open squares, redox-doped). Reproduced from Eckstein et al. [94]

For the band-filling model the temperature was assumed to be 293 K and an effective hole mass of $m_{eff} = 0.07m_e$ with m_e being the electron mass [22]. The size of the exciton was assumed to b 13 nm, based on experimentally obtained values [22, 96]. The confinement model assumes a relative permittivity $\eta = 7.43$

Both models produce similar charge concentrations for the identical absorption spectra. Consequently, absorption spectroscopy alone does not prove one or the other charge distribution models. However, it makes it possible to link charge concentrations to the other spectroscopic methods and compare results of those of absorption measurements [94].

2.2 Two-dimensional materials

Transition metal dichalcogenides materials (TMDCs) are a class of quasi two-dimension semiconductors, which have attracted considerable scientific attention at the time of writing. The main reason for this increased interest is that advanced mechanical exfoliation techniques allow the production of high-quality flakes of TMCD mono-layers. Many of their exciting properties like their direct bandgap [99–101], strong fluorescence [99] or high on-off rations in field-effect transistors [102]. That includes significantly increased exciton stability and a strong dependence of electronic properties on the dielectric environment. Two of these systems, Molybdenum disulfide (MoS_2) and h-BN, have been investigated in this work and shall be introduced and elaborated in the following chapter.

2.2.1 Molybden disulfide structure and electronic properties

Mo_2 is one of the most thoroughly researched two-dimensional TMDC since it was the first one to be exfoliated [103]. Like many other low-dimensional materials, many of its exciting properties only arise when reducing the bulk material to a single layer. MoS_2 has a an hp6 crystal structure [104] with molybden and sulfide forming a hexagonal pattern on a single layer of this material, as illustrated in image 2.12.

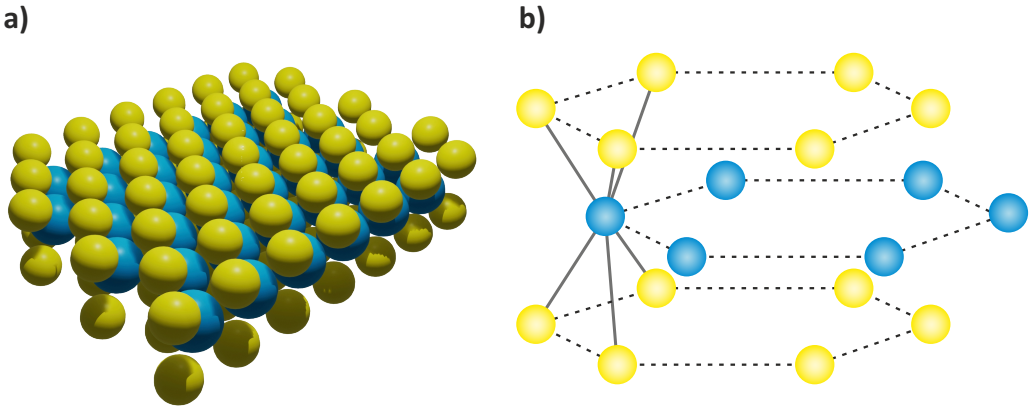

Figure 2.12: Illustration of a single layer of MoS_2 a) shows a macroscopic view of a single nanosheet of MoS_2. b) shows the crystal structure is derived from the hexagonal layers of the elements.

Like in graphene, the individual layers are only held together by van-der-Waals interactions, while the intra-layer Mo-S bond has a strongly covalent character [105]. MoS_2 changes its optoelectronic properties when thinning a stack of $MoS2_2$ down to a single layer. It transitions from an indirect bandgap semiconductor to a direct one when reducing the sample thickness to

a single layer [106, 107]. Furthermore the indirect bandgap of bulk material is about 1 eV [108, 109], while calculation put the of mono-layer MoS_2 at 1.9 eV [107]. Moving from a multi-layer to a single-payer system also changes the nature of excitonic signals. There is two direct bandgap transition at the same wave vector, the A and B exciton, as a result of the spin-orbit coupling of the valence band [110]. This has a profound impact on the photoluminescence spectrum of MoS_2. In bulk, no appreciable PL can be detected. On the other hand, the monolayer emission spectra are dominated by A, and B excitonic resonances, which is characteristic for layered molybdenum and tungsten dichalcogenides [111, 112]. As a result of an increase in transition moment, the PLQY increases by a factor of approximately 20, which, given at sufficiently low defect densities, can approach one [91]. This makes monolayers relatively easy to identify via photoluminescence microscopy since they stand out as exceptionally bright objects compared to multi-layers.

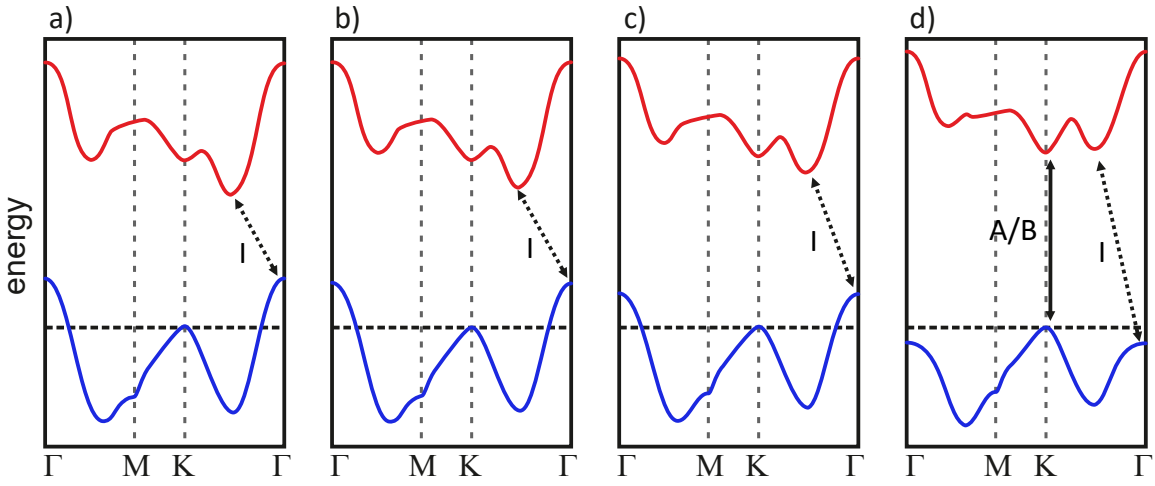

Figure 2.13: HOMO and LUMO band structure for a different number of MoS_2 layers. a) bulk MoS_2, b) quadrilateral MoS_2, c) bilayer MoS_2 and d) mono-layer MoS_2. Bulk material has an indirect bandgap which becomes larger with increasing layer thickness. For the case of mono-layer MoS_2 the material becomes a direct bandgap semiconductor. The dotted lines indicate the indirect bandgap transition, designated I, while the full line indicates the direct bandgap transition, corresponding to the A and B exciton. Reproduced from Splendiani et al. [113]

The changes in the band structure and electronic transition properties with decreasing layer thickness are illustrated in figure 2.13. The difference in relative energy shift at different wave vectors results from the spatial localization of the associated orbitals. States near the K point consist primarily of d-orbitals at the Mo atoms. Since the Mo atoms are situated in the middle of the MoS_2 unit cell, they have only negligible interactions with the environment outside their layer. States near the Γ point, on the other hand, consist predominantly of linear combinations of d orbitals of Mo and anti-bonding p_z orbitals on S atoms. The p_z component localizes them on the surface of the MoS_2 sheet and thus expose them to interactions with the environment [113].

Fluorescence tuning by doping

As with SWNTs, chemical doping has proven to be an effective tool to modify the carrier density of monolayer materials such as Mo_2 [114, 115]. The change in the absorption spectra is similar to the ones observed in SWNTs, as the first excitonic transition is red-shifted with increasing doping level. Furthermore, oscillator strength is transferred from excitonic transitions to trion transitions [116].

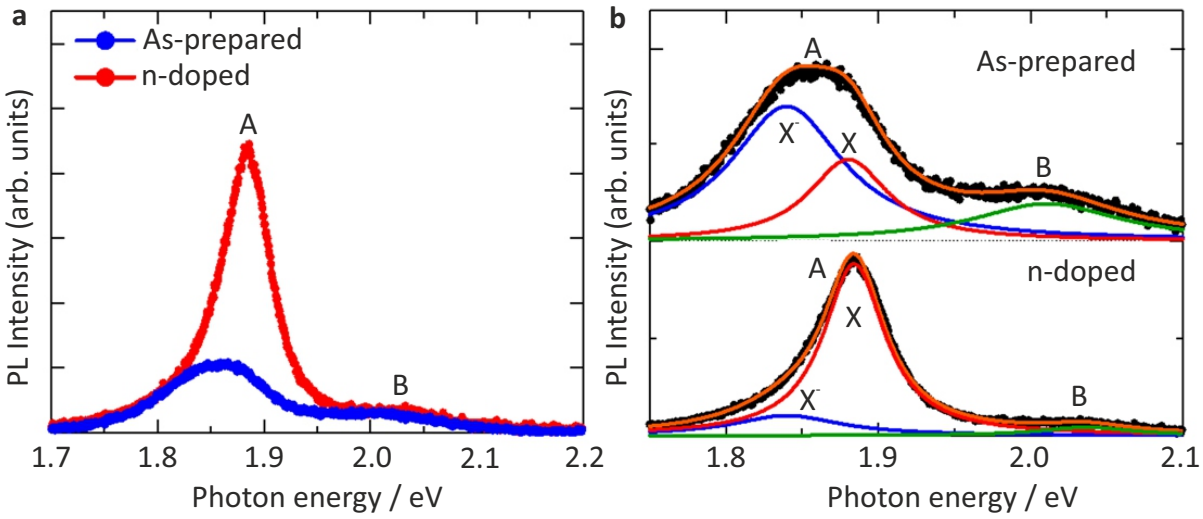

Figure 2.14: a) Overall an increase in PL intensity can be observed. A new sharped signal arises as a result of doping the material. b) Multi-peak fitting a Reproduced from Mouri et al. [64]

An overview of expected changes in the fluorescence spectra of Mo_2 is shown in figure 2.14. In the as-prepared sample of MoS_2, the fluorescence spectrum is dominated by two spectral features, the A and B excitons. The spectral line of the A exciton is a superposition of the trion X^- and the exciton X. The trion signal indicates n-type doping in as-prepared samples, which results from unintentional heavy electron doping [64, 116]. P-type doping with an oxidation agent can remove this intrinsic doping, shifting oscillator strength back from the X^- trion to the exciton.

2.2.2 Hexagonal boron nitride

Another low-dimensional material that has attracted a significant amount of academic interest is monolayer h-BN. Its structure is analogous to graphene, giving individual layers a thickness of one atom. An illustration of its structure and the lewis formula are depicted in figure 2.15. In bulk crystals, the layers are only kept together by van-der-Waals forces, making exfoliation a viable technique for the preparation of single nanosheets, just like it is in graphene [117]. However, compared to TMDCs or graphene, it has a significantly larger bandgap. In the bulk

material, the reported bandgap has been experimentally determined to be 5.95 eV [118–122]. In monolayer h-BN theoretical predictions put this value at 6 eV [123, 124]. Aside from its electronic properties, h-BN compounds, in general, are also known for their remarkable thermic, and chemical stability [125].
While the material is commonly referred to as a direct-gap semiconductor in literature [117], its large bandgap probably makes the term insulator more appropriate. Nevertheless, there have been successful experiments that make use of this extensive bandgap like UV lasing [126].

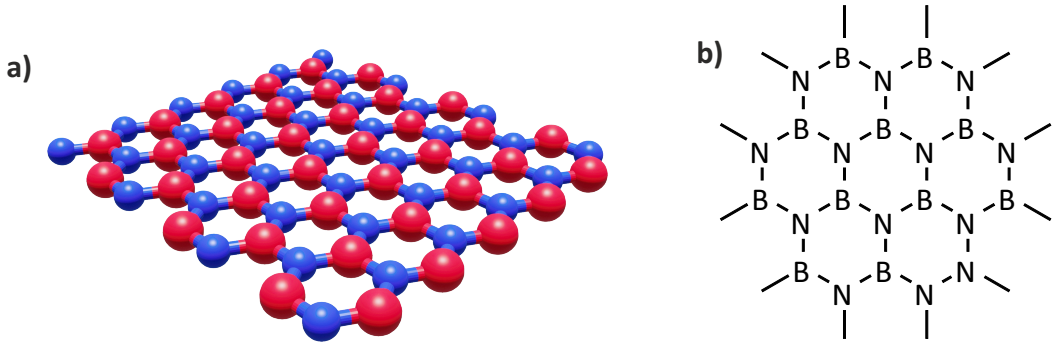

Figure 2.15: a) Three dimensional image of an h-BN sheet. Red ball indicate boron atoms, while blue balls indicate nitrogen atoms. b) Lewis formulae of h-BN. The structure forms a hexagonal lattice, analogous to graphene.

Monolayer h-BN has also found another niche as a substrate for other low-dimensional materials. It has proved to be effective in shielding other low-dimensional materials from detrimental environmental effects. Due to its atomically layered structure, h-BN provides a smooth and homogeneous surface with no defects like dangling bonds. Encapsulation of two-dimensional materials like MoS_2 can improve some properties in the encapsulated material. This includes reduced emission linewidth in transition metal dichalcogenides [127, 128], or enhanced carrier mobilities in graphene [129, 130].

2.3 Photoluminescence microscopy

Direct imaging of any object smaller than 150 µm is impossible by simply using the naked eye. However, low-dimensional materials are often far below that threshold, sometimes only a few micrometres in size. This necessitates using various magnification techniques, the most common one being microscopy. Traditional transmission microscopes rely on objects blocking a part of the light beam between source and detector to produce an image. However, it is also possible to directly image the emissions of objects themselves, a technique referred to as Photoluminescence microscopy (PLM). PLM remains an essential tool for identifying and characterizing low dimensional materials like SWNTs since the PL spectrum can contain valuable information about the interaction of the material with the environment. The following chapters aim to provide the theoretical background in the foundations of microscopy and PLM in particular.

2.3.1 Beam profile and gaussian beam

Geometric optic does not accurately describe the behaviour of electromagnetic radiation through lenses since It would necessitate an infinite energy density at the focal point. Furthermore, the wavefronts of light are never perfectly parallel. A more accurate description is provided by the model of a Gaussian beam, as depicted in image 2.16 [131].

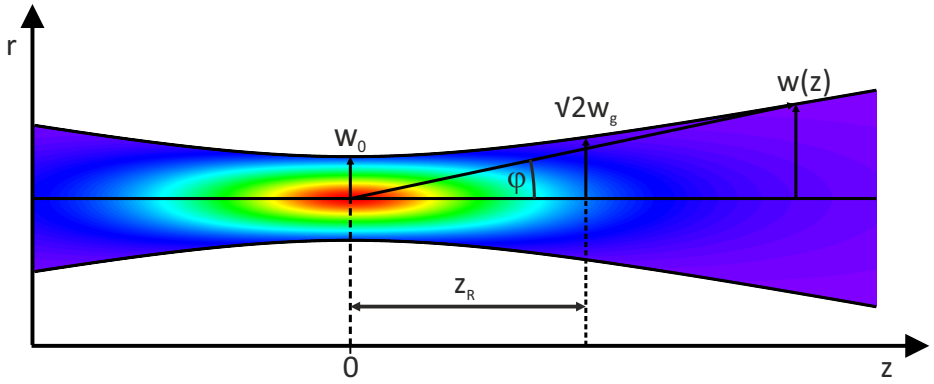

Figure 2.16: Profile of an ideal gaussian beam at its smallest diameter. The angle of divergence ρ depends on the radius of the beam waist w_0 and the wave length λ. The transversal beam profile describes the point at a distance z at which the amplitude has dropped to 1/e of the maximum. The color corresponds to the energy intensity at the given point in gaussian beam.

As the name suggests in a Gaussian beam the transversal beam profile is described by a Gaussian function:

$$w(z) = w_0\sqrt{1 + \left(\frac{z}{z_R}\right)^2} \tag{2.16}$$

In the case of a Gaussian beam, only the minimal beam waist w_0 is sufficient to characterize the beam fully. Of particular importance for microscopy is the Rayleigh length z_R:

$$z_R = \frac{\pi w_0^2 n}{\lambda} \tag{2.17}$$

where λ is the wavelength, n the refractive index of the medium and w_0^2 the beam waist size. The Rayleigh length is the distance from the focus point, where the beam width has increased to $\sqrt{2}w_0$. The Rayleigh length can be used to characterize the divergence of a laser beam. For microscopy purposes, objects are generally considered in focus when they are within the Rayleigh length of the objective. At distances where $z >> z_R$, the beam profile can be approximated as linear. Doing so allows for a simple description of the divergence angle ρ:

$$\rho = arctan(\frac{w(z)}{z}) \approx arctan(\frac{\lambda}{\pi w_0}) \tag{2.18}$$

This shows that a wider angle of divergence ρ allows for a smaller minimum beam radius w_0. This relation shows that using lenses with shorter focal distances allows capturing a wider angle

of radiation and a ”stronger” focus. Consequently, objects with low PLQY are best imaged with objectives with high NA, which can capture a more significant portion of the emitted light.

2.3.2 Resolution limit

The minimum observable size of objects in microscopy can not be infinitely decreased by optical means. Barring other experimental issues, the diffraction limit (or Abbe-limit) is usually the limiting factor:

$$d = \frac{\lambda}{2nsin\theta} = \frac{\lambda}{2NA} \tag{2.19}$$

Light with the wavelength λ can only be resolved up to a distance of d. The angle of convergence θ and the refractive index n can also be expressed through the numerical aperture of the objective NA, which allows for a simple estimate for the resolution limit [131].
The diffraction limit describes at which distance two objects can no longer be separately observed since their signals overlap to such a degree that there is no discernible minimum between them. As a result, it is not possible to determine whether two-point emitters or one elongated object produce the PL image.

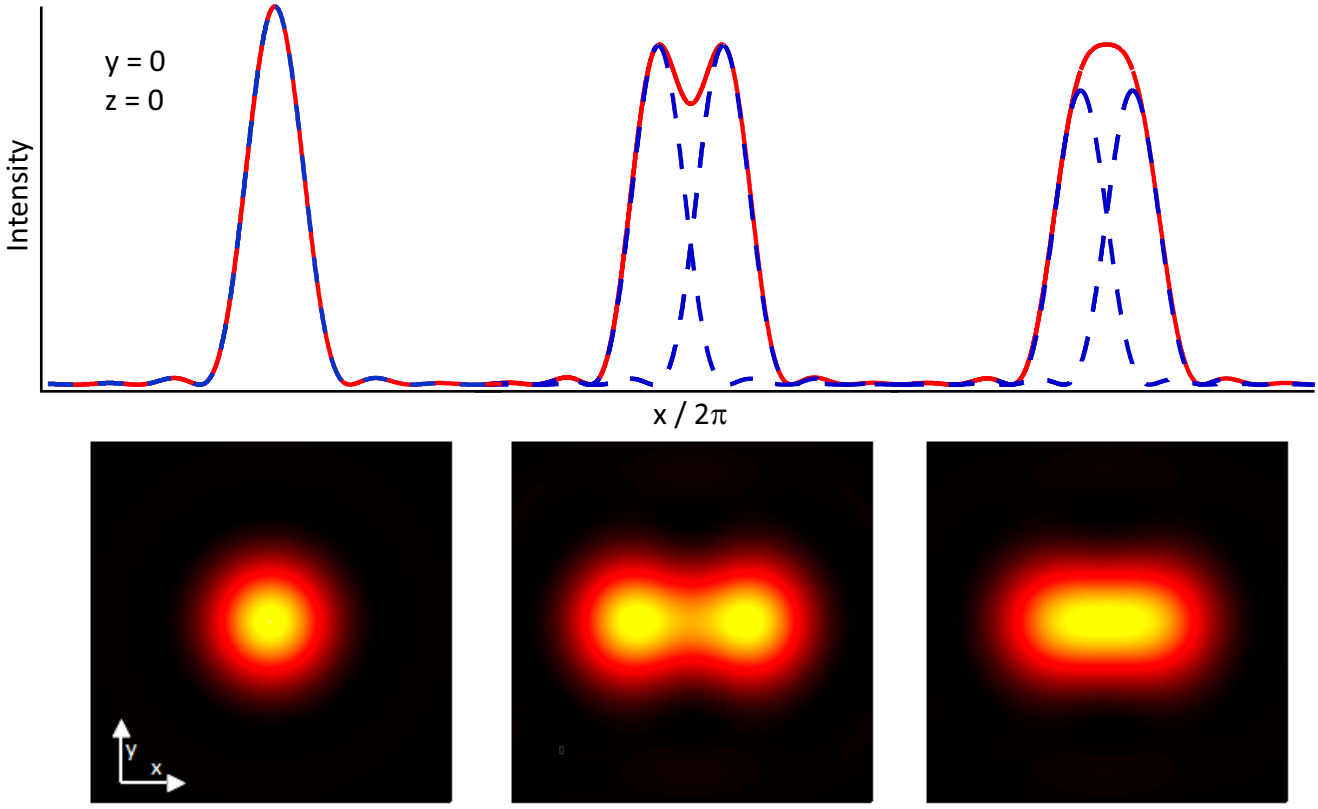

Figure 2.17: Simulated Airy-Disc patterns of point emitters. a) Image and profile of a single point emitter. b) Two-point emitters close enough to have overlapping signals, but they are far enough apart to identify minimum. Consequently, both objects can still be considered optically resolved. c) Two-point emitters which are so close together that they can no longer be distinguished as different objects. Since there is no minimum in the intensity profile, it is not possible to determine whether one elongated object or two-point emitters are observed.

A single point emitter can be described using the airy disc function, which describes a perfectly focused spot of light, assuming no other imaging errors and a circular aperture. In this case, the resolution limit is only limited by the diffraction of light.

$$PSF(r') = \left[2\frac{J_1(r')}{r'}\right]^2 \tag{2.20}$$

where J_1 is a first-order Bessel function and the normalized radius r' given by the following expression:

$$r' = \frac{\pi D}{\lambda f} = \frac{\pi r}{\lambda N} \tag{2.21}$$

where D is the aperture diameter, f is the focal length, N is the numerical aperture, and λ is the emission wavelength [132]. It should be noted that in an actual microscopy setup, the diffraction limit may not be the limiting factor. Other technical limitations like the pixel density in

the detector can constrain the resolution limit. The perfectly circular pattern, as shown in the image 2.17, also depends on the shape of the aperture if the focal plane is constrained or cut off at other points in the optical setup the exact shape from the idealized results represented here. The Abbe-Limit also provides the three potential ways to increase the spatial resolution of a given optical setup: Decrease the wavelength, increase the refractive index or increase the angular aperture. In fluorescence microscopy, the emission wavelength is usually not tunable, leaving the numerical aperture as the only viable path to increase resolution. This is usually accomplished by low working distances, and therefore high angular apertures, and immersion oils, which have a higher refractive index than air ($n_{oil} \approx 1.52$) [133].

2.3.3 Environmental effects on low-dimensional fluorophores

When investigating samples with low-intensity photo-luminescence, it is imperative to capture as much of the emitted radiation as possible. Besides increasing the numerical aperture, an often neglected factor is the substrate material upon which the observed emitter is placed. An emitter placed on a dielectric interface between materials with different refractive indices will preferably emit into the material with a higher dielectric constant (and thus refractive index). This results from a stronger coupling of the electromagnetic field to this material [131].

Therefore it is beneficial to design samples so that PL is measured through the medium with a higher dielectric constant. The downside to this approach is that it limits the experiment to mediums that are transparent to the excitation and emission spectrum.

2.4 Raman spectroscopy of SWNTs

2.4.1 The Raman effect

Unless otherwise specified, the following introduction into the theory of Raman spectroscopy is based on the work of Ferraro et al. [134].
The Raman effect describes the change in energy and momentum of inelastic photon scattering on a molecule and the coinciding change in the vibronic state of the system. In order to observe a change in the vibronic state, the induced vibration needs to produce a change in polarizability. This makes the method complementary to FT-IR spectroscopy, a resonant absorption approach, which requires a change in the dipole moment.
To understand Raman spectroscopy basics, a classical view of the interaction with a diatomic

molecule can be helpful. In this instance, the incoming photons are seen as oscillating electromagnetic fields (E).

$$E = E_0\, cos(2\pi\nu_0 t) \tag{2.22}$$

where E_0 is the vibrational amplitude and ν_0 the frequency of the incident photons. An electric dipole moment is induced when the incident photon interacts with a diatomic molecule.

$$\mu = \alpha E = \alpha \cdot E_0\, cos(2\pi\nu_0 t) \tag{2.23}$$

The polarizability α is a constant since it is a property of the molecule. If the molecule vibrates with a frequency ν_m, the molecular displacement q is given by:

$$q = q_0\, cos(2\pi\nu_m t) \tag{2.24}$$

For small amplitudes, α can be approximated as a linear function of q, which which leads to following expression:

$$\alpha = \alpha_0 + \left(\frac{\delta\alpha}{\delta q}\right)_0 q_0 + ... \tag{2.25}$$

α_0 is the polarizability at the equilibrium position while $\left(\frac{\delta\alpha}{\delta q}\right)_0$ is the rate of change in q. Equations 2.23, 2.24 and 2.25 combine into

$$\mu = \alpha \cdot E_0\, cos(2\pi\nu_0 t) \tag{2.26}$$

$$= \alpha_0 \cdot E_0\, cos(2\pi\nu_0 t) + \left(\frac{\delta\alpha}{\delta q}\right)_0 q E_0\, cos(2\pi\nu_0 t) \tag{2.27}$$

$$= \alpha_0 \cdot E_0\, cos(2\pi\nu_0 t) + \left(\frac{\delta\alpha}{\delta q}\right)_0 q_0 E_0\, cos(2\pi\nu_0 t)\, cos(2\pi\nu_m t) \tag{2.28}$$

$$= \alpha_0 \cdot E_0\, cos(2\pi\nu_0 t) + \frac{1}{2}\left(\frac{\delta\alpha}{\delta q}\right)_0 q_0 E_0 \{cos[2\pi(\nu_0 + \nu_m)t] + cos[2\pi(\nu_0 - \nu_m)t]\} \tag{2.29}$$

In a classic interpretation, the first term corresponds to an oscillating dipole: a photon with the frequency ν_0 (Rayleigh-Scattering). The second term corresponds to Raman scattering processes with the frequency $\nu_0 + \nu_m$ (anti-Stokes) and $\nu_0 - \nu_m$ (Stokes). If $(\delta\alpha/\delta q)$ is zero, the Raman scattering also becomes zero. This shows how a change in polarizability is necessary in order for Raman bands to be active.

As described in formula 2.31 conservation of energy-momentum requires that the energy and momentum of the scattered photon isE_E and k_S is equivalent to the sum or difference of the incident photon and the phonon [135].

$$E_S = E_i \pm E_q \tag{2.30}$$

$$k_S = k_i \pm q \tag{2.31}$$

Incident radiation is scattered at a given molecule. This results in the emission of a phonon in the molecule and a photon with reduced energy back into the environment. The difference in

energy in the incident and the emitted photon is called stokes-shift and is in good approximation equal in energy to the phonon emitted into the scattering material.

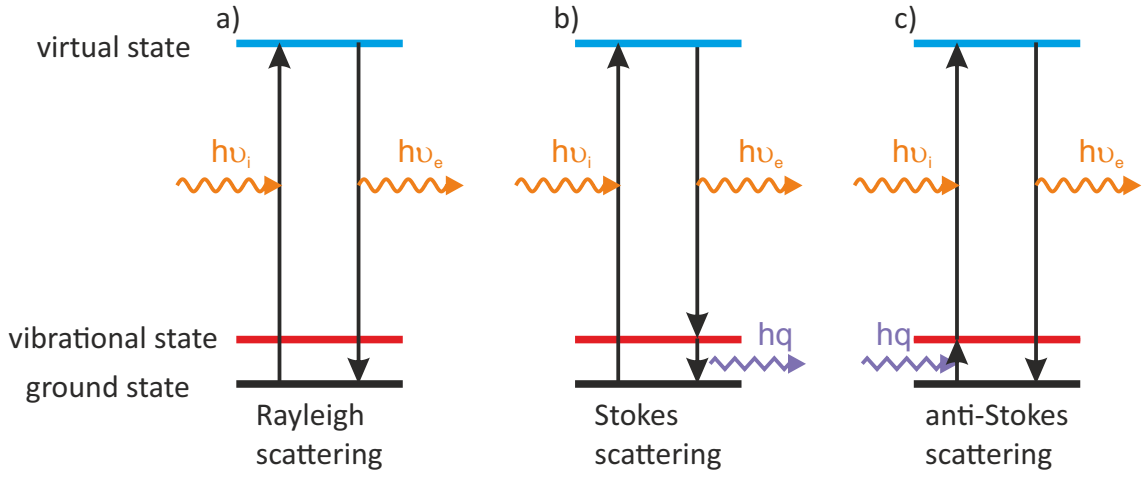

Figure 2.18: Illustration of the three principal processes underlying Raman spectroscopy. a) Rayleigh scattering: Incident light is excites the system into a virtual state and a photon with approximately the same energy but a different wave vector is emitted. b) Stokes scattering: The incident photon is absorbed into a virtual state. Upon emission both a batochromicly shifted photon and a phonon are emitted. The phono corresbonds to the first excited vibrational state. c) Anti-Stokes scattering: A phonon is absorbed, resulting in an exication into the first vibronic state. From this state an hypsochromic photon is emitted.

As shows in 2.18 three different scattering processes can occur when a photon interacts with a molecule. Scattering can be understand as an excitation into a virtual energetic states, which relaxes under emission of a photon either into the ground state or an vibronic state. It should be noted that virtual states are not real observable states. Their existence arises from the description of Raman scattering via perturbation theory. They do not however represent an actual solution to the Hamiltonian but a transition between initial and final state, induced by the interaction with the oscillating electromagnetic field of the photon. In order for the Raman effect to occur, an electronic state above the ground state has to exist, even if no resonant transition occurs.

If the relaxation results into a return in the ground state the process is described as Rayleigh scattering. This is the by far most likely outcome with a probability that is roughly a million times higher than that of the two other scattering events. Stokes scattering occurs when the radiative relaxation ends in the first excited vibronic state, resulting in the emission of a phonon into the material to return to ground state. Anti-Stokes scattering is even less likely, since it requires a phonon to exist in order to be possible at all. The average number of photons n with a given energy q is given by the Bose-Einstein distribution 2.32.

$$n = \frac{1}{e^(E_q/k_B T) - 1} \tag{2.32}$$

Since Raman spectroscopy is usually performed at room temperature or below the Bose-Einstein distribution heavily favors excitations from the ground state.

2.4.2 Resonant Raman spectroscopy

The Raman effect does not require a resonant excitation. However, the overall low intensity usually necessitates long measurement times, which is not always feasible as experimental conditions can not always be relied upon to be stable for an extended amount of time. To alleviate this issue, Raman spectroscopy can be performed with light which is resonant to an electronic transition of the sample, as illustrated in 2.19.

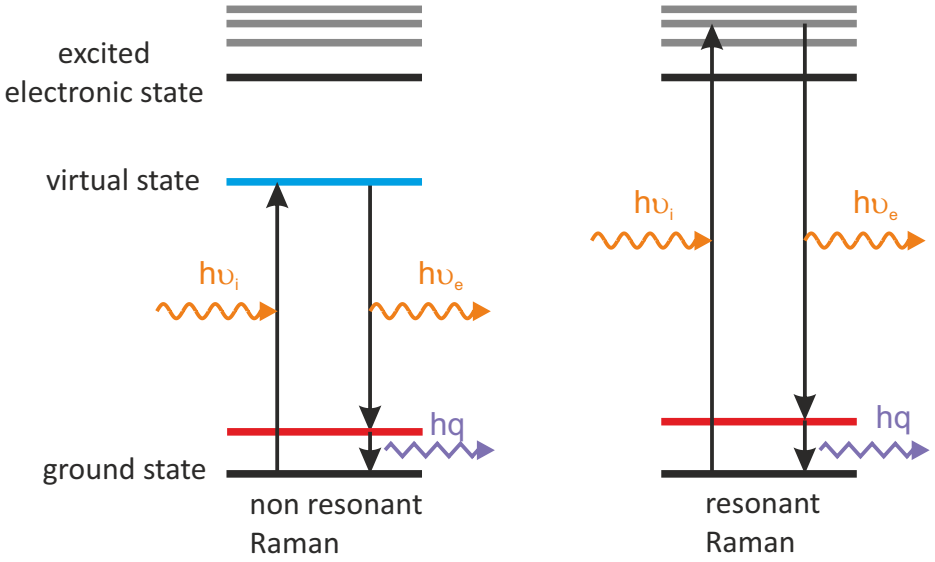

Figure 2.19: Non-resonant Raman spectroscopy usually uses excitation energies that lie below the excitation energy of any actual electronic state. However if the excitation energy is resonant with a real electronic state the observed Raman effect is increas by a factor of approximately 10000.

Resonant Raman is roughly a thousand times more intense since the incident photon couples strongly to the probed molecule. Thus the induced electric dipole is considerably stronger, which intensifies the observed Raman effect. Resonant Raman is widely used in carbon nanotube research for two reasons: Firstly, Raman experiments on singular carbon nanotubes require unreasonably long measurement times. Secondly, it allows easy distinction of different carbon nanotube chiralities since only the signal of the chirality which meets the resonance condition is intensified[14].

Resonant Raman amplification is strongly dependent on the resonance conditions. A quantum mechanical description of the Raman process is necessary to understand this in more detail: We assume an initial electronic ground state $|0\rangle$ with no excitons present. The excited state shall be denoted as $|a\rangle$ with the associated excitonic transition energy E_a The Raman scattering probability for a given phonon mode near E_a can be approximated by the following expression[136]:

$$P_p h(\omega_i) \approx \left(\frac{2\pi}{\hbar}\right) \left| \frac{\langle 0|\mathscr{H}_{eR}(\omega_i)|a\rangle \ \langle a|\mathscr{H}_{e-ion}|a\rangle \ \langle a|\mathscr{H}_{eR}(\omega_s)|0\rangle}{(E_a - \hbar\omega_i)(E_a - \hbar\omega_s)} + C \right|^2 \tag{2.33}$$

$\mathscr{H}_{eR}$ is the Hamiltonian for the electron-radiation interaction, while $\mathscr{H}_{e-ion}$ is the Hamiltonian for the electron-phonon interaction. C is a constant background, which consists of the non-resonant contributions, which can be neglected under resonance condition. Of particular importance are the terms containing $(E_a - \hbar\omega i)$ or $E_a - \hbar\omega_s$. Both of these terms will enhance the scattering probability when $\hbar\omega_s$ is close to E_a. Consequently, the resonance condition applies both the incoming and scattered photon, which will be referred to as incoming resonance and outgoing resonance in the remainder of the text. C denotes non-resonant contributions. However, in this formulation, the energy denominator would become infinite at perfect resonance $E_a = \hbar\omega_i$. In order to avoid this, the intermediate state $|a\rangle$ can be given a finite lifetime r_a. Consequently E_a has to be replaced by a complex energy $E_a - i\Gamma_a$, where Γ_a is the dampening constant, related to r_a by $\Gamma_a = \hbar/\tau_a$. The overall Raman scattering probability with free excitons is given by [136]:

$$P_p h(\omega_i) \approx \left(\frac{2\pi}{\hbar}\right) \left| \frac{\langle 0|\mathscr{H}_{eR}(\omega_i)|n\rangle \ \langle n|\mathscr{H}_{e-ion}|n'\rangle \ \langle n'|\mathscr{H}_{eR}(\omega_s)|0\rangle}{(E_n - \hbar\omega_i - i\Gamma_n)(E_{n'} - \hbar\omega_s - i\Gamma_{n'})} \right|^2 \tag{2.34}$$

$|n\rangle$ denotes the nth excitonic state. In SWNTs, the excitonic levels are usually sufficiently far apart, energetically speaking, that it is the only transition relevant to resonant Raman considerations. Consequently, the overall observed resonant Raman intensity of a band depends on the resonance of both the incoming and outgoing photon.

2.4.3 Raman modes in single-walled carbon nanotubes

The three principal first-order transitions are illustrated in image 2.20 are the G^+, G^- and radial breathing mode (RBM). The G^+ is a longitudinal stretching mode, with the vibration occurring along the tube axis. As a result, it is independent of the chirality of the nanotube. The G^- band is a transversal mode moving along the circumference of the tube. It is strongly diameter dependent, as the curvature of the tube changes the character of the C-C bonds, moving it closer to a sp^3 hybridization model with increasing curvature. Finally, the radial breathing mode, which is inversely proportional to the CNT diameter, is unique to every SWNT species. While the other two modes can also be found in graphene, this mode is unique to SWNTs and can be used to identify individual chiralities.

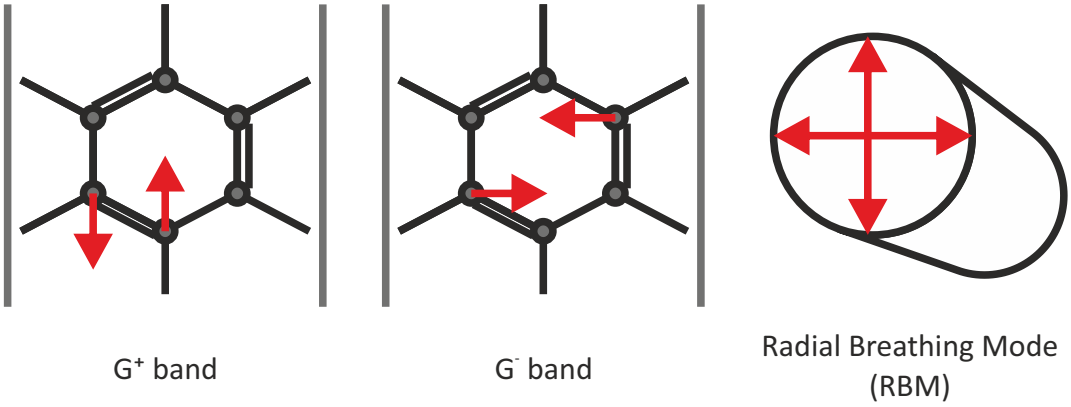

Figure 2.20: a) The G^+ mode represents the longitudinal streching mode along the tube axis. Since the C-C bonds involved are very similiar the G^+ mode shows little variation across all types of SWNTs. The The G^- is the transversal mode. Since the vibration occurs alongside the circumfence of the tube, the curvature and thus the chirality of the tube greatly influence the G^- position. c) The radial breathing (BRM). The RBM is characteristic for every tube, since it is inversly proportional to the tube tube diamter.

Of primary interest in this dissertation was the G^+ and G^- band of the 6,5 chirality. which typically are found at 1590 cm^{-1} and 1530 cm^{-1} respectively. The frequency of the RBM is considerably lower at 100 cm^{-1} to 500 cm^{-1}. All of these processes are first-order Raman transitions, but there are several second-order processes that can occur.

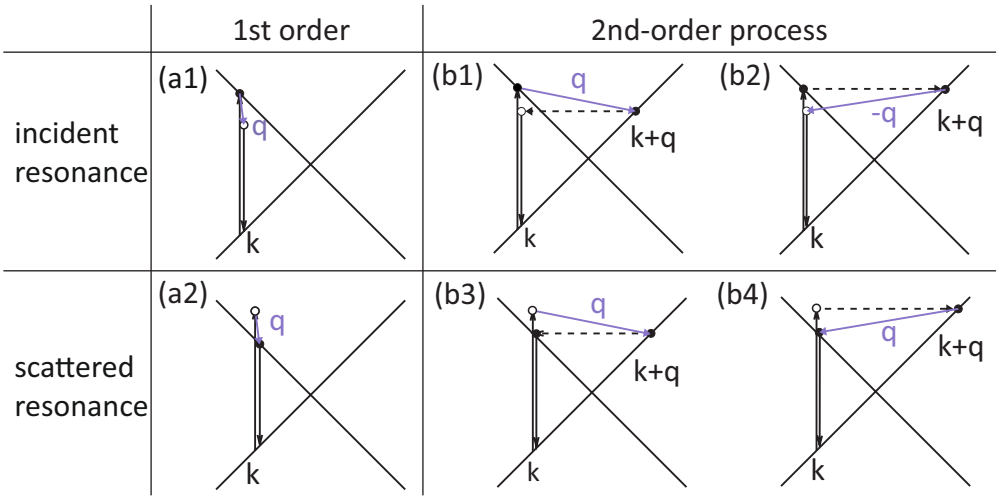

Figure 2.21: First and second order Raman processes in SWNT. (A) First order processes. (b) one-phonon second order. Figure reproduced from Dresselhaus et al. [14].

In second-order Raman the scattering wave vectors **q** and **-q** become involved (see figure 2.21). After excitation into an excited state at the k point, the electron is scattered, changing momentum. It is then scattered back to the k point and emits a photon upon recombination with the hole there. In SWNTs, the most notable second-order effect is the D defect band. It is the direct result of scattering at defect sites after excitation. Therefore this band increases in strength with increasing defect concentration. The G^+/D ratio can be used to quantify the number of defects in graphene and SWNTs [137–139].

2.5 Electron paramagnetic resonance spectroscopy

Electron paramagnetic resonance spectroscopy (EPR) is valuable to investigate unpaired electrons and their dynamics. It has proven particularly useful for investigating metal complexes and organic radicals. In this thesis, its ability to observe isolated charges will be used to investigate charges on carbon nanotubes. The following sections provide the necessary theoretical background to understand the basic principles behind this method. Unless noted otherwise this section is based on the textbook *Electron spin resonance* by Charles Poole[140].

Zeeman effect

The physical effect underlying EPR is the Zeeman-Effect. It describes the splitting of a spectral line in the presence of a magnetic field. The magnetic moment $\boldsymbol{\mu}$ of an electron with a spin $\boldsymbol{S}$ = 1/2 is given by the following expression:

$$\boldsymbol{\mu} = -g_e \beta_e \boldsymbol{S} \tag{2.35}$$

β_e ist the Bohr magneton and g_e is the dimensionless electron g-factor, which for a free electron has a value of 2.0023. The energy for the interaction of this electron with a magnetic field is

$$E = -\boldsymbol{\mu_e} \cdot \boldsymbol{B} = g_e \beta_e \boldsymbol{S} \cdot \boldsymbol{B} \tag{2.36}$$

Under most experimental conditions the magnetic field is directed along one axis. If we define this axis as the z-component this equation simplifies to the following expression:

$$E = g_e \beta_e B S_Z \tag{2.37}$$

For an electron with a spin of $\boldsymbol{S}$ = 1/2 this interaction produces two energy states:

$$E_\pm = \pm \frac{1}{2} g_e \beta_e B \tag{2.38}$$

These two different states are arbitrarily labeled as spin-up, (↑), + 1/2 and α or spin-down, ↓, -1/2 and β corresponding to anti-parallel and parallel orientation of S_Z to the magnetic field. As illustrated in figure 2.22 an oscillating magnetic field with the frequency ν can induce the EPR transition from up to down state if the resonance condition

$$\Delta E = E_+ - E_- = h\nu = g_e \beta_e \boldsymbol{B_R} \tag{2.39}$$

is satisfied.

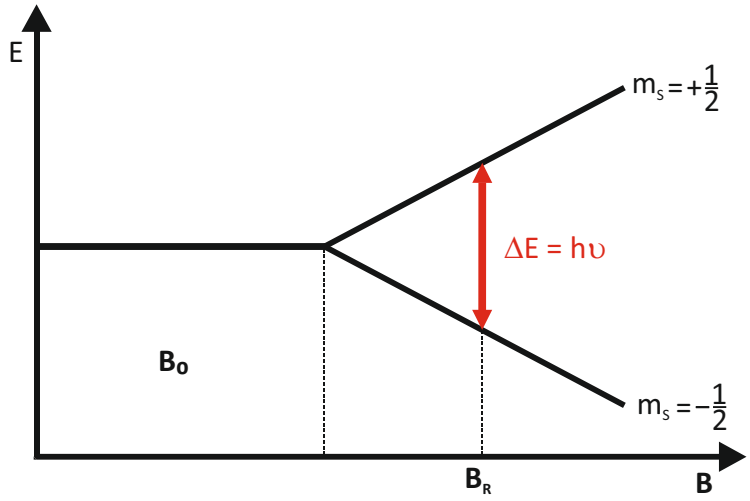

Figure 2.22: Visualisation of the Zeeman effect. With increasing magnetic field strength the energetic splitting between up and down state inreases in magnitude. The transition between those states can be spectroscopically probed forming the basis for EPR.

ΔE is the energy of an incident photon that induces this transition, often called a spin-flip. That Interaction forms the backbone of EPR spectroscopy and allows the characterization of unpaired spin systems like free electrons or organic radicals. In practice most EPR experiments are performed using a fixed excitation frequency and adjusting the Zeeman-splitting via the magnetic field strength to produce their spectrums. The fixed frequency makes the use of resonators around the sample possible, which can increase the effective field strength immensely.

Field modulation

In order to improve the signal/noise ratio, EPR spectroscopy uses lock-in detection. Another set of magnetic coils modulates the field strength at the sample at a given frequency μ. This shifts the resonance of the spin-flip and consequently induces an oscillation in the absorbance. This effect is illustrated in image 2.23.
Consequently, the signal oscillates with the frequency μ, enabling the use of a lock-in amplifier, which drastically improves the signal to noise ratio by filtering out the noise of all other frequencies. As a result, the observed EPR signal is the first derivative of the absorbance with the approximation $\frac{dI}{dB} \approx \frac{\Delta I}{\Delta B}$.

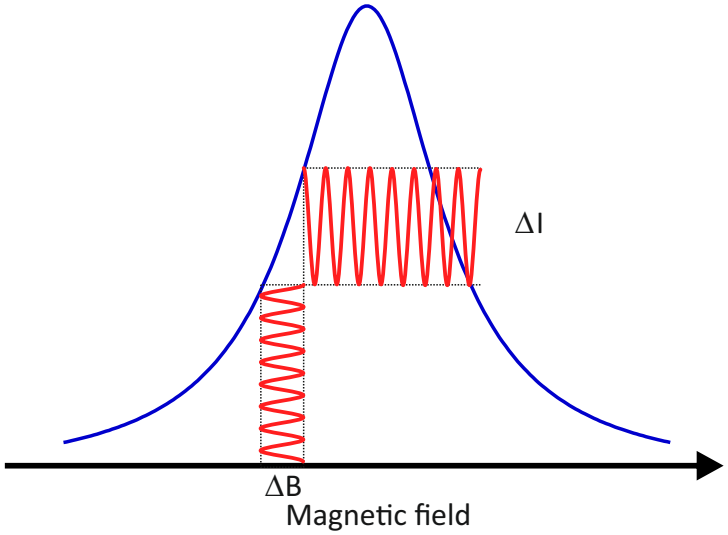

Figure 2.23: Illustration of the field modulation and the resulting signal. The blue line indicates the absorbance at a given magnetic field. With the oscillating field modulation ΔB the signal oscillates by ΔI at the same frequency.

Quantitative EPR

EPR can be used to measure the amount of spins in a given sample. In order to do so the EPR signal needs to be integrated twice, since the actual signal is the first derivative of the Signal due to use of lock-in detection as elaborated previously. First a reference sample is measured with a know density of spins. These materials can be commercially purchased and allow for a reliable calibration of the EPR spectrometer. In the case of our experiment 1,3-bis(diphenylene)-2-phenylallyl (BDPA) (Lewis formulae in figure 2.24) was used.

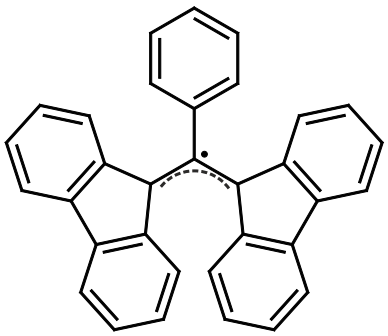

Figure 2.24: Lewis formulae of 1,3-bis(diphenylene)-2-phenylallyl (BDPA), the EPR reference sample used for spin quanitification in this experiment.

The magnetic transition moment is generally a lot weaker than the electronic transition moment. This necessitates higher sample concentrations than what is usually required in optical experiments, in the order of 10^3 to 10^4 more.

3 Preparation of single walled carbon nanotube Samples

3.1 Introduction and motivation

As already mentioned, a variety of methods can produce SWNTs. However, all of them only provide limited control over the chirality, diameter, length, and electronic properties. To this day, this remains a limiting factor when it comes to potential applications and research alike. Continuously refining existing preparation is therefore imperative to advance the field of low-dimensional materials. However, to produce samples suitable for spectroscopic investigation, it is first necessary to remove non-SWNT material and isolate singular tubes. Otherwise, most SWNTs can not be probed since they are encased between other nanotubes. Furthermore, the strong impact of dielectric screening on the electronic properties necessitates a mostly homogeneous environment to produce meaningful data, which agglomerates do not provide[141].
The current literature on techniques for large-scale preparation of SWNT suspensions only provides limited insight into why specific preparation methods are more or less effective. The following chapter attempts to quantify the difference in sample quality between sonication and shear-mixing. Furthermore, we explore some of the possible mechanisms underlying the dispersion process. The preparation technique used in this chapter provided the samples for most of the other experiments in this dissertation. Many experiments, photoluminescence, in particular, are very sensitive to defects on the SWNTs. Therefore high quality and the ability to reliably produce SWNT suspensions is essential.
While the production of SWNT-Suspensions is already well documented in the literature, certain aspects of the preparation steps are often neglected or poorly documented, resulting in less than ideal reproducibility. The following section aims to elucidate some of the often neglected aspects of sample preparation, like the impact of sonication on the dispersion agents. Photoluminescence quantum yield can be used to gauge the quality of a given sample since it quickly diminishes with increasing defect density. In this dissertation, it is the primary method to characterize the sample quality during the various preparation steps.
The following chapter will first provide an overview of the currently established methods and their known advantages and disadvantages. Then the experimental procedures used in this dissertation are explained in detail. Finally, the resulting experimental data and conclusions that can be drawn from them are presented.

3.2 State of the art of SWNT preparation

SWNTs, as produced, usually form agglomerates of SWNTs intermixed with impurities and catalyst residues. The large surface area relative to their volume means that SWNTs have strong π-π interactions with adjacent tubes.[142, 143] Consequently, they form tightly packed bundles, which are difficult to break. The most common method to overcome this is to either sonicate or shear-mix the bundled material in a solution of a dispersion additive, which inhibits re-aggregation after the bundles have been separated. Afterwards, centrifugation removes the remaining undispersed raw material and other impurities. The following chapter elaborates on these different steps in the preparation process.

3.2.1 SWNT synthesis

SWNTs are synthesized via catalyzed growth of amorphous carbon. A variety of methods can be employed for the production of carbon nanotubes, such as arc discharge[144, 145], laser ablation [146, 147], plasma torch[148] and chemical vapor deposition (CVD)[149].
The SWNT material SG65i, used in this thesis, is commercially produced via a CVD process called CoMoCat. As the name indicates, a cobalt-molybdenum catalyst is used with a process temperature of 700 °C to 950 °C and a pressure of 1 bar to 10 bar. These CVD parameters and catalysts are optimized for the synthesis of (6,5) SWNTs. The resulting raw material is further enriched to increase (6,5) content, which results in an SWNT content of 70 % of the total carbon amount, above 50 % of which are of the (6,5) chirality[150]. The length of the tubes is about 1 µm[150].Despite the high content of (6,5), SG65i still contains a substantial amount of amorphous carbon, catalyst remains and other SWNT chiralities. While this material provides an excellent baseline to work from, further processing steps are necessary, elaborated in the following sections.

3.2.2 Dispersion additives

SWNTs by themselves are not soluble in any solvent environment, but with the use of dispersion additives, it is possible to produce stable SWNT suspensions. Two classes of chemical compounds have proven themselves particularly effective: Tensides and polymers. Tensides like sodium dodecyl sulfate or sodium deoxycholate have a lipophile and a hydrophilic component. The tensides form micelles around SWNTs with their lipophile side pointing towards the tube while the hydrophilic component points towards the aqueous environment, making suspensions in water possible.[43].

However, in this thesis, SWNTs were only stabilized in organic solvent environments, mediated by a polymer additive. Generally, polymers also allow for a higher degree of selectivity and

perform better at isolating singular tubes. Poly[(9,9-dioctylfluorenyl-2,7-diyl)-alt-co-(6,6'-2,2'-bipyridine)] (PFO-BPy)[151] for instance is particularly selective towards semiconducting (6,5) Nanotubes[152–154], Sensitivities of up to 99.98 % have been reported [6]. PFO-BPy is an organic copolymer consisting of alternating segments of fluorenyl und bipyridine, which is primarily soluble in apolar solvents like toluene and THF. Its Lewis-structure is shown in figure 3.1 a).

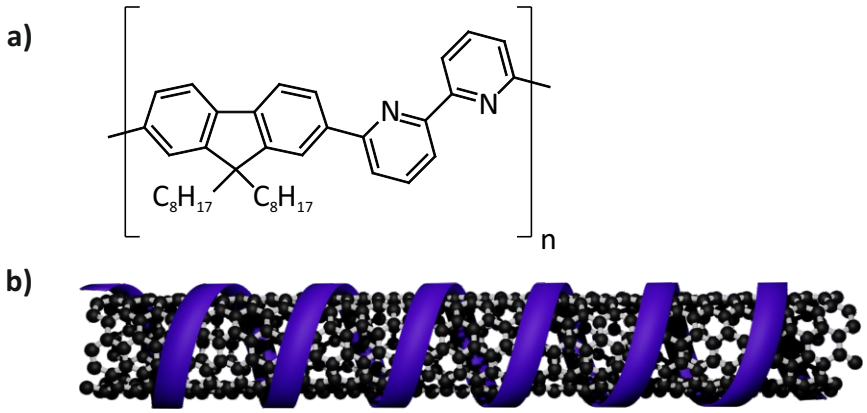

Figure 3.1: a) Lewis formula of PFO-BPy. b) Illustration of SWNTs are stabilized by PFO-BPy. The polymer helically wraps around the Tube, thus isolating it from other CNTs and stabilizing it in the solvent environment

PFO-BPy stabilizes SWNTs by wrapping around them in a helical structure, as illustrated in 3.1 [155]. The helix angle is 14°$\pm$2°, although the precise geometry of the SWNT/PFO-BPy complex is also dependent on the solvent environment [154]. The helical structure appears to favour a particular tube diameter of around 7.6 Å, corresponding to the (6,5) SWNT chirality. The primary interaction between tube and polymer are π-π interactions [156]. At the time of writing, it is still unclear why the polymer selectively wraps semiconducting tubes and not metallic ones with comparable diameters. This wrapping behaviour may also be the reason for its superior performance when isolating SWNTs. Tenside micelles can, in principle, form around SWNT bundles as well, while a diameter selective polymer will not readily wrap aggregates of several tubes [157].

3.2.3 Debundling

In order to break up SWNT bundles, the π-stacking interaction between SWNTs has to be overcome. This requires the application of a considerable amount of shear force, which sonication[158] and shear-mixing can provide.

Tip sonication

Tip-sonication produces its shear force through cavitation, generated by the acoustic wave of the sonication horn. The implosion of these cavities can result in extreme local conditions with temperatures of several thousand Kelvin and pressures of up to 1000 bar[159]. While this makes sonication an undeniably effective tool for debundling CNTs, it can unfortunately also damage the tubes themselves. One of the primary benefits of sonication is that it produces results considerably faster than other methods. The precise timescale depends on several experimental parameters, but generally, the high shear forces of horn sonication are the quickest way to break up SWNT bundles.
However, there are also downsides to this approach. An increase in sp3 defect density, reduction of average tube length and open holes in the SWNT structure have been reported as a result of prolonged sonication[160, 161]. Furthermore, ultrasonication can degrade polymers in solution, significantly shortening the polymer length[162, 163].

Shear mixing

The shear forces that lend the method its name are generated by pressing a fluid at high velocity into a volume with comparatively low speed. The concept of shear-mixing is illustrated in figure 3.2. A rotor presses the surrounding fluid through a grating while fresh fluid is sucked into the stator from below. The speed differential generates shear forces that can debundle SWNTs or other particles and agglomerates.

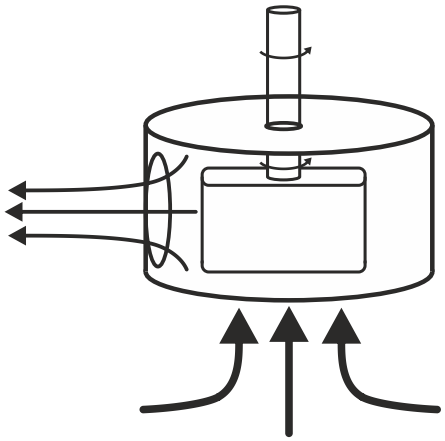

Figure 3.2: Schematic illustration of the principle behind shear force mixing. The arrows indicate fluid flows. The rotor ejects fluid through openings in the stator. Fluid is drawn from the fluid below. The speed differential of ejected fluid to the surrounding liquid causes shear forces, breaking up agglomerates.

Shear-mixing can be used to debundle SWNTs both with tensides[164] and with polymers[165]. Compared to sonication, the shear forces applied to the particles are much weaker. This means that the shear-mixing process is slower overall than horn sonication but also less destructive. SWNTs suspensions produced via shear mixing show higher average length distributions than sonicated samples. [165] Furthermore, there are no documented cases that shear force mixing damages polymers, which given the importance of polymers as dispersion additives, can have a considerable influence.

3.2.4 Centrifugation

Centrifugation as final processing step is used to remove non-dispersed raw material from suspensions. At lower forces is used to remove undispersed raw material and and amorphous carbon from the suspension. At higher centrifugal forces it can also sediment the SWNT material from the suspension itself. This, however, only occurs at relative centrifugal forces above 60.000 g[53]. The relative centrifugal forces (RCF) can be calculated via the following formula:

$$RCF = RPM^2 \cdot 1.118 \cdot 10^{-5} \cdot r \tag{3.1}$$

RPM denotes the rotation frequency in rounds per minute, while r is the rotor radius. Two centrifuges were used: For batches with a volume of 20 mL or less a Biofuge 15 benchtop device from Heraeus Sepatech and for any batch with a larger volume, a Rotina 35R from Hettich Zentrifugen. Centrifugation with the Biofuge 15 usually takes about 5 minutes at the maximum speed of 14000 rpm ($\approx$ 15000 g), while the Rotina 35R usually requires 45 minutes, due to a significantly lower speed of 4000 rpm ($\approx$ 2700 g).

3.3 Experimental aspects

3.3.1 Concentration measurements of SWNT suspensions

The absorption band of SWNTs can be used to quantify SWNTs in suspensions. In samples with only one chirality, the first excitonic transition does not meaningfully overlap with other signals. The oscillator strength combined with the molar extinction coefficient can then be used to calculate the mass content of a given suspension of (6,5) SWNTs.[166]:

$$c_C = B\frac{\Delta_{fwhm} OD}{fd} \tag{3.2}$$

where c_C is the molar carbon concentration, d the cell's optical patch length, and f the oscillator strength. OD is the peak optical density of the suspension at the excitonic transition, which is found at 1000 nm. The FWHM is the full-width half-maximum of this peak. Together, these two values essentially measure the oscillator strength of this transition. For convenience a constant $B = 5.1 \times 10^{-8}$ mol L cm nm^{-1} is defined, using common units used in the laboratory.

The absorption spectra themselves were recorded with an Agilent Cary 5000 UV-VIS spectrometer. It can cover a spectral ranger 170 nm to 3000 nm. The suspensions were placed in cuvettes (Typ 105.250-QS, Hellma Analytics) with an optical path length 1 cm. Absorption spectra were taken in the range of 200 nm to 1300 nm with a wavelength interval of 1 nm and an integration time of 1 s. The optical density at 1000 nm and the FWHM is determined via a Gauss fit, which provides the necessary data to calculate the molar carbon concentration according to formula 3.2.

3.3.2 Relative photoluminescence quantum yield

The relative PLQY of SWNT suspensions was determined by the ratio between absorption at the S_2 absorption band and the S_1 emission. Almost a 100 % of the excitation into the S_2 is transitions into the S_1 state and emits from there. Therefore, the S_1 emission can be considered to linearly proportional to the S_2 absorption.
Photoluminescence spectra of the suspensions were recorded using a custom setup built by Tilman Hain [167]. Tilman Hain's dissertation covers the precise setup and its capabilities. Therefore, only a brief summary of its capabilities and the chosen experimental parameters will be given.
As a light source, it uses an NKT SuperK Extreme super-continuum laser in combination with an NKT VARIA filter to produce laser emission in the spectral range of 400 nm to 840 nm with a bandpass of 2 nm to 50 nm. The Emission is spectrally resolved by an Andor Shamrock 303i-B spectrograph. It has two detectors, a CCD camera (ANDOR Newton CCD DU920P-OE) for the visible spectral region and an InGaAs (iDus PDA DU491A-1.7) array for the NIR spectral region. The spectrometer is controlled via LabView Application, specifically written for this device.
For capturing PL spectra, the InGaAs array in combination with a grating with a blaze wavelength of 1250 nm and 150 lines were used. The spectrometer slit was set to 50 µm. The total power of the excitation beam was at 7 mW at 568 nm to 570 nm with a 2 s exposure time. The absorption spectra were recorded with the same settings as described in section 3.3.1. Afterwards, the SWNT suspensions in cuvettes (Typ 105.250-QS, Hellma Analytics) were taken directly taken to the PLE spectrometer. The absorption spectrum was integrated between 568 nm to 572 nm, as well as the entire PL Spectrum at the excitation wavelengths of 568 nm to 570 nm. The ratio between these two integrals is relative PLQY, which given identical experimental parameters, can be used to observe relative changes in the PLQY of different samples.

3.3.3 Shear-Mixing

Suspensions were prepared with concentrations of 0.38 g L^{-1} of SG65i raw material and 0.5 g L^{-1} of PFO-BPy polymer. Both chemicals were dispersed in toluene (>=99.8 % analytical reagent grade) using a custom made glass vial, with a diameter of 5.08 cm and a length of 14 cm. All shear-mixing processes used the Silverson L5M laboratory shear mixer. A 1" Stator with a high-performance sieve with rectangular openings, optimized for suspensions, was used. The shear speed was set to maximum, resulting in a rotation speed exceeding the limit of the electronic display of 9999 rpm. The stator was slightly displaced from the centre of the vial, as described in the manufacturer manual. This displacement introduces a turbulent flow that ensures that the process impacts the entire volume of the suspension. For cooling, the glass vial was submerged in water at room temperature.

Figure 3.3: Image of the shear mixing setup. During normal operation the glass flask is submerged in a water bath to provide sufficient cooling.

The SWNT mass concentration during shear-mixing was tracked via absorption spectrometry. To do so 1 mL samples were taken, centrifuged and measured. After recording absorption spectra, the sample was added back to the suspension to avoid material loss. Once the SWNT E_{11}-Signal ceased to change meaningfully, the entire batch was centrifuged using the Rotina 35 benchtop centrifuge until no visible particles were present in the supernatant, which took up to 60 min. Should visible particles remain in the supernatant, 5 µm filter (Merck SMWP01300 filter) in combination with a filter holder (Merck XX3001200 Swinny filter holder) and lab syringes were used to remove them. Experiments involving ultracentrifugation used the Hettich Optima L-90 K with a type 70.1 Ti fixed angle rotor.

3.3.4 Sonication

In all sonication experiments, the samples were tip-sonicated with a Branson Sonifier 450 with the following settings: Duty-Cycle: 50 %, power output: 4.5 and 7.5 h run time. The sample composition for sonication was 0.5 g L^{-1} CoMoCat SG65i raw material and 1.0 g L^{-1} PFO-BPy in 15 mL toluene. As reaction container polystyrene 50 mL falcon tubes were used since, unlike most glass containers, they can easily withstand the stress induced by tip-sonication. The sonicator horn is submerged into the solution at a depth of about 1.5 cm. It is imperative that the horn is placed precisely into the middle of the tube. Otherwise, the sonication pulses push the suspension up the reaction container walls. This causes increased evaporation and introduces air bubbles into the suspension, which lowers the sonication efficacy.

Figure 3.4: Image of the sonciation setup. The falcon tube is submerged in an ice bath during operatino, to ensure proper cooling.

Sonication at this intensity level produces a considerable amount of heat. Therefore each batch is cooled via an ice bath, which is renewed every 1.5 h. Once sonication is complete, centrifugation via the Biofuge 15 benchtop centrifuge removed the undispersed raw material.

3.4 Results and Discussion

3.4.1 Dispersion efficiency comparison between sonication and shear-mixing

Several aspects have to be taken into consideration when choosing between the two dispersion methods. Sonication tends to be a more destructive method shortening both nanotubes and polymers alike,[163] as well as increasing the defect density in SWNTs. However, shortening the polymer may positively affect the SWNT yield in suspensions. Comparing the SWNT mass yield between shear-mixing batches with varying polymer yields shows polymers with lower average molecular weight generally result in higher SWNT yield. In extreme cases, such as a polymer with an M_w of 99.000 M Dalton no measurable amount of SWNTs could be dispersed in solution. This particular polymer batch was also almost insoluble in any kind of solvent. After centrifugation, no polymer or SWNTs could be found in the absorption spectra of the solution. Interestingly sonication shows no sensitivity towards the polymer length, indicating that the harshness of the method might positively impact overall yield.
To confirm this investigation the previously unusable polymer-batch with an average molecular weight of 99.000 Dalton was sonicated for 7.5 h, with identical parameters as a usual sonication based SWNT process. The sonicated PFO-BPy material was then used to shear-mix an SWNT sample as described previously. Contrary to the previous attempt at using this polymer for shear-mixing this batch of PFO-BPy, a considerable yield can be obtained. Figure 3.5 shows a comparison of shear-mixing with and without sonication of PFO-BPy.

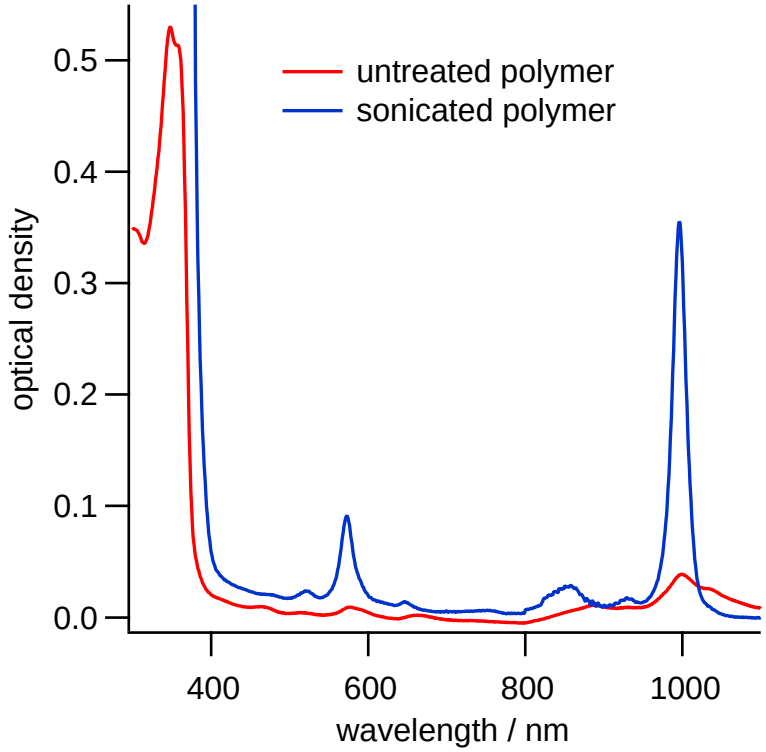

Figure 3.5: Absorption spectra of shear-mixed SWNT suspension with and without previous sonication, with otherwise same sample processing technique. Both samples used the same batch of SWNT raw material and PFO-BPy. The shear-mixing times are 29.17 h for the untreated sample and 11.17 h for the treated sample

The signal at 360 nm can be attributed to the $\pi \rightarrow \pi^*$ transitions of PFO-BPy. Without sonication, this signal is weaker than in sonication or shear-mixing batches with high yield, which in SWNT suspensions is usually concentrated enough to saturate the absorption signal at this wavelength. Combined with an only negligible signal at 1000 nm, which indicates a negligible SWNT concentration, it seems that polymer batches with high average molecular weight can only be dissolved to a minimal extent, reducing the amount of polymer available for wrapping SWNts. Another possible explanation is that SWNTs wrapped with long polymer chains tend to aggregate into larger particles, which are then lost in the centrifugation step. Consequently, their efficacy when it comes to stabilizing SWNT is also greatly reduced. In stark contrast to that, the sonicated polymer can be used to produce stable suspensions via shear-mixing, even if not to the same degree as pure sonication does.

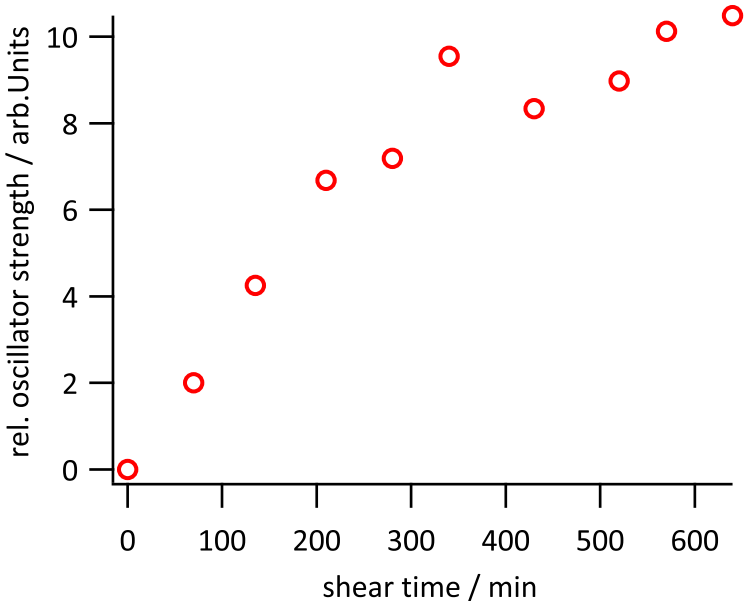

Figure 3.6: The relative oscillator strength represents the integral of the SWNTs S_{11} peak over the energy domain in electron volt. This value is linearly correlated to SWNT concentration. Over time the yield increases, approaching a maximum value. The drop at 330 min is due to a pause in the shear-mixing process of about 8 h, which led to a small amount of reaggregation.

Generally, colloidal suspensions become less stable with increasing particle size [168]. As a result, shear-mixing yields for individual runs should always be expected to be lower than sonication since sonication reduces the size of SWNTs. Since sonication produces similar results irrespective of the raw material but can also increase the effectiveness of polymer alone, the reduction in SWNT length alone does not suffice as an explanation. It is well established in the literature that bath sonication reduces the molecular weight, effectively the length, of a polymer [163, 169]. Since tip sonication generally operates at much higher intensities than bath sonication methods, a considerable shortening of PFO-BPy is expected. This might explain why shear-mixed samples are very sensitive to the particular polymer batch used, which can vary considerably in average polymer length, while sonication is not.

While shorter polymer lengths are clearly beneficial, it not entirely clear why they are more effective in dispersing SWNTs. Longer polymers may be more likely to adsorb other SWNT/Polymer aggregates and thus form larger particles, which are subsequently lost during centrifugation. SWNT suspensions produced by shear-mixing tend to form flakes after several days of storage. These flakes seem to be loose agglomerates, which can be readily redispersed by shaking or mild sonication. This does not happen with sonicated samples, which indicates that shear-mixed samples can form larger agglomerates between different SWNT/PFO-BPy particles. Another possible explanation would be that longer polymer strands are less likely to wrap around the SWNT and thus does not result in stable formation. Long polymer does not seem to dissolve in toluene compared to shorter batches, as evidenced by the lack of absorption signal in the shear-mixed sample (figure 3.5). In that case, the reduced effectiveness would mean that less polymer is available for wrapping SWNTs. Most likely, both factors contribute to the lower yield with PFO-BPy polymer.

This might provide a pathway towards more efficient shear-mixing. Pre-selecting or synthesizing shorter polymer batches or using chemical or physical means to shorten existing batches could drastically increase SWNT-yield. Given that the size of SWNTs themselves is an essential factor in the overall SWNT mass yield, the concentrations achieved by sonication may give an upper limit for the maximum yield in shear-mixing.

3.4.2 Centrifugation

As mentioned in the previous section, centrifugation may also play a key role in the yield in the production of SWNT suspension. To test the impact of re-aggregation on the overall yield 0.57 g L^{-1} CoMoCat SG65i material was added to already stabilized and fully processed (6,5)-PFO/BPy suspension. This mixture was then put in a sonication bath for 15 min. Letting the sample rest for 2 h and then centrifuge results in an overall reduction of SWNT concentration of 97.9 %. The corresponding spectra are shown in figure 3.7a). This is not necessarily surprising as both are carbon-based substances with a large effective surface area. However, the implications for sample preparation are severe as the entire process basically aims to stabilize and isolate material which tends to do the exact opposite. An optimistic estimate puts the total yield of (6,5) mass during a complete sonication-based preparation at 2 %.

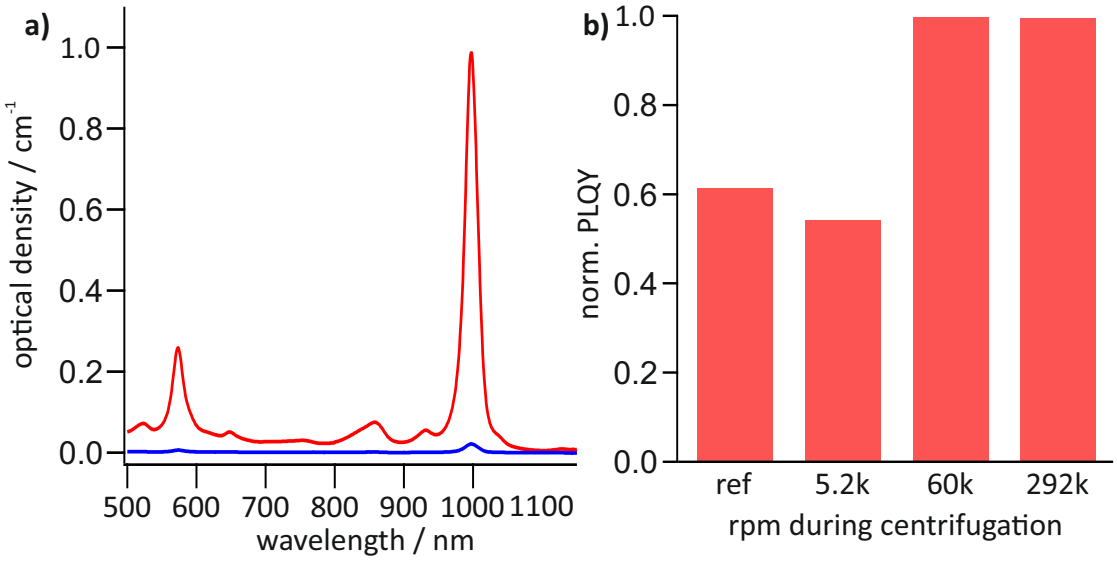

Figure 3.7: a)Absorption spectra of SWNT suspension before (red line) and after (blue line) treating the suspension with CoMoCat raw material. Integration over the E_{11} exciton transition energy (947 nm to 1087 nm) can be used to quantify the SWNT content of both suspensions[166]. The total loss of SWNT content was 98 %. b) Normalized PLQY at different centrifugation rotation speeds. The ref value indicates the orignal suspension, which was then centrifuged at different speeds.

This may indicate that most of the losses during the preparation of SWNTs suspension is not due to a failure to wrap SWNTs with dispersion additives but rather a failure to prevent wrapped

tubes from forming aggregates that are lost during centrifugation. Consequently the time between terminating shear-mixing or sonication and the subsequent centrifugation should be kept as short as possible to avoid unnecessary losses.
However, centrifugation may also provide another pathway for increasing sample quality at the expense of mass yield. If sufficient centrifugal force is applied, otherwise stable SWNT suspension can begin to sediment. Ultracentrifugation at three different speeds showed that the PLQY of the supernatant improves at higher speeds, as shown in figure 3.7. Generally, heavier particles should sediment during any centrifugation process. This would include longer SWNTs, which have fewer defects due to the tube ends also representing defects. Therefore a decrease in PLQY should be expected. Apparently, another factor at play more than makes up for the loss of longer SWNTs. The improved efficiency for removing SWNT bundles is the most likely cause since bundles generally have a lower PLQY than single SWNTs[157]. Given that the mass of a bundle significantly exceeds that of single tubes, they should be disproportionately more affected than those, which would be consistent with the observed relative PLQY values. In conclusion, ultracentrifugation may be another way to produce higher quality samples if only small amounts of SWNT suspension is required. Up to 90 % of the SWNT content is sedimented at rotation speeds higher than 60,000 rpm, so this method is primarily helpful for PL microscopy experiments, which require only minuscule amounts of SWNT but significantly benefit from high PLQY.

3.4.3 PLQY of shear-mixed and sonicated SWNT suspensions

Since defects present a quenching site for the diffusion-limited photoluminescence in SWNTs, the photoluminescence quantum yield (PLQY) present a good indicator for the amount of damage SWNTs incur during the preparation process. Comparing the relative PLQY of otherwise identical SWNT-samples makes it possible to compare the damaging effects of two different preparation techniques. As seen in 3.8 the PLQY decreases sharply with increasing sonication times. Since the value for shear-mixed samples lies below the shortest sonication times, it can reasonably be assumed that shear-mixing does also increase the defect densities in tubes.

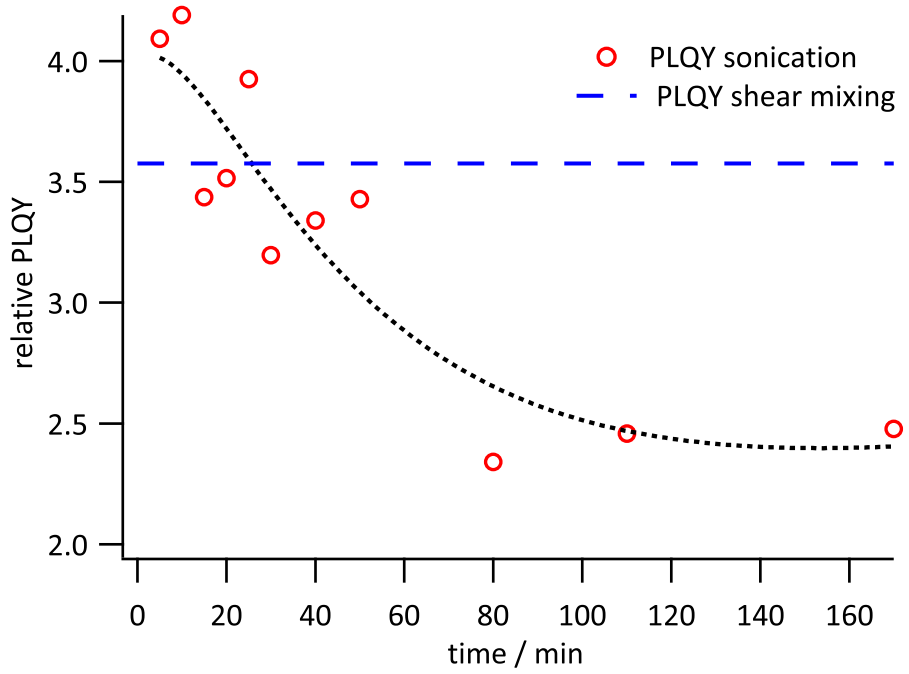

Figure 3.8: Changes in relative PLQY over sonication time. The red marks indicate the measured values of relative PLQY, with the dotted black line serving as guide to the eye. The dashed blue line is the PLQY value of a suspension produced by 20 h of shear-mixing.

However, shear-mixing does so at a considerably slower rate since the indicated value was measured after 20 h of shear-mixing. Short sonication times can help mitigate this issue. However, large scale production of high PLQY samples is not feasible without shear mixing since the overall mass yield of SWNT material is comparatively small. While both methods can yield high-quality samples, the shear mixed sample in a 50 ml batch had an optical density of 1.4, while the sonicated sample in 5 mL batch only had an optical density of 0.76 after 10 min sonication. Producing significant amounts of low defect materials is thus not possible via sonication, which prohibits experiments that require higher material concentrations like EPR or thin-film preparation.

3.4.4 Transient absorption signal

The decreased defect density can also be quantified by transient absorption (TA) spectroscopy. The exciton lifetime, measured by TA, can be used to calculate the average distance between quenching sites. These are typical defects in the SWNT structure or tube ends. Shorter tubes and higher defect concentrations thus decrease the exciton, similar to the drop in PLQY, since higher lifetimes makes radiative decay more likely. A TA map and the signal component at 1000 nm is shown in figure 3.9. The measurements and fits were performed by Pascal Kunkel.

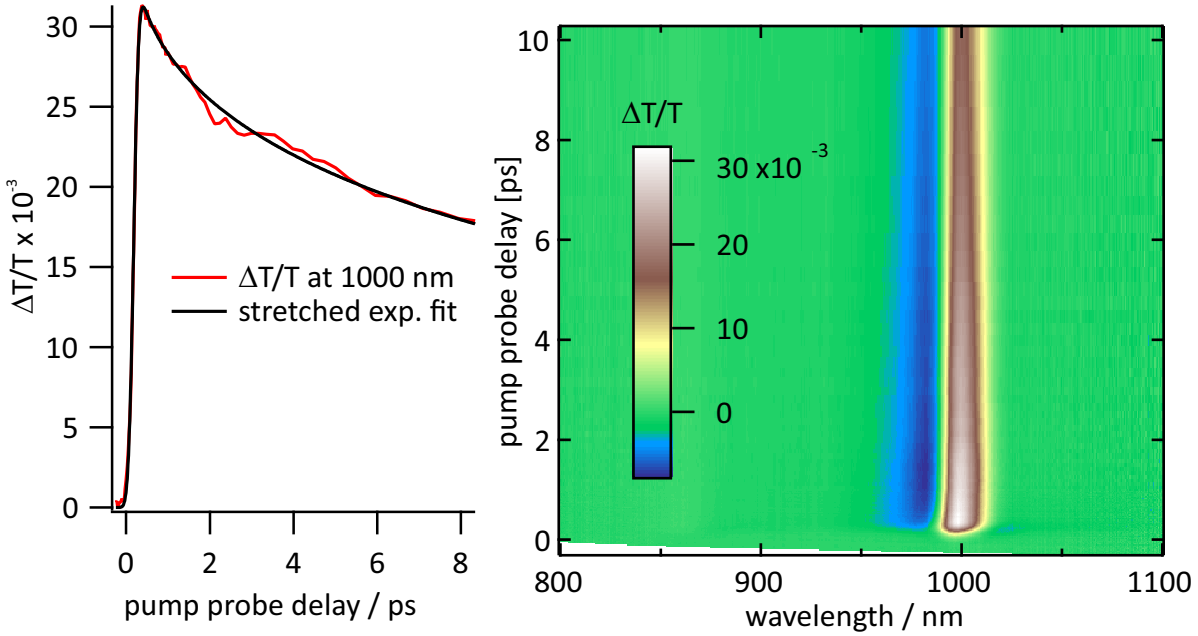

Figure 3.9: Transient absorption spectra of shear-mixed SWNTs. The stretched exponential fit in combination with the localized defect model results in average lifetime of 17.3 ps and an average distance between defects of 192.1 nm

By fitting a stretched exponential function to the data an average lifetime of 17.3 ps, which corresponds to a mean distance between defects of 192.1 nm or a defect density of 5.2 µm^{-1}. Mean tube length of shear-mixed (6,5) suspensions has been reported to be 1.82 µm[53]. Both tube ends are considered defects as well, which means the TA spectroscopy results indicate an average of about seven defects on the tube itself.

3.5 Summary

The impact of various steps in the preparation of SWNT suspension has been investigated on their effects on the PLQY, which serves as a proxy for the defect density of SWNTs.
The median length difference of shear-mixed and sonicated SWNTs has been documented before, but no comparison for the PLQY has been put into the literature thus far. Shear-mixing is far less detrimental to the PLQY than sonication. After 30 min of sonication, the PLQY falls below the value of suspensions which have been shear-mixed for 20 h and continues to do. The higher PLQY indicates a low defect density which was verified by transient absorption spectroscopy, which yielded a mean lifetime of 17.3 ps and consequently a mean distance between defects of 192.1 nm.
Comparing the effectiveness of sonication and shear-mixing for producing SWNT suspensions reveals that sonication is generally faster at the expense of sample quality. If the PLQY and defect density are critical factors, shear-mixing is preferable. Another significant result is the impact of polymer strand length on the SWNT yield. The increased performance of PFO-BPy as a dispersion additive through sonication could provide an opportunity to increase the yield of high-quality SWNT material substantially. At the time of writing, the impact of the polymer strand length has not been documented before.
Next, the impact of centrifugation on the PLQY was measured. The PLQY increases by a factor of two at higher centrifugation speeds, although up to 90 % of the SWNT material is sedimented at those speeds. The most likely cause for this increase is the more thorough removal of SWNT bundles, which display a lower PLQY than fully isolated tubes. Using centrifugation as a pathway to increase sample quality should be considered carefully. For purposes that require single isolated tubes, like microscopic experiments, centrifugation could provide another way of improving sample quality. On the other hand, this approach would be unconstructive when the SWNT material is aggregated, like in thin-film devices.

4 Photoluminescence microscopy of low-dimensional materials

Their reduced dimensionality of materials like SWNTs, graphene or TMDCs, gives rise to their fascinating properties but also to several experimental challenges. Their strong interactions with the dielectric environment make high-purity samples a necessity since impurities can drastically impact the properties of the material. Furthermore, every single low dimensional object is somewhat unique since they all show a variable amount of defects of different nature. Combined with their nanoscale size, sample preparation can be challenging and even when successful, conclusive data can only be obtained when probing individual objects. In order to identify and isolate signals of nanoscale objects, photoluminescence spectroscopy is an invaluable tool. Combined with a tunable laser and various detectors, it is possible to probe a broad range of low-dimensional materials and their heterostructures, even though only a few objects of interest are present in the sample. One objective of this thesis was the construction of a PL microscope capable of investigating a variety of different low dimensional materials. This includes the capability for PL imaging, spectroscopy and time-correlated fluorescence measurements. This microscope was then used to investigate potential sample preparation techniques, with the aim to produce and investigate heterostructures between SWNT and MoS_2 monolayer.
Firstly a brief overview of the current state of the art of heterostructures of two-dimensional materials is given. This is followed by an overview of the PL microscope and its various components. The next section explains the preparation techniques used to produce the heterostructure samples. The final section of this chapter presents the results of PL imaging and spectroscopy of these samples.

4.1 State of the art

Hybrid structures have been a focal point of scientific research. Given recent progress in 2D material preparation, most 2D monolayer materials have been thoroughly investigated. Heterostructures are at the point of writing less well researched due to the experimental difficulties in the preparation of these structures. The following section provides a brief outline of the documented cases of low-dimensional hybrid structures and their photoluminescence properties.

Of particular note is the formation of inter-layer excitons, which can show significantly increased PL-lifetimes of hundreds of nanoseconds [170–173] up to even microseconds [174]. For these excitons to form, the involved materials need to have a type 2 band alignment. As illustrated in image 4.1 the band alignment between (6,5) SWNTs and MoS_2 could be a promising candidate for the investigation of inter-layer excitons.

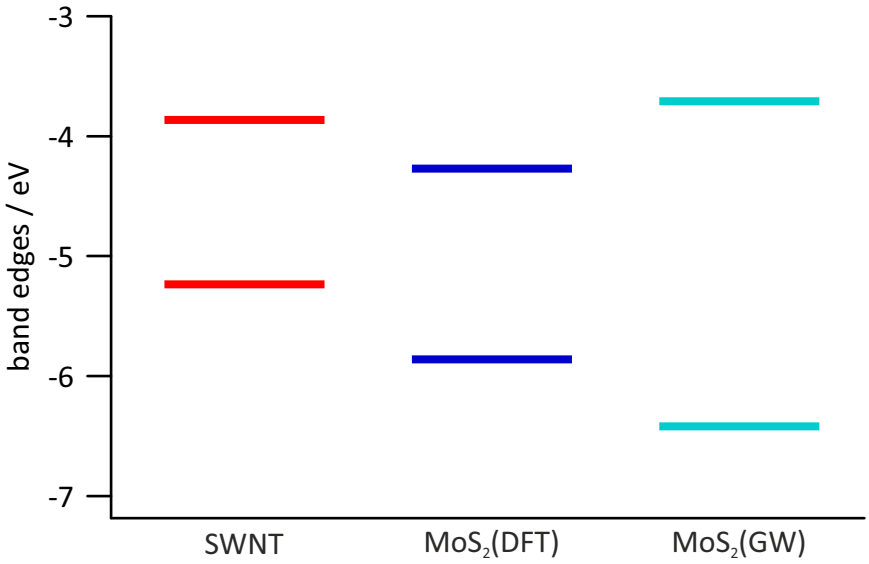

Figure 4.1: Band edges of SWNT and MoS_2. The SWNT bandeges have been experimentally determined The MoS_2 energies resulted from theoretical calculations taken from Zhang et al. [175].

As of right now, interlayer excitons have only been observed in 2D material heterostructures such as $MoSe_2$ and WSe_2 [176]. Theoretical calculations show that these two materials have the necessary Type II band alignment [177–179], which X-ray photoelectron spectroscopy has experimentally confirmed citeChiu2014. Contacting the two materials gives rise to a new spectroscopic signal at the contact area between the two materials, which is attributed to interlayer excitons [176]. This new signal is comparable in strength to the interlayer excitons at temperatures of 20 K but much weaker than them at room temperature [176, 180]. An example for interlayer exciton between $MoSe_2$ and WSe_2, as reported by [176] is shown in figure 4.2

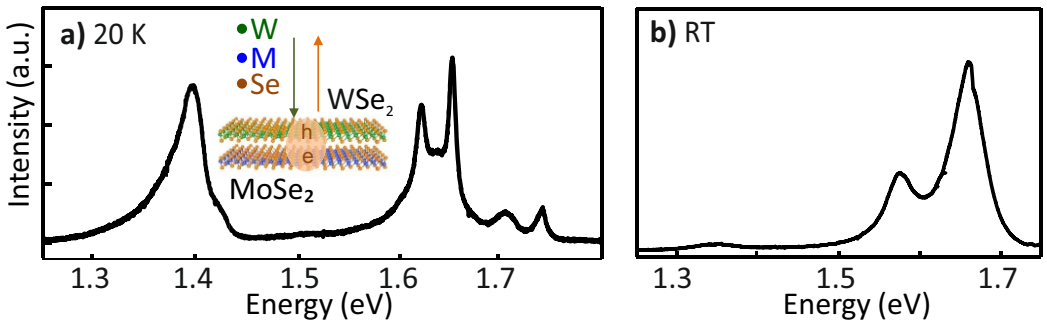

Figure 4.2: PL spectra of a $MoSe_2/WSe_2$ heterostructure at 20 K and room temperature. The emission at 1.5 eV to 1.75 eV are due to excitonic emission of the two materials. The signal between 1.3 eV and 1.4 eV are attributed to the interlayer exciton. Image reproduced from Rivera et al. [176]

The interlayer exciton bleaches the intra-layer PL signal [172, 180–188]. The charge transfer between two dimensional heterostructures is also reported to be extremely fast at below 50 fs [189].

4.2 Photoluminescence microscopy setup

As explained in the in theory chapter regarding SWNTs (2.1) and two-dimensional materials 2.2, the different low-dimensional materials show a wide spectral range in their absorption and emission behavior. In order to image and capture PL spectra of a wide variety of nanoscale objects, the microscopy setup as illustrated in figure 4.3 was constructed. In the following, the various components and their capabilities will be listed and explained in detail.

4.2.1 Objectives

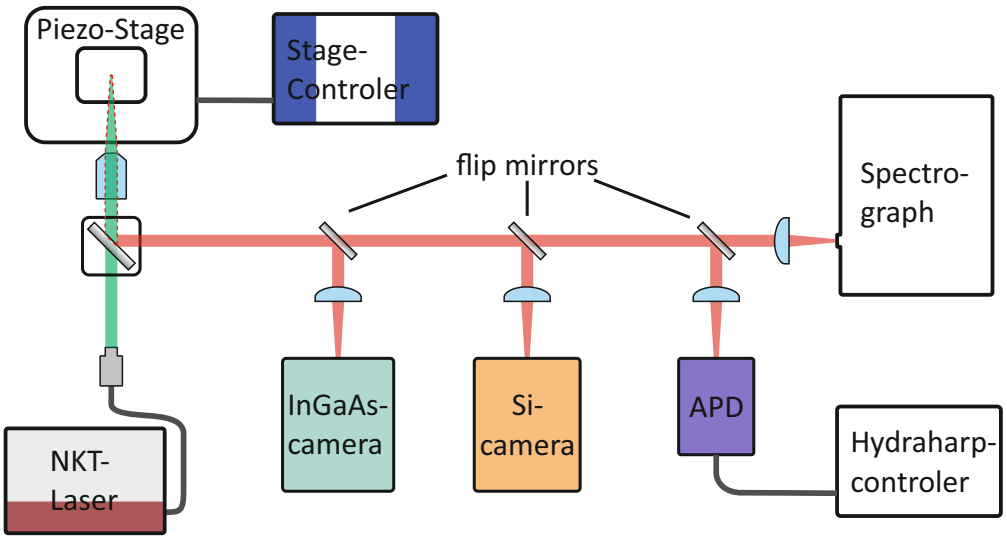

Figure 4.3: The setup uses and NKT photonics lasersystem as a variable emission light source for excitation (green beam). Via an objective a sample on the two-axis piezo stage is illuminated from below. The same objective collects emitted radtion (red beam) from the sample. The beamsplitter before the objective seperates emission and excitation light with the emissio beeing forwarded to multiple detection systems: An InGasAs camera of NIR imaging, an SI-camera for UV/VIS imaging, an avalanche photodiode for time-resolved photoluminescence and a spectrograph for spectral resolution.

In total three objectives are available for measurements. A 60x oil-immersion objective (*Nikon CFI Apo TIRF 60x*) with a numerical aperture of 1.49 and a variable working distance of 0.13 to 21 mm. Its high NA makes it ideal for observing weak emissions from single nanoscale objects, since it can capture emissions from a wide angle. It is less useful for large scale observations,

since it can only image a small area of interest and its short working distance necessitates careful sample preparation and handling.

For larger scale observation a 50x objective (*Olympus Mplan 50x*) with an NA of 0.75 and a working distance of 0.38 mm is available. The decreased NA makes it easier to find the focal plane compared to the 60x objective. Furthermore finding a focal plane is easier due to increased Railay length. This makes this objective suitable for quick imaging of samples or transmission methods without oil immersion.

Finally a 20x objective (*Nikon S Plan Fluor)* with an NA of 0.45 and a adjustable working distance of 6.90 mm to 8.20 mm allows for overview images, which can be important for larger objects or to quickly collect statistical information of a large number of objects. Its long working distance also enable the use of thicker and sturdier sample carriers, which can be helpful for some sample preparation techniques. As downside of using this objective is the comparatively low amount of fluorescence that can be picked up due to the small numerical aperture.

4.2.2 Sample-positioning

The microscopy uses three stages in total to position the samples. A illustration of the sample positioning setup is shown in figure 4.4. A high load vertical stage (Thorlabs VAP10) carries is used for rough sample positioning in the z-Axis. A stepper motorized xy stage (Lang MCL-2) placed on this z-translation stage is used for rough sample positioning, which can also be performed by hand. The precision of this stage is not sufficient for nanoscalig objects, but it can cover a range of about 10 cm.

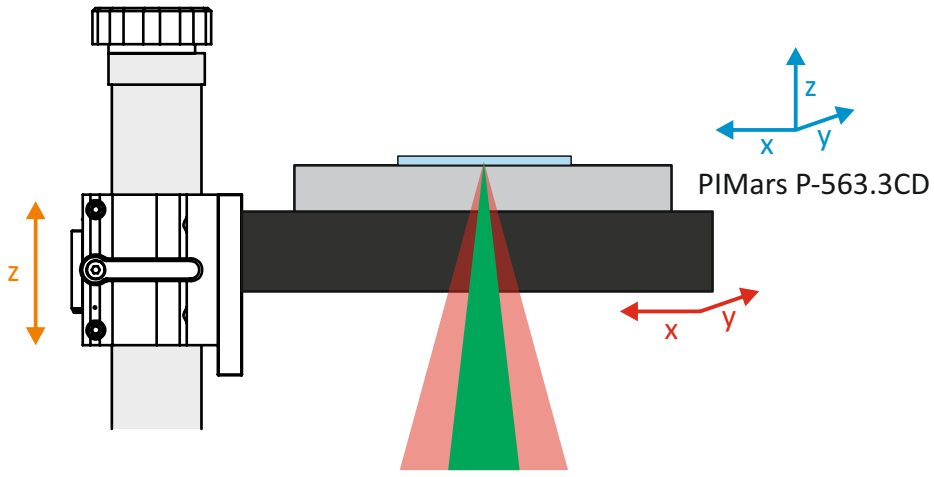

Figure 4.4: Schematic illustration of the sample positioning system. The Thorlabs VAP10 provides rough z-translation. The Lang MCL-2 stage provides are rough xy positioning, while the PIMars p-563.3CD enables high precision positioning. The two latter stages have a window that allows the excitation beam (red) to be focused on the sample and the emission (green) to captured.

However, the short working distances of the higher magnification objectives necessitates extraordinarily precise and stable sample positioning. After rough positioning a *Physical Instruments E-712.3CD* digital piezo-controller in combination with a *PIMars P-563.3CD* XYZ Nanopositioning Stage ensure sufficient precision for the investigation of nanoscalig samples. The translation of this stage is precise up to 0.5 nm, enabling imaging of even atomically thin materials at a range of 300 µm in all three spatial dimensions.

4.2.3 Excitation light sources

NKT SuperK Extreme

The different nanoscalig materials that are subject to investigation with this microscope show vastly different absorption behavior, which in turn require a lot of flexibility in the excitation light sources. For this reason the principle light-source is a *NKT SuperK EXTREME EXR-15* supercontinuum laser. The system is capable of emitting light within 410 nm to 2400 nm. The intensity at a given wavelength is shown in figure4.5. The device also supports pulsed emissions with a repetition rate of 78 MHz.

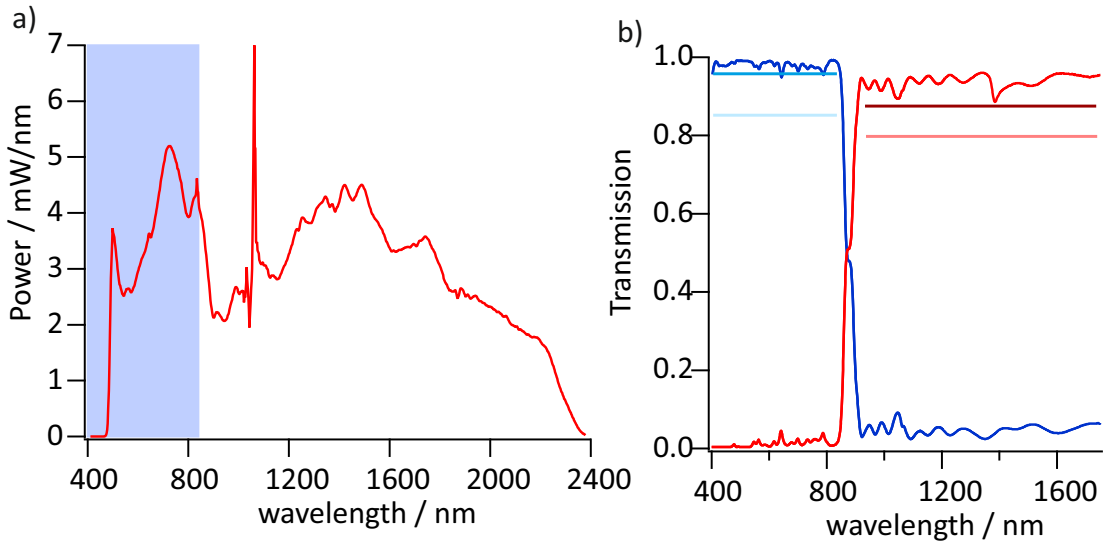

Figure 4.5: Emission profile of the SuperK Extreme white light source as provided by the manufacturer [190]. The blue area marks the spectral range of the SuperK Varia filter system. The peak at 1024 nm results from the emission of the pump laser.

Notably there is a sharp peak in the emission profile at 1024 nm. It results from a Nd:YAG laser, which pumps the optical fiber wich in turn produces the white light spectrum depicted in figure 4.5. Since the NIR emission was not required for any experiments and the fact that it can interfere with the detection system operating in this spectral range, the infrared range was removed from the emission via the SuperK SPLIT system. The fiber exiting the NKT SuperK EXTREME was directly plugged in the SPLIT box. The beam splitting optics inside this device separate the white light laser into its visible and infrared components, as depicted in graph 4.5 b). Another fiber connects

the SPLIT system to a NKT SuperK Varia tunable filter box, which selects a wavelength from the white-light laser to match the absorption energies of the probed samples. It can do so over the entire available spectral range and a bandpass ranging from 2 nm to 50 nm. Another fiber transitions from the VARIA into a free beam, which is then used by the microscopy setup. Directly after the transition into a free beam a shortpass filter (FES0850) removes the remainder of the pump laser at 1024 nm, which is not completely suppressed by the SPLIT system.
Since the spectrum of the NKT SuperK Extreme laser is not constant when changing the power setting, the power is always set to 80 %. To attenuate the excitation power as needed, a filter wheel (Thorlabs FW1AND) is positioned before the beam splitter with the following five neutral density filters: 0.5, 1.0, 2.0, 3.0, and 4.0.

405 nm laser diode

Furthermore a continuous wave 405 nm laser (LDM-405-350-C) with 350 mW laser can be used to supplement the NKT light source, in case the NKT laser cannot emit sufficient amounts of lights in the ultraviolet spectrum. However, this laser diode has a very inhomogeneous beam profile, which can be a problem when illuminating a larger area. As a result intensity distribution on the sample would be similiarly inhomogeneous. To improve the beam quality a spatial filtering setup is positioned directly after the diode. A schematic illustration of the setup is shown in figure 4.6.

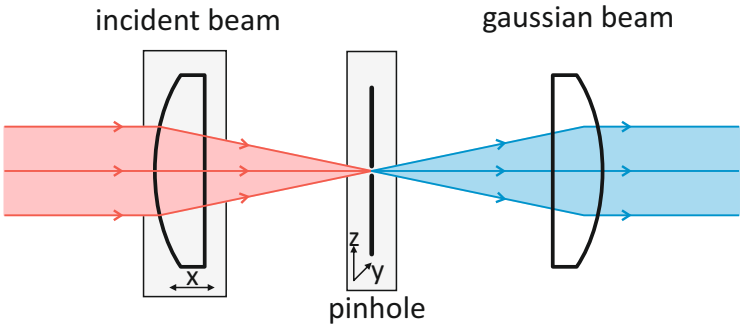

Figure 4.6: Schematic of the spatial filtering setup.

An aspherice lens (f = 6.24 mm) focuses the incident laser beam on a 10 µm pinhole in a xy-translation stage (*Thorlabs* ST1XY-D/M). Afterwards, filtered beam is then collimated using a plano-convex lens (*Thorlabs* N-BK7 f = 25.4 mm).
The spatial filtering setup produces a Gaussian beam by filtering out all beam components that do not contribute to a gaussian beam profile. Consequently, this method is costly if applied to a beam profile that diverges strongly from a Gaussian beam. In this case the 350 mW output power only amounts to 120 µW with a beamwidth of about 1 mm after filtering and optimal alignment. However, this value is still sufficient for probing individual low-dimensional objects.

4.2.4 Detection systems

Beam-splitting

The setup is equipped with three dichroic mirros. A 425 nm shortpass (DMSP805R), a 605 nm shortpass (DMSP605R) and a 805 nm shortpass. They are positioned within magnetic filter holders (DFM1/M) and can be swapped as needed for a particular material.

Time-correlated single photon counting

Time-resolved measurements can be performed using a Picoquant *HydraHarp* TCSCP module in combination with a Picoquant *PDM MPD* Single Photon Avalanche Diode, which provide time resolutions of < 50 ps. Combined with the pulsed NKT light source, TCSCP measurements are possible.

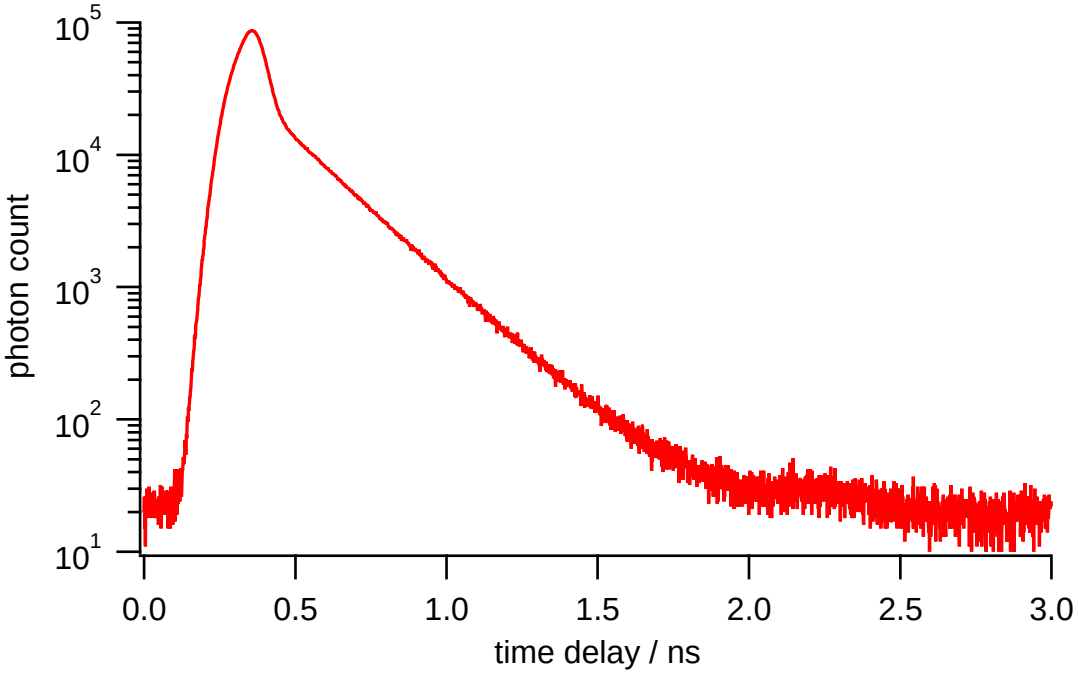

Figure 4.7: Instrument response function of the TCSPC detection system using the NKT SuperK Extreme laser.

The instrument response function of the system is shown in 4.7. It was recorded using scatter laser radiation from an aqueous suspension of polystyrene nanobeads. Given the length of the IRF, the setup has a lower resolution limit of 2.0 ns. The maximum repetition rate of the laser is 78 MHz, which provides an upper limit for the lifetime range of 12.8 ns. The repetition rate can be lowered to a minimum of 2 MHz, corresponding to an upper limit of 500 nm.

Imaging systems

Three imaging systems are available. The image is focused on the detector with a 200 mm lens. The Andor *Clara* silicon CCD camera with 1392x1040 6.45 µm pixel is particularly useful for low temperature measurements, since it can be cooled to −55 °C without condensation becoming an issue.
The QHYCCD QHY174mono SI CMOS camera provides higher resolutions with 1920x1080 5.85 µm pixel and higher quantum efficiencies as well as high framerates, due to USB3 connectivity, which enables higher data rates. As a downside, the non-vacuum construction makes strong cooling difficult since condensation on the chip becomes an issue.
For NIR measurements, a Xenics *Xeva* InGaAs camera with 320x256 30 µm pixel can be used for imaging materials that primarily emit in the NIR region. While SI can still be used for 1000 nm emission, anything beyond requires InGaAs detectors which the Xeva provides.

Spectral resolution

In order to fully characterize the samples detected by the imaging systems an Andor *Shamrock 303i* spectrograph is used. It offers an internal motorized grating turret, which has been mounted with three gratings with different central wavelength: 500 nm (300 lines), 1200 nm (300 lines) and 1250 nm (150 lines). Like the imaging systems this allows measurements from the UV to the NIR regions of the electromagnetic spectrum. The spetral lines are picked up by two detectors: An Andor *Newton CCD* with 1024x256 15 µm pixel for the VIS region and an Andor *DU491 IDus* InGaAs array with 1024 25 µm x 500 µm pixels for NIR measurements.

4.3 Sample preparation of low-dimensional materials

Preparing samples of low-dimensional materials is always a challenging prospect. The materials are by definition only a few nanometers strong in one or more dimensions, making individual objects very susceptible to damage. Combined with the sensitivity of their photophysical properties towards defects, sample preparation becomes a delicate matter. The following chapter explains the techniques used to produce the various samples for PL microscopy. Firstly the exfoliation of MoS_2 and h-BN is elaborated on. Both use fundamentally the same technique with some differences that will be mentioned below. Secondly, the sample preparation of individual nanotubes from suspensions is briefly explained. The two approaches can then be combined for the production of hybrid structures.

4.3.1 Preparation of MoS_2 and h-BN samples

Both HBN and MoS_2 are both prepared using exfoliation from larger crystals and transferring them unto #0 glass slides. As a substrate Menzel #0 microscopy slides (thickness 85 µm-115 µm) were used. Since these are very fragile and the fact that the exfoliation process is susceptible to vibrations and deformation of the substrate, the slides were taped on top of significantly stronger 1 mm microscope slides (VWR 631-1550) using Scotch©3M Magic Tape. The glass slide was first cleaned using isopropanol and then plasma-treated in a Zepto-BLS Model 2 plasma system to remove impurities. The Plasma was set to maximum power with an oxygen-flow setting of 0.4 for 10 min. The synthetic MoS_2-crystal was purchased from 2D semiconductors, while the h-BN crystal (BN2A1) was obtained from HQ Graphene.

4.3.1.1 h-BN sample preparation

In the case of h-BN, NITO-Tape was used to pick up a multitude of layers directly from the crystal. The material was thinned by spreading it across the entire tape by folding the tape unto itself. The tape was then applied to the glass slide. Doing so slowly and using a Q-Tip to press it onto the substrate carefully minimizes the formation of air bubbles. The glass slide was then heated to 110 °C for 10 min. In order to ensure swift and homogeneous heating, a metal block is coated with thermal foil. The temperature was controlled using an infrared non-contact thermometer. Afterwards, the tape was pulled off at an angle of roughly 30° and a speed of about 10 cm s^{-1}. An illustration of this process is shown in Figure 4.8. Once the transfer of the material unto the coverslip is complete, it is removed by cutting the scotch tape, which holds it on the microscopy slide. That way, the coverslip can be recovered without risk of damaging it when peeling off the tape by hand.

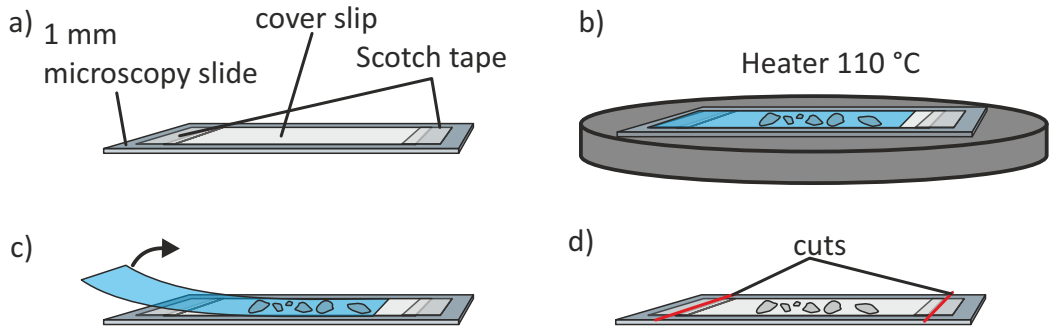

Figure 4.8: Ilustration of the preparation of h-BN samples. a) A cover slip is fixated to a microscopy slide using scotch tape b) The NITO-tape holding bHN flakes is applied and the slide is heated for 10 min at 110 °C. c) The NITO tape is pulled of, leaving hBN-flakes behind. d) The scotch tape holding the coverslip on the microscopy slides is sliced as indicated by the red lines. The coverslip can then be used for fluorescence microscopy experiments.

This approach to sample preparation generally results in a plethora of h-BN oligo and multilayers, with few monolayers sprayed in between. Reflectance microscopy can be used to distinguish between the different layers. This approach can also be used to prepare MoS_2 layers. In case isolated monolayers are needed, individual monolayers can be picked up and selectively transferred to a different substrate. This can be advantageous for PL microscopy experiments since signals from other flakes can interfere with the measurement of a flake.

4.3.1.2 MoS_2-sample preparation

The MoS_2 monolayers were prepared by Simon Kießling using a method described in Castellanos-Gomez et al. [191]. The first sample preparation step is identical to h-BN described above in section 4.3.1.1. After that, a single monolayer on the sample was identified using reflectance microscopy. This monolayer was picked up with a PDMS-Gel Film from Gelpak and then placed on a new cleaned and plasma-treated coverslip. The monolayer can be deterministically transferred to the new substrate by carefully pulling the film while heating the coverslip.

4.3.2 Preparation of SWNT samples

The major challenge for SWNT samples is distributing individual nanotubes across the sample geometry. Spin coating and drop-casting either waste much of the material or tend to accumulate material due to the coffee-stain effect. However, using a slightly modified approach, it is possible to distribute SWNTs evenly across the sample's surface. For SWNTs, it is imperative to use glass slides with low fluorescence intensity in the NIR region to avoid an overlap with SWNT signals. Cover-slip from Menzel have proved to be th best commercially available option[157]. Four droplets of silica grease are deposited in a square pattern on the glass slide. A drop of SWNT suspension of 15 µL is cast between the silica grease. Another glass slice is carefully pressed on top of the sample to spread the suspension between the two slides. This process is illustrated in figure 4.9.

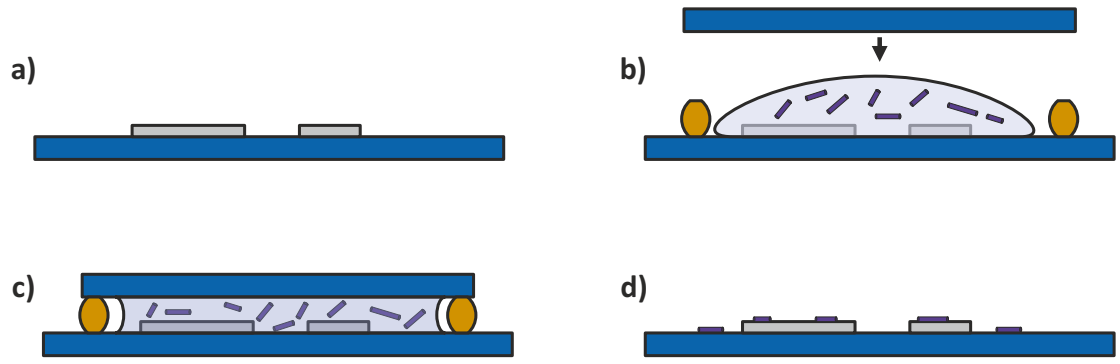

Figure 4.9: Illustration of the 2D/SWNT hybrid sample preparation. a) Basis are 2D layers on coverslips as prepared in 4.3.1 b) A droplet of SWNT suspension is cast on the 2D layers. Silica grease (orange) serves as spacer between the two cover slips. c) This "sandwichstrucure is placed under vacuum for 45 min. d) The result are a more homogeneous distribution of SWNT across the sample compared to pure drop-casting.

For the deposition of SWNTs on 2D semiconductors, exfoliated 2D layers are put on the glass wafer as described in 4.3.1.1 and 4.3.1.2 with no further alterations to the preparation method compared to blank samples.

4.4 Results and Discussion

4.4.1 PL microscopy of low-D materials

The main purpose of this PLE microscopy device is the observation of low-dimensional materials. The microscope has been tested on a number of systems to ensure its proper functionality.

4.4.1.1 Quantum dots

PL Imaging of quantum dots can test the PL-Setups resolution capabilities. As elaborated in section 2.3.2 the resolution of a microscope is fundamentally limited by the refraction limit. However, this holds only true if other technical limitations do not impose a limitation on the resolution exceeding the Abbe limit. One way of ensuring this is to take an image of a point-light source. Doing so should produce characteristic refraction patterns, described by the airy-disc function (see 2.3.2). One of the closest physical system to a point light source are quantum dots, quasi one dimensional

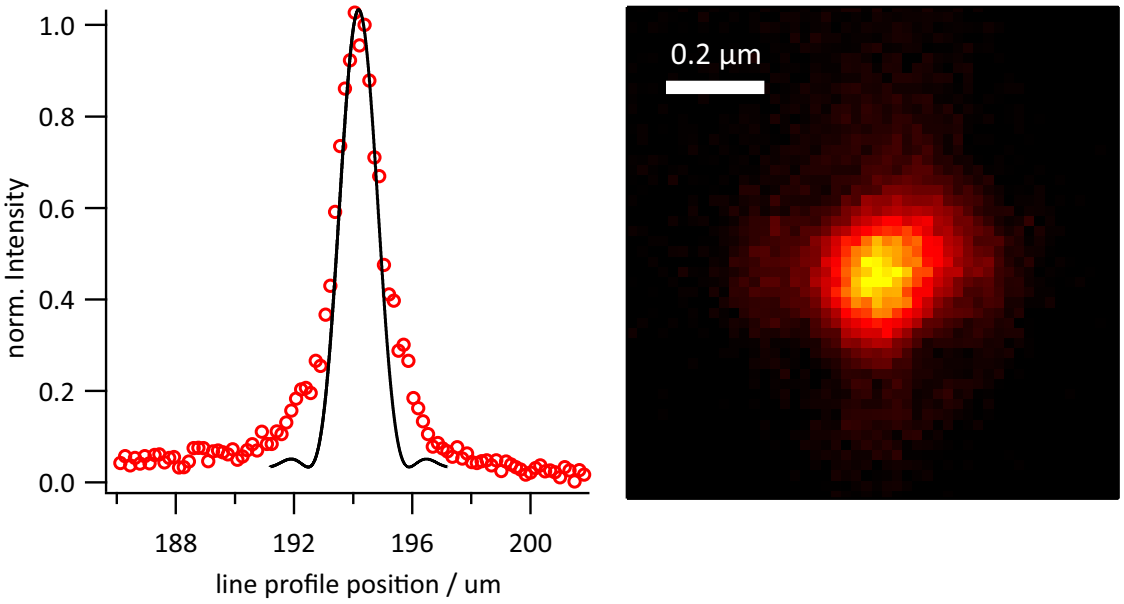

Figure 4.10: The right image shows the PL image of a quantum dot. The left image shows the line profile through the middle of the dot (red marker) and a point spread function at the same wavelength and numerical aperture

Overlaying the Point-Spread function over the Quantum Dot signal shows that the expected Refraction pattern is present, proving that the imaging capabilities are indeed limited by refraction. However, the signal does not match the results perfectly, with the actual signal showing a greater intensity. The point-spread function assumes a perfectly spherical aperture. The image shows a faint cross shape as a diffraction pattern, which is characteristic for rectangular apertures[192]. The most likely explanation for the discrepancy between line profile and the point-spread function is that the various optical elements (mirrors, lenses, filters) act as a non-spherical "aperture", causing this deviation.

4.4.1.2 Single-walled carbon nanotubes

4.4.1.3 Molybdenum-disulfide

One of the critical challenges in PL microscopy regarding TMDCs is distinguishing between bulk material, oligolayers and monolayers. The PL microscope has been successfully used to image MoS_2 flakes of various thicknesses and positively identify single monolayers via PL spectroscopy.

Samples are prepared using reflectance microscopy to guide the exfoliation process. After identifying promising flakes via reflectance microscopy, transmission imaging can quickly identify a flake. PL imaging is usually less suitable for this task since it requires considerably longer integration times of about a factor of 10. This makes transmission microscopy more practical for scanning larger sections of a sample. Once a flake is identified, a PL image is recorded while allowing a more precise analysis. An image of a bulk sample as well an oligolayer section is depicted in figure 4.11.

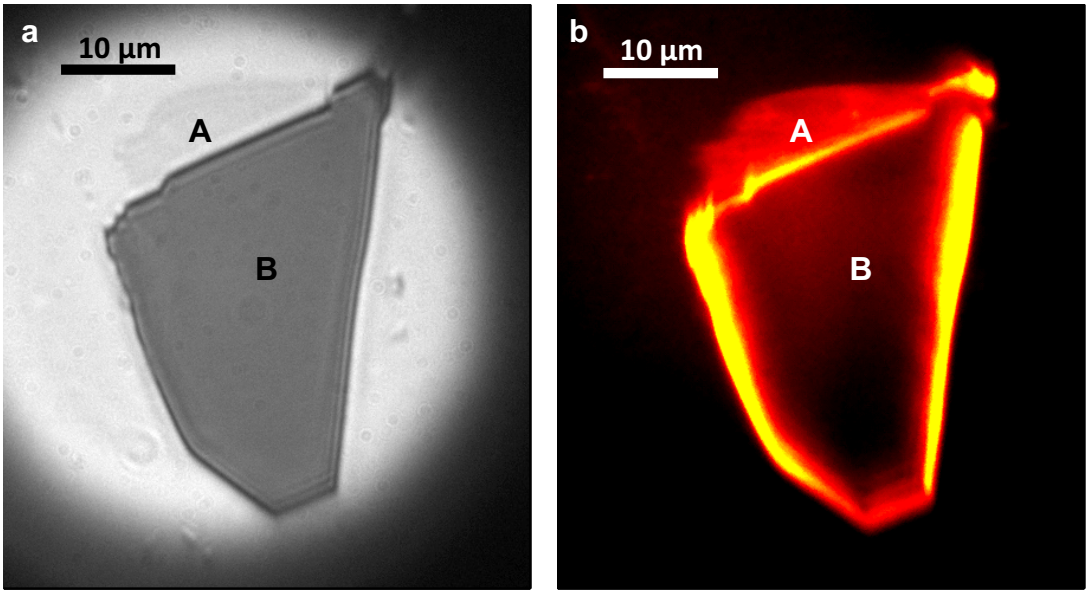

Figure 4.11: Transmission (a) and photoluminescence image of a MoS_2 multilayer flake. A marks an oligolayer, while B marks bulk MoS_2 material.

A marks an oligolayer, which easily be recognized by its transparency in the transmission image. B marks the bulk which shows stronger fluorescence at its edges, which is characteristic property of multilayer flakes. The increased PL intensity at the edges of a flake have been attributed to numereous factors like charge carrier density, defect density, strain, screening, band-bending and crystallinity [193–196].
Less clear is the distinction between oligolayer and monolayer as both are transperent in transmission spectroscopy. The oligolayer A does appears somewhat inhomogeneous which gives some early indication, that the sample is indeed not a monolayer. An image of an actual monolayer is seen in figure 4.12

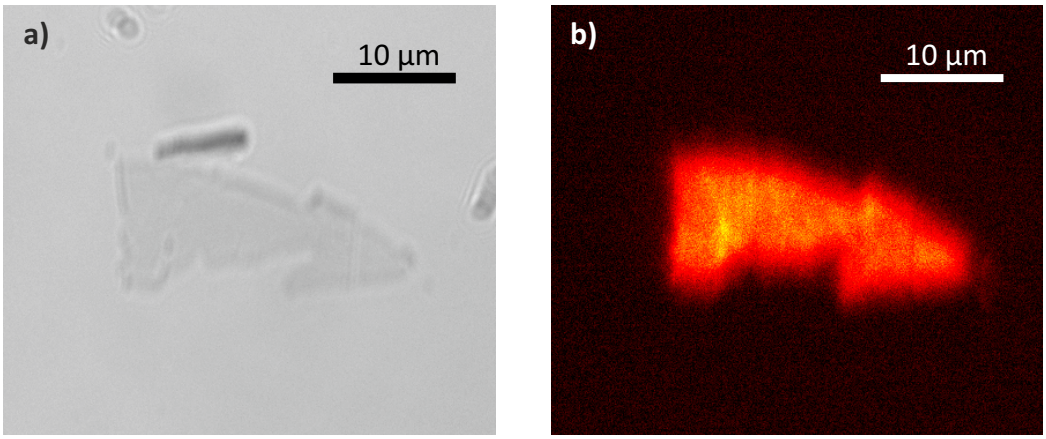

Figure 4.12: a) Transmission Image of an MoS_2-monolayer b) Photoluminescence Image of the same MoS_2-monolayer. The various objects in the transmission image, which do not have corresponding PL signal are impurities.

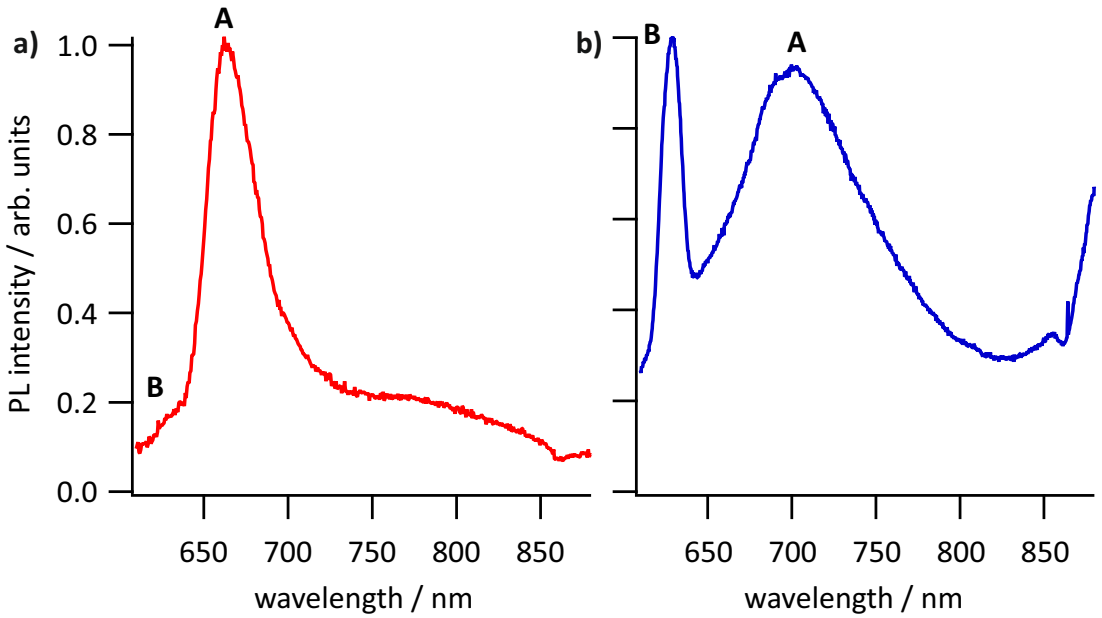

Figure 4.13: a) PL spectrum of the MoS_2 flake shown in figuere 4.12. A and B mark the two relevant excitonic transitions. b) PL emission of a multilayer MoS_2 flake.

However, at times, the contrast in the transmission image is not clear enough to identify a monolayer with a satisfying degree of certainty. PL spectroscopy is necessary to identify a monolayer

in this instance. This experimental setup can selectively target a region limited by the size of the laser spot. Figure 4.13 shows the PL spectrum of a monolayer flake and of a bulk sample. The PL of the bulk sample mainly comes from emission at the band-edges, as seen in figure 4.11. This is why direct bandgap excitonic transitions are detectable despite being a characteristic feature of MoS_2 samples. However, the excitons' relative strength and peak positions are strongly shifted, which serves as a clear indicator to differentiate oligolayer and monolayer samples.

4.4.2 PL microscopy on hybrid systems

4.4.2.1 H-BN/SWNT samples

Depositing SWNTs on HBN layers and taking fluorescence images can be used to verify the viability of a given sample preparation technique. Since h-BN does not strongly interact with the SWNTs, we can observe how SWNTs aggregate when deposited on mono-layer materials. Figure 4.14 shows an image of SWNTs deposited on h-BN. SWNTs can be observed both on and beside the flake proving that the deposition method works as intended. However, one unintended side effect is that SWNT material appears to aggregate at the edges of the 2D-flake. While this does not pose a significant problem for measurements of tubes on the flake, it necessitates the preparation of flakes with about 30 µm. Otherwise, the comparatively strong signal emitted from aggregated tubes can not be sufficiently separated from the tubes on the flake itself.

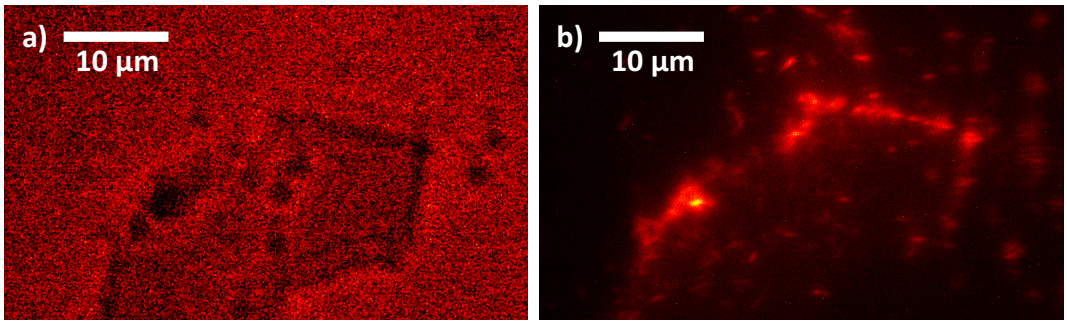

Figure 4.14: a) Transmission Image of an HBN flake before the introduction of SWNT into the sample. b) Photoluminescence image of the same flake but with SWNTs on top. Aggregation at the edges of the flake are visible.

Otherwise the method, described in section 4.3.2 appears to perform adequately, both for isolated SWNT samples and depositing on monolayer. No meaningful changes in the SWNT signal could be detected. However that is not necessarily surprising given the fact that due to the large difference in bandgaps no significant interaction between SWNTs and h-BN is to expected.

4.4.2.2 SWNT/MoS_2 hybrid samples

Using the same preparation technique that was used for h-BN samples, SWNTs can also be deposited on MoS_2 monolayer flakes. The flakes were identified via reflection microscopy, in which they appear significantly thinner than oligo-layers. Afterwards, PL imaging and spectra of the flake were used as verification. One such sample before SWNT deposition is shown in figure 4.15.

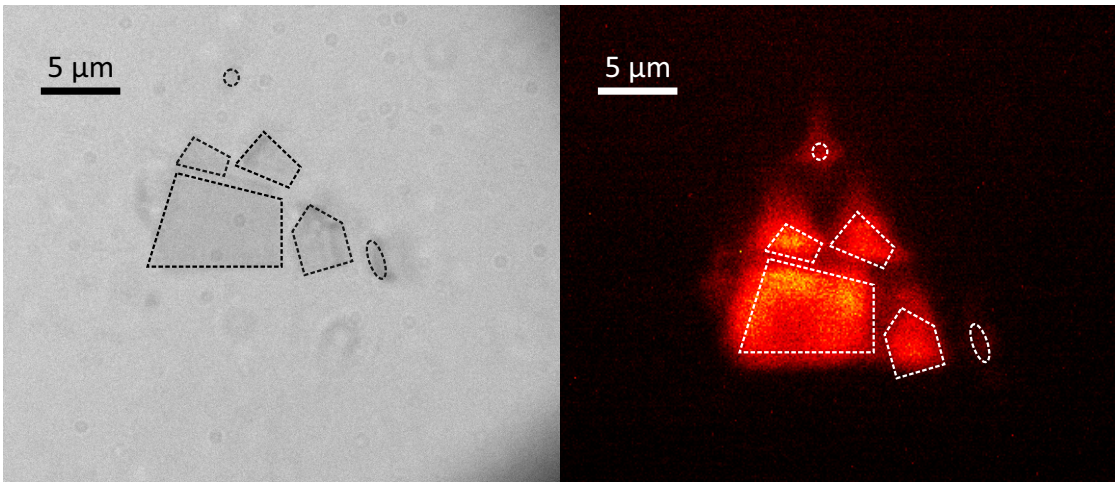

Figure 4.15: a) Reflectance image of the sample before SWNT deposition. b) Fluorescence image of the sample before SWNT deposition. The outlines between the two images match.

After deposition, using the procedure described in section 4.3.2, PL imaging was resumed. Somewhat surprisingly, however, no SWNTs could be detected in the immediate vicinity of the MoS_2 sample. Although several SWNT are present beside the flake, none were found on the MoS_2 material itself (see figure 4.16). As explained in section 4.4.2.1 we would expect to find substantial aggregation at the flake edges. However, in this case, despite SWNTs being nearby, we observe no aggregation at the edges or the top of the MoS_2 flake. There are two possible explanations for this observation: Firstly: No SWNT have been deposited on the MoS_2 flake, or secondly, the SWNT has been deposited but no longer show a detectable fluorescence signal.

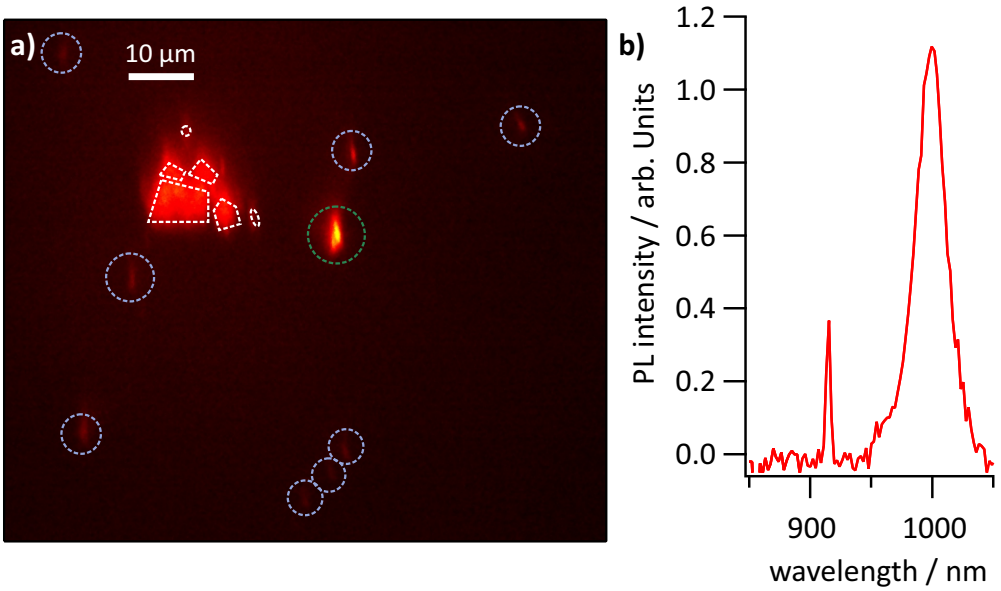

Figure 4.16: a) Photoluminescence image with an 950 nm longpass filter of the MoS_2 flake after SWNT deposition. The NIR emission of the MoS_2 flake (white outline) is visible by the filter but numerous SWNTs (green and blue circles) are present in the vicinity of the flake. b) PL signal of the SWNT with the green outline in a). It shows the characteristic SWNT excitonic emission at 1000 nm

Investigating the signal of MoS_2 flake itself reveals a substantial change in its emission spectrum. Scanning over the entire sample shows the same change in spectral behaviour across the entire sample. A comparison in emission spectra before and after introducing SWNTs is shown in figure 4.17. The observed changes in the PL intensity are consistent with a shift from excitonic transitions to trionic signals. Mouri et al. [64] reported the reverse of this process when treating MoS_2 flakes with F4TNQ, an oxidizing agent. This indicates that treating the flake with SWNT suspensions increases the negative charge density on the flake.

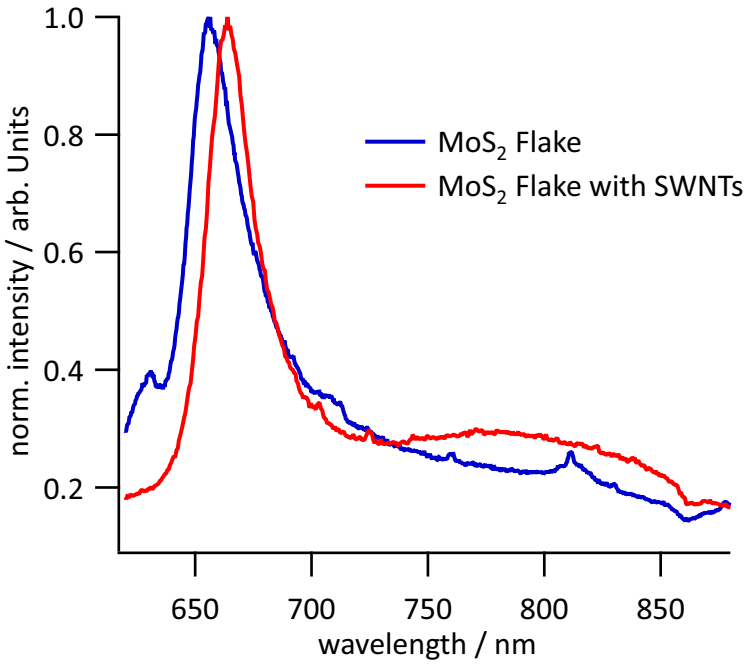

Figure 4.17: Comparison of the photoluminescence spectra of MoS_2 flakes before and after treatment with swnt-suspensions.

Another possible explanation is that changes in the dielectric environment induce this change in behaviour. Together with SWNTS, both PFO-BPy and toluene were deposited on the MoS_2-flake, which in turn might sufficiently alter the dielectric environment without SWNTs having any measurable effect. Furthermore, while toluene and PFO-BPy are both not particularly reactive substances, it is also possible that electrons are transferred from these compounds unto MoS_2. To investigate the impact of PFO-BPy and toluene on the behaviour of two-dimensional MoS_2, a reference experiment with an identical experimental procedure with a PFO-BPy/toluene solution has been conducted. A 0.1 mg L^{-1} PFO-BPy solution has been drop cast on a freshly prepared MoS_2 flake and dried in a vacuum. The exact concentration of PFO-BPy in the SWNT-suspension is not precisely known since an unknown portion of the polymer is lost during centrifugation. Since the original suspension is prepared by shear-mixing with PFO-BPy concentration of 0.5 mg L^{-1} and since the resulting suspension has been diluted by a factor of 1000 to obtain the drop-casting suspension, the concentration in this reference experiment should be at least 500 times more concentrated. If any changes in MoS_2 are due to PFO-BPy, they should be even more pronounced than in the SWNT experiment. The resulting images and spectra are shown in figure 4.18.

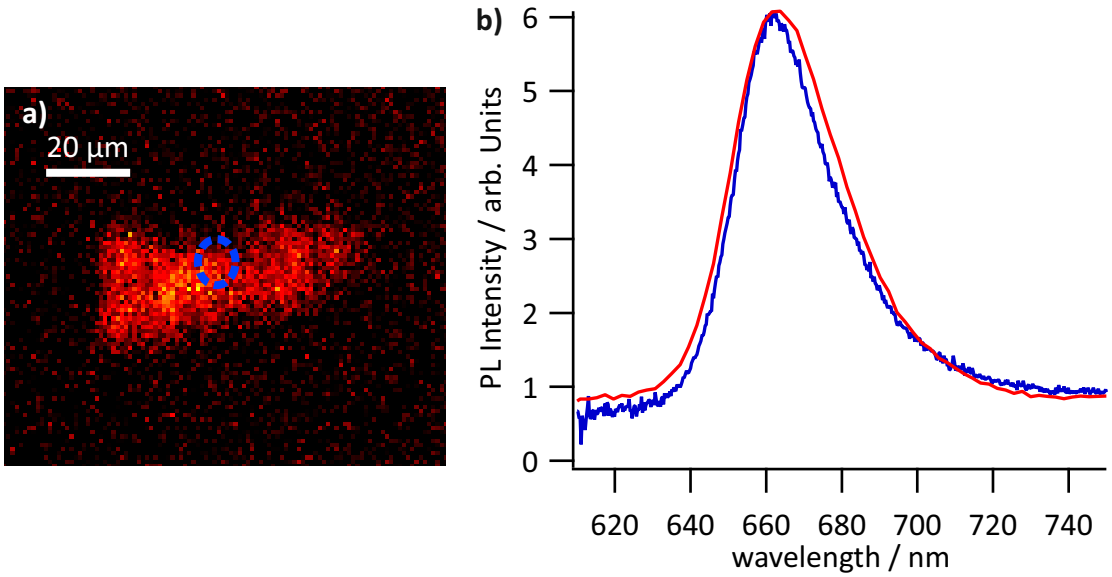

Figure 4.18: a) PL image of an MoS_2 flake after coating the flake with PFO-BPy. The blue circle indicates the excitation laser spot for capturing the reference spectrum. b) shows this spectrum in blue. The red line is the PL spectrum of the flake before PFO-BPy coating. Photoluminescence spectrum of a MoS_2 flake before and after treatment with a PFO-BPy/toluene solution.

Comparing the two spectra before and after treatment, a redshift of about 1 nm in exciton/trion peak can be observed, alongside a small line broadening. The redshift is most likely caused by an increase in dielectric screening due to polymer deposition on the flake. This reduces the exciton binding energy and thus transition energy [197, 198] Inhomogeneous line broadening can occur with an increase in disorder in the environment. It should also be noted that the probed spot is not precisely identical since the sample had to be put under vacuum and then re-positioned on the microscope to precisely match the MoS_2/SWNT experimental procedure. A perfect match in the target laser spot is not possible, so the minor changes in the optical spectrum may be due to the inhomogeneity of the sample or the substrate surface. More significant than the minor shifts in the PL signal is the strong contrast with the observations made after treatment with SWNT

suspension. The peak shift is not nearly as strong, and the line width increases instead of decreasing, indicating that the relative trion/exciton emission intensity does not meaningfully change. This effectively eliminates toluene and PFO-BPy as causes for the observed changes, barring a slight inhomogeneous broadening. Consequently, SWNT as the only remaining component in the suspension is very likely the cause for the changes in the MoS_2-photoluminescence.

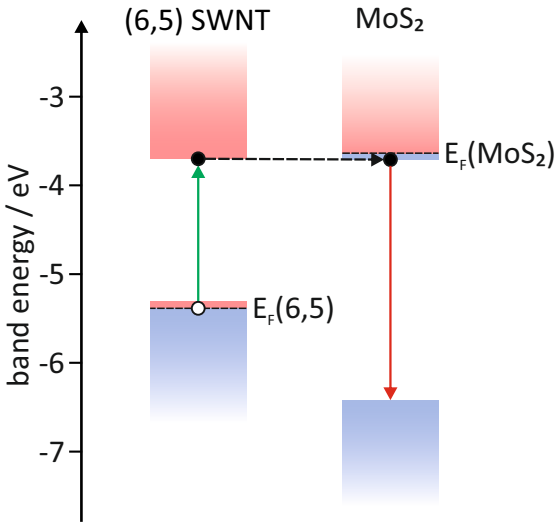

Figure 4.19: Band energies of (6,5) SWNTs and MoS_2. The (6,5) band energies are obtained from spektroelektrochemical analysis [199] while the MoS_2-values are based on theoretical calculations [175]. The blue areas indicate occupied states, while red areas mark empty states. MoS_2, as prepared, is often somewhat n-doped, which means some of its conduction band states are occupied. These states could transfer electrons into the conduction band or the valence band of the SWNT, since SWNTs, as prepared, often exhibit a slight p-doping and consequently a slightly depleted conduction band. The depicted doping level only serves as an illustration for possible transitions and is not based on quantified measurements.

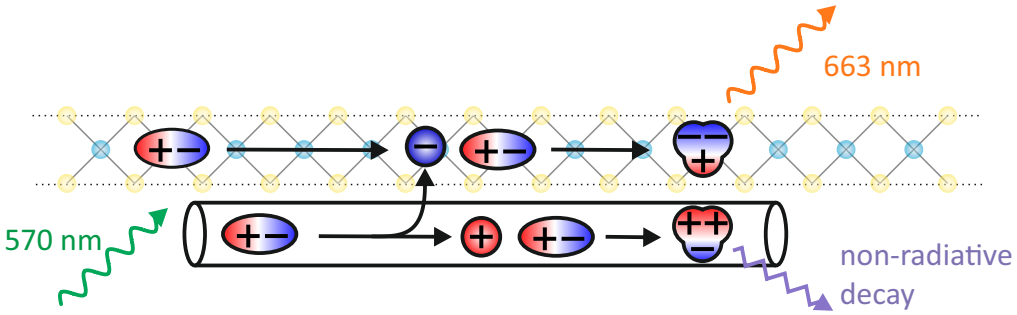

Figure 4.20: Schematic illustration of the proposed charge-transfer mechanism. 570 nm excitation light generates excitons in both the MoS_2 layer and the carbon nanotube. Excitons sepearte and transfer a negative charge to the MoS_2 layer. It combines with a trion and emits its characteristic emission at 663 nm. The hole on the tube recombines to a positive trion and decay non-radiatively.

Given the fact that the PL spectrum indicates that excess charges were added to the MoS_2 flake, it seems reasonable to assume that those charges originate from the nanotubes. Charge transfer between the two materials requires a band alignment that doesn't pose prohibitively tall potential barriers between the conduction or valence bands. The bands and possible charge transfers

are shown in figure 4.19. However, the energy bands depicted in the image are not perfect for the bands under the presented experimental conditions. The bands of (6,5) were experimentally obtained by spectro-electrochemical analysis [199] in percolated network films, submerged in a THF solution. Since the environment can shift the band energies, tubes deposited on a glass wafer will have a slightly different band structure. The same holds true for MoS_2, whose bands were obtained by theoretical calculation via a G_0W_0 approach [175]. Given the larger surface area and the stark difference between vacuum and a glas/air environment, the potential deviations are probably even more significant. Nonetheless, the documented values make an electron transfer between the materials at the very least plausible. Furthermore, both compounds are often not in their intrinsic state after sample preparation. SWNTs usually exhibit slight p-doping, especially when exposed to air. MoS_2 on the other hand, is often somewhat n-doped. Therefore even if an interaction would be impossible from the intrinsic state, a charge transfer might occur via otherwise impossible transitions from doped bands. Furthermore, bandgap renormalization could further shift the band energies. Given how close the conduction bands of the two materials are, their precise relative position can not be predicted.
However, despite these caveats, the bands are energetically close enough together that some charge transfer processes seem considerably more plausible than others. One possible explanation would be the transfer of electrons from the (6,5) SWNT unto the MoS_2 monolayer in an electrochemical reaction. Doping SWNTs introduces defect sites that, upon contact with excitons, can cause non-radiative decay. This usually results in a drastic reduction in PLQY, which would make the SWNTs extremely difficult to detect via fluorescence microscopy. However, the relative band position between the two materials would make this reaction quite improbable. Transfer of charge carrier from the valence band of the SWNT to the conduction band of MoS_2 would face a steep potential barrier, making this mechanism virtually impossible. The intrinsic doping in the SWNT and MoS_2 would further exacerbate this issue.
Another more plausible mechanism is that photo-generated excitons in the MoS_2 flake are separated with positive charges being transferred on the tube and the remaining negative charges forming a trion on the MoS_2 flake (illustrated in figure 4.20). Under these conditions, observing SWNT emission would also be very difficult since the broad absorption spectrum of MoS_2 makes it impossible to excite SWNT excitons at or below 570 nm without doing the same in MoS_2. It has been reported in the literature that 2D heterostructures have produced interlayer excitons under those circumstances [176]. Drastic quenching of intra-layer photo-luminescence has also been observed [172, 180–188, 200]. However, direct observation of interlayer excitons was only possible below 20 K in 2D heterostructures. Given that the experiments presented in this thesis have all been performed at room temperature, the absence of this signal does not necessarily preclude the possibility of a charge transfer. The PL signal does not significantly change when scanning over the entire flake, suggesting that most of the flake contacts SWNTs.

Beyond the experiments presented in this dissertation, additional methods could provide more insights and verify the presented hypothesis. In order to gain more information about this system, two experimental pathways seem particularly promising: Firstly, low-temperature PL microscopy on two-dimensional heterostructures report the observation of inter-layer excitons [170]. This becomes evident with a new signal in the PL spectrum at the contact area, which is completely absent in our experimental evidence. If charge transfer between SWNTs and Mo_2 is possible as hypothesized, then interlayer excitons should form. However, the Coulomb interaction is likely not strong enough to stabilize them at room temperature. If so, PL spectra at 10 K

could provide direct evidence for their existence and for charge transfer between the materials.

A second promising approach to gain more information would be Raman imaging. As further elaborated in section 2.4.2 doped SWNTs show significant changes in their Raman signal. Even if PL imaging and spectroscopy seizes to be viable, the tubes on MoS_2 could be investigated via Raman spectroscopy. It would allow for identification and determining the doping level of any SWNT, which could provide more definitive information regarding the SWNT/MoS_2 interaction and direct evidence of SWNT/MoS_2 contact areas.

4.5 Summary

This chapter focused on PL microscopy of nanoscalig materials. A PL microscope was constructed, and its capability to examine nanoscalig materials has been verified by recording PL images and spectra of SWNTs, MoS_2 and quantum dots. The setup also allows for reflectance imaging, making it possible to quickly identify potential monolayers of MoS_2 and h-BN in a given sample. The setup operates at the resolution limit as verified by the refraction patterns observed during quantum dot imaging.
A method to produce SWNT/TMDC heterostructures materials has been tested by depositing SWNTs on h-BN monolayers. PL imaging shows that SWNTs are deposited on a single flake but tend to aggregate at the edges of the monolayer.
Using this method to bring SWNTs in contact with MoS_2 monolayers significantly impacts the PL spectrum of the MoS_2 flake, despite no measurable SWNT signal on or directly nearby the MoS_2 flake. MoS_2 PL intensity is shifted away from excitonic signals towards trionic emission. This shift is not detectable in a reference experiment using only a solution of toluene and PFO-BPy. Trionic signals in low-dimensional materials are usually associated with doping. The relative band positions of SWNTs and MoS_2 make an electrochemical reaction that transfers electron from SWNTs to the MoS_2 unlikely. A fast electron transfer from SWNTs to MoS_2 is a plausible explanation for the formation of trions in the monolayer, although this could not be directly proven in this dissertation.

5 Charges and charge propagation in SWNTs

One of the more promising potential applications of SWNT is that as a semiconductor material. Today, silicon is the foremost material for almost every semiconductor application, notably in computation. However, due to the immense miniaturization efforts in the past decades, fundamental quantum-mechanical limitations are fast approaching [201]. Low-dimensional materials like SWNTs could provide a pathway to continue improving semiconductor applications beyond this point. In order to make low-dimensional semiconductors viable for application, it is necessary to modify their electronic properties by doping the semiconductor, thereby introducing additional charge carriers and altering their band structures. In bulk semiconductors, doping means substituting atoms in the crystal lattice with other elements. In SWNTs, on the other hand, doping is considerably less well understood. Their one-dimensional structure and reliance on redox-doping instead of substitutional methods result in vastly different behaviour than bulk semiconductors. Many of the established doping and preparation techniques are also not applicable to SWNTs, necessitating a different approach to doping.
Furthermore, challenges in sample and dopant preparation have often limited investigations in this direction. Absorption spectroscopy has provided considerable insight into the electronic changes that occur during the doping process but relying on optical spectroscopy to characterize charge behaviour in SWNTs is still a somewhat limiting approach. In the following chapter, a series of experiments are presented, using established sample preparation techniques to enable more in-depth characterization of charge-carrier behaviour in doped SWNTs.
Firstly, the changes in the conductivity of SWNT-thin films is investigated. The mechanical fragility and sensitivity of SWNTs films to their environment make it challenging to probe the conductivity while controlling the doping level. The following chapter will present the preparation of a viable thin-film sample on interdigitated electrodes and their characterization via absorption spectroscopy and resistance measurements.
As mentioned before, it is not yet established in scientific literature whether or under which conditions charge carriers are localized or homogeneously distributed in SWNTs. To further investigate this question, the results of a series of electron paramagnetic spin resonance (EPR) spectra on doped SWNTs will be presented. This technique allows quantitative measurements of charges on the nanotubes. The resulting values were compared to previously established techniques to quantify charges via absorption spectroscopy.
Next, the results of Raman spectroscopy of doped SWNTs are presented. Raman spectroscopy holds a few advantages of absorption spectroscopy since it can be used to investigate film surfaces or another sample under which the absorbance can be challenging to measure. Correlating the results could provide the basis for a more straightforward way to characterize SWNT samples.

Lastly, the results of a cooperation with Jašinskas et al. [202] regarding the dynamics of photo-generated charge carrier of SWNTs and SWNT/PCBM blend films will be elaborated on. Just like the charge carriers themselves, charge carrier propagation is vastly different in percolated nanotube networks compared to bulk semiconductors due to the prevalence of charge hopping between tubes. The transient photocurrent measurements provide considerable insight into this aspect of charge propagation.

5.1 Resitivity measurments of doped SWNT-films

Conductivity measurements of SWNT-films, while simple in principle have a few design challenges that need to be overcome. Earlier versions of this experiment used four-point-measurements as a means to measure conductivity while correcting for contact resistance. This approach proved problematic however. Contacting with electrodes can damage the film. Combined with repeatedly submerging in solvent, followed by drying the films suffered considerable damage, rendering any measurement result meaningless. Consequently the measurements were performed on transparent Indium-tin-oxide interdigitated electrodes. With this approach absorption spectra of doped SWNT thin-films can be recorded alongside the resistance measurements.

5.1.1 Experimental aspects

5.1.1.1 SWNT sample preparation

The most straightforward way to characterize the resistivity of a thin film is four-point sensing. In previous iterations of this experiment, this approach has unfortunately proven to be too destructive for SWNT thin films. Contacting the film from above with electrodes can cause sub-millimetre size rips. The doping process requires submerging the films in toluene which swells up the film and exacerbates existing cracks. While individual measurements are not problematic, the damage accumulates over the entire series of doping steps to a point where the measured resistance values become meaningless. Therefore a different approach was chosen: measuring the resistance of thin film deposited on indium-tin-oxide (ITO) interdigitated electrodes (IDE; IME 2025.3 M ITO U). A schematic illustration of the sample design can be seen in figure 5.1.

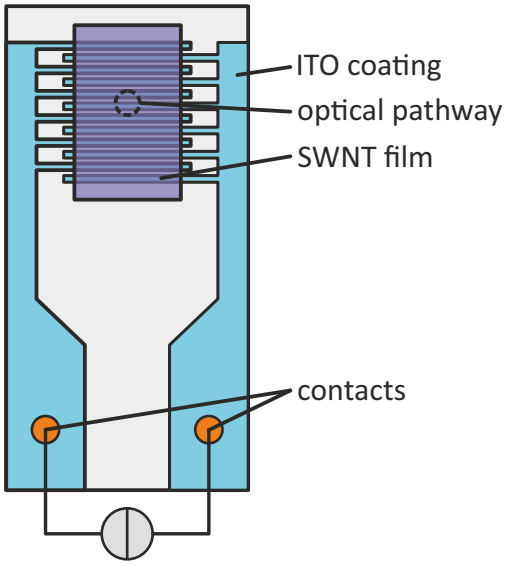

Figure 5.1: Interdigatated electrode sample for conductivity measurements. According to supplier information the distance between individual ITO strips is 20 µm at a length of 5 mm. The glass substrate is coated with a layer of conductive but transparent ITO. The dashed circle, labeled ”optical pathway” indicates the area that is probed via a 1 mm plate with pinhole. The blank ITO electrode is used a background measurement.

The production of SWNT thin films via filtration is explained in detail in section 5.2.1. 1 mL of a (6,5)-PFO-BPy suspension with an optical density of 2.5 at 1000 nm is filtered to produce the thin film. Instead of redispersing the film, the filter carrying the SWNT material is cut to size to fit the IDE. It is then firmly pressed on the ITO slide for about 1 min. A sequence of three acetone baths dissolves the filter material. After dissolving the filter, an SWNT thin-film remains on the IDE. The film had a thickness of 58 nm, determined by the optical density [203]. The optical pathway (see figure 5.1 is probed with the Agilent Cary5000 spectrometer, with a 1 mm pinhole plate to ensure that only the surface area that is covered by SWNT-film is probed.

5.1.1.2 Benzylviologen preparation

Viologen compounds have been reported to successfully n-dope SWNT [204]. However, in our experiments, viologens have not produced stable n-type doping of (6,5) SWNT films under ambient conditions. While the redox compounds themselves are stable, the doping itself seems to quickly degrade upon contact with oxygen. However, it can be used to remove existing p-doping in SWNTs films, which is its main function in this dissertation.

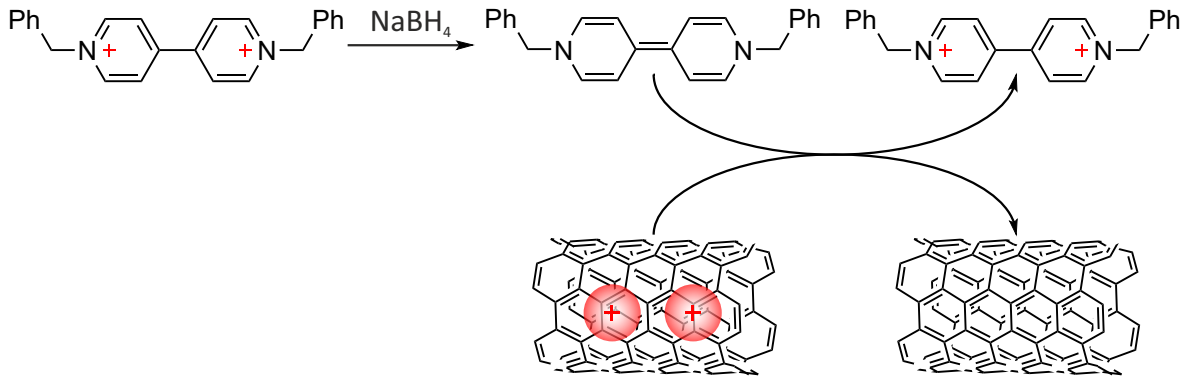

Figure 5.2: Reaction scheme of Benzylviologen and SWNT. 1,1´-Dibenzyl-4-,4´-bipyridinium dichloride is reduced via $NaBH_4$ to the reduction agent Dibenzyl viologen. This compound in turn is used to remove p-doping from the SWNT-film.

Benzene-viologen (BV) was prepared via a two-phase synthesis as described by Kim et al. [204]. 2 mL of water and a stir bar were given into a Schlenk flask, and 1 mg of 1,1´-Dibenzyl-4,4´-bipyridinium dichloride (BV^{2+}) were added and dissolved. Then 2 mL of toluene were added. Since the two solvents are not soluble in each other and toluene has a lower density, two phases form with toluene on top. Then 2 mg sodium bor hydride ($NaBH_4$) was added. During the reaction, gaseous diborane is formed and emitted from the solution. A schematic illustration of the reaction is depicted in figure 5.3.

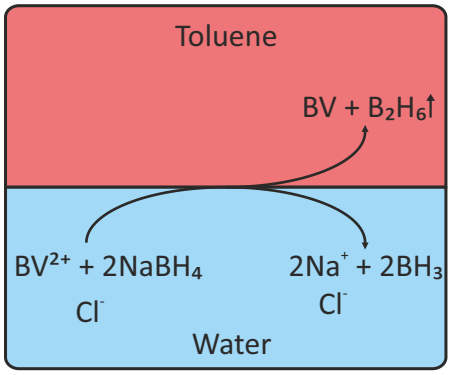

Figure 5.3: Schematic illustration of the two-phases synthesis process. BV^{2+} reats with sodium bor hydride to Natrium and BV. BV is only soluble in the toluene phase due to its greatly reduced polarity compared to BV^{2+}, and thus migrates in the organic phase. Diboran (B_2H_6) is formed as a byproduct and is emitted into the ambient air.

BV is stable in ambient condition for extended periods of time Kim et al. [204], so it can be used for longer measurements series.

5.1.1.3 Doping of SWNT films

As a p-dopant Gold(III)-chloride($AuCl_3$) was used. A stock solution of $AuCl_3$ in an acetone/toluene mixture (volume ratio of five to one), with a concentration of 2 g L^{-1} was prepared. Since $AuCl_3$

is highly hygroscopic, the material is weight in enclosed containers or in a glovebox. The stock solution and fresh solvent mixture were used to prepare 2 mL solutions of $AuCl_3$ with increasing concentrations. For BV a 2 mL solution with a concentration of 1 g L^{-1} was used.
To control the doping process, the IDE-thin-film sample was submerged in a solution of the dopant for 15 min. Afterwards, the sample is rinsed with a toluene/acetonitrile solution to ensure that the dopant doesn't form a conductive film on the IDE substrate, which could interfere with the conductance measurment.
The Conductivity measurements were performed using a BioLogic SP-50 potentiostat. The current was measured at a constant voltage of 0.1 V for 30 s. The current for the latter 50 % of the measurement was averaged to ensure that the system is probed in equilibrium. The resistivity was then calculated, using Ohm's Law.

5.1.2 Results and Discussion

SWNT film pretreatment

One common issue when performing measurements with SWNT-thin-films is that due to interaction with ambient water, the films often show a slight oxidation (or p-doping) [205]. Since we aim to probe the effects of doping on the conductivity compared to the intrinsic state, this oxidation is an issue. In order to ensure that the films are as close as possible to the intrinsic state, the films are treated with Benzylviologen (BV), a reduction agent. In order to avoid contaminating the following doping series with BV, the films were rinsed with toluene afterwards.

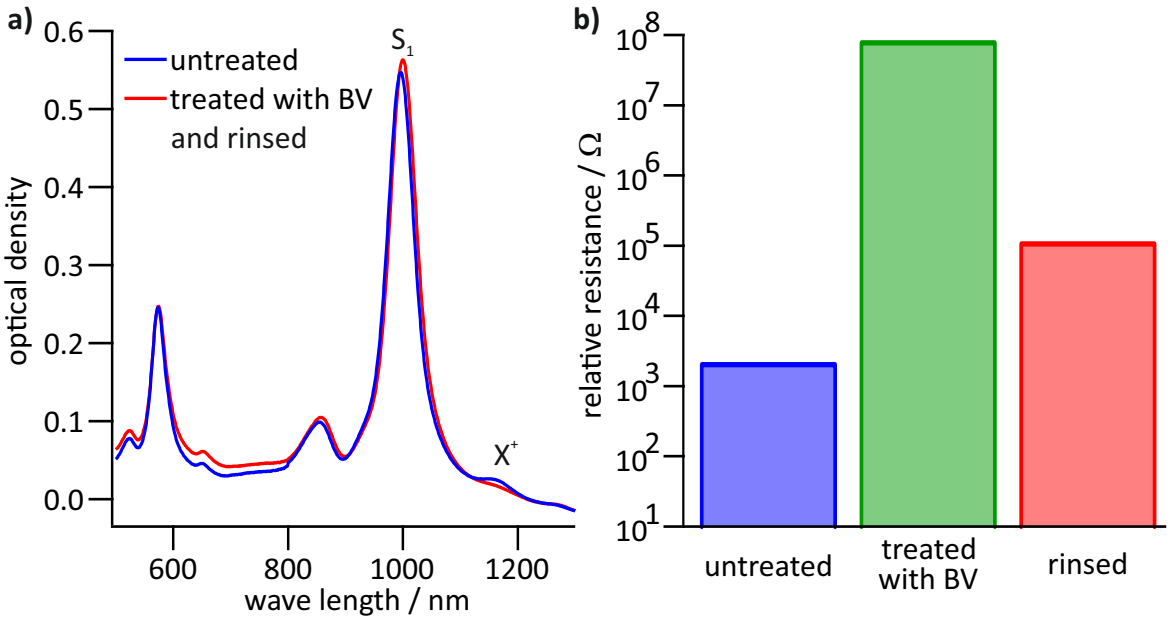

Figure 5.4: a) Absorption spectra of an as produced untreated SWNT-film on IDE(blue) and the after treatment with BV and rinsing the film with toluene. The trion signal X^+ is quenched and the excitonic S_1 peak is slightly red-shifted, consistent with a decrease in doping intensity. b) Measured resistance corresponding absorption spectra of SWNT thin-films. Treatment with BV increases the resistance massivly, while rinsing reduces although not the level observed before treatment.

Figure 5.4 shows the effects of this BV treatment. While Kim et al. [204] report that (6,5) SWNTs can be n-doped via viologen treatment, absorption and resistivity measurements indicate that SWNTs are much closer to the intrinsic electronic state after treatment than before. The untreated spectrum of the SWNT thin films shows a slight trion signal at 1170 nm, indicating an expected slight intrinsic oxidation. Treating the film with BV quenches this signal completely. Furthermore, comparing the measured resistivity, we observe that treating the film with BV increases the measured resistivity by a factor of about 10^8. Rinsing decreases the resistivity somewhat to about 10^5, indicating that a small amount of doping occurs even in the small window of time between BV treatment and rinsing. Alternatively, Ferguson et al. [206] suggested in their publication that rinsing could decrease the PFO-BPy content in the film, thereby increasing the contact surface between nanotubes inside the polymer matrix. While this would explain the decrease in resistance between BV treated films and rinsed films, the increase in resistance and the changes in the absorption spectrum nevertheless suggest that the untreated films are much closer to the undoped state than before.
No trionic signal or other signs of n-doping were observed. This is not necessarily the expected result. The reduction potential of the V^+ to V^0 of −0.79 V is in principle sufficient to remove charges from the (6,5) conduction band with its bandgap of 1.55 eV. Due to the symmetry of conduction and valence band around the Fermi-level, a potential of −0.775 V or lower should be sufficient. However, BV does not seem to be capable of introducing stable charges on (6,5) SWNTs. The introduced charges may be unstable under atmospheric conditions and are quickly removed via reaction with ambient water and oxygen. However, Kim et al. [204] claimed to have found evidence for n-doping in a polychiralic sample. It is possible that SWNTs with a larger diameter and smaller bandgap can achieve stable n-doping using BV, while (6,5) can not. Regardless of the reported results, the changes in the absorption spectra and resistivity are far more consistent with a de-doping than n-type doping. While that makes BV unsuitable doping experiments of (6,5) SWNTs, it can still be useful to eliminate the intrinsic p-doping that is often found in as-prepared SWNT samples. The BV-treated and rinsed films were used as a starting point for a series of absorption spectra and resistance measurements with increasing p-doping levels using $AuCl_3$ as an oxidizing agent. The results are depicted in figure 5.5.

P-doping series

The resistivity first falls drastically, consistent with observations from the BV treatments, where removing the small oxidation caused by ambient water increased resistance by a similar value. The initial doping steps reintroduce oxidation, so similar behaviour is to be expected. After this initial drop, the resistance drops at a significantly lower rate. The inset shows a double logarithmic graph for the resistivity after the initial two data points. The drop in resistivity remains somewhat linear between $AuCl_3$ concentrations of 3 µg mL^{-1} to 50 µg mL^{-1}, which is closer the behavior observed in silicon doping [207]. After 100 µg the resistivity does not meaningfully change with increasing dopant concentration.

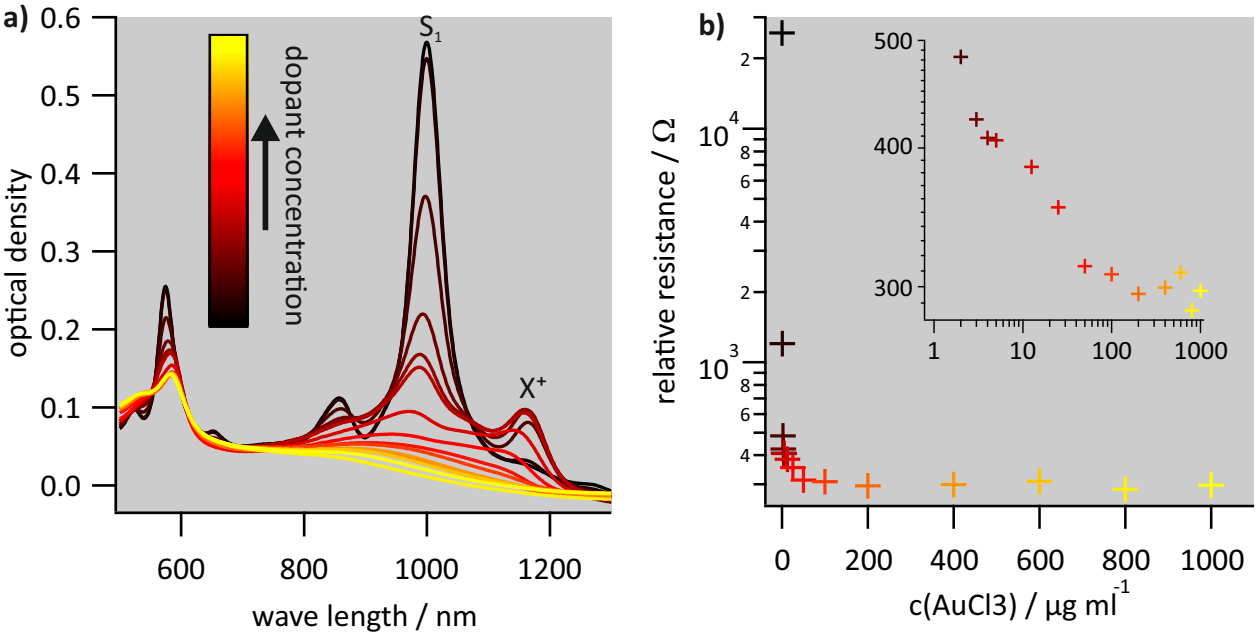

Figure 5.5: a) Absorption spectra of the SWNT thin-film/IDE sample with increasing dopant concentration. Initially the excitonic signal S_1 decreases while the trionic signal X^+ increases. At very high doping level even the trionic peak is quenched. These changes are consistent with p-doped SWNT films [22]. b) The resistivity measurements of the sample samples. The color of the datapoint corresponds to the absorption spectrum of the same color. The inset shows a double logarithmic plot without the first two datapoints. The two initial steps reduce the resistance far stronger than any following steps, and behave superlinear even in a double logarithmic plot.

The initial sharp drop in resistivity might result from decreasing contact resistance between SWNT film and electrode. Another factor proposed by Ferguson et al. [208] is that submerging the film in solvent removes excess SWNT, which in turn increases the conductivity of the film. However, this explanation is not consistent with the observed increase in resistivity when treating the film with BV. If anything, a treatment with toluene dissolved BV should remove more PFO-BPy. Even higher dopant concentrations do not change the resistivity by much, indicating that the SWNT material might be saturated with charge carriers. This would essentially constitute a degenerate semiconductor, a state in which defect sites are so close together that they form a continuous band. This is consistent with other experimental observations, including the EPR experiments elaborated on in the next chapter.

5.2 Charge carrier quantification via EPR

A major challenge in understanding doping in SWNTs is the character of the introduced charges. Of particular importance is the question of localization: Are charges trapped in a segment of the SWNT, or are they delocalized and move freely across the tube axis? Earlier reports suggested that homogeneous distributions of charges [209], indicating free movement. However, recent research indicates that charges may be instead localized, and the changes in fluorescence and absorption spectra are the result of the excitons' interactions with these charges [76]. Both approaches have been elaborated on in section 2.1.3. So far, these investigations into the charge behaviour have relied on indirect observations via the absorption and fluorescence spectra of nanotubes.
A direct way of observing localized charges may provide a more definite answer to the question of localization. A very promising approach to gain more insights into this question is to quantify the amount of charge on an SWNT via electron paramagnetic spin resonance spectroscopy (EPR). The detection spins density in doped carbon nanotube samples would strongly suggest localized charges. The experimental aspects and the resulting data are presented in the following chapter.

5.2.1 SWNT suspension preparation

Quantitative EPR spectrometry can be used to quantify the amount of charge in a given sample, provided the charges carry a non-zero spin. By continuously doping an SWNT-suspension, the charge density on the nanotubes increases. Observing the changes in the EPR signal, we can obtain information about the density and character of the introduced charge carriers. Suspensions of (6,5) SWNTs have been prepared via shear-mixing as described in 3. The resulting SWNT suspension only contained a small amount of SWNT, with a mass concentration of about 1.5 mg L^{-1}. While this is sufficient for optical spectroscopy, EPR experiments require significantly higher concentrations, as mentioned in section 2.5. In order to increase the sample concentration, the SWNT suspensions were first vacuum-filtered through a 0.1 µm Isopore Membrane Filters (Ref: VCTP01300) using a standard filtration setup for membrane filters (Merck Millipore XX1012500 Microanalysis filter holder). Since the overwhelming majority of SWNTs are longer than 0.1 µm [53], almost the entire CNT content is caught on the filter. The process is illustrated in figure 5.6

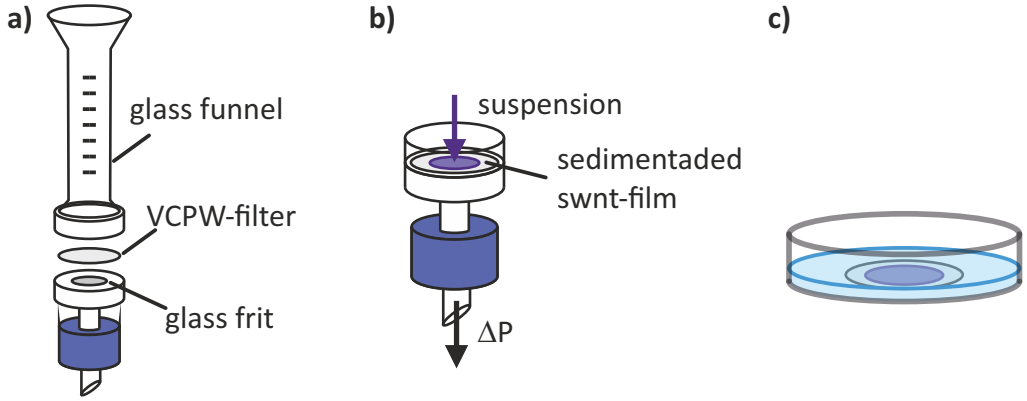

Figure 5.6: Schematic illustration of the production of concentrated SWNT suspension. a) Using a XX1012500 Microanalysis filter holder setup the 0.1 µm filter is placed according to manufacturer instruction b) SWNT suspension is pulled through the filter via a vacuum applied to the glass flask after the filter. c) The SWNT film is placed into an acetone bath to dissolve the VCPW filter.

The filter is then dissolved by transferring the film into an acetone bath, which is then shaken for 20 minutes, using an MS1 Minishaker (IKA) at about 1 Hz rotation speed. The acetone is removed and replaced by fresh solvent after the 20 min run time. This process is repeated three times to eliminate all filter material quantitatively. The SWNT-film is then placed in a fourth and final acetone bath and kept there overnight. The film is then re-dispersed in the desired volume of on acetonitrile/toluene (volume ratio 1:5), using a sonication bath (Bandelin Sonorex Super 10 P) for 45 min at 100 % intensity. The addition of acetonitrile to solvent is necessary to ensure sufficient solubility of $AuCl_3$. The temperature was kept at 20 °C by adding ice to the sonication bath as needed. Absorption spectra of the now concentrated solution were taken.

$AuCl_3$ was likewise dissolved in an acetonitrile/toluene mixture. The $AuCl_3$ were then added to the SWNT-suspension in 10 µL steps. After each doping step, the solution was bath sonicated for 15 min. The addition of $AuCl_3$ solution dilutes the SWNT content in the sample. For the EPR measurements, this was not an issue since the entire sample remained inside the magnetic field, so despite the increased volume, all of the SWNTs were probed. For the absorption spectra, where only the concentration inside the light beam is captured, the dilution was corrected via division through the dilution factor.

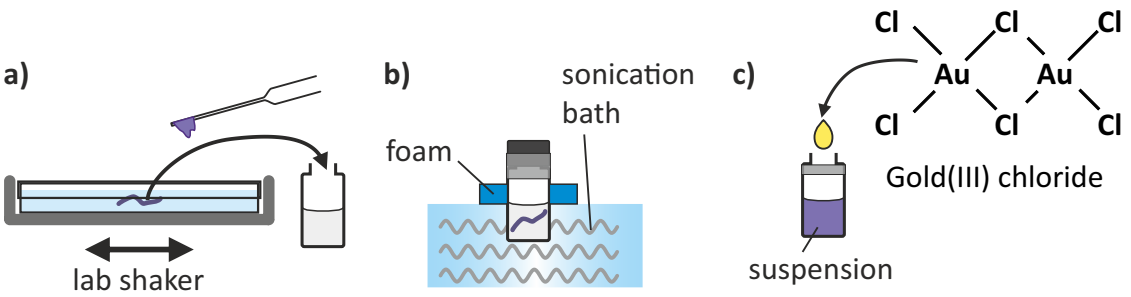

Figure 5.7: Illustration of the final steps in sample preparation for EPR-experiments. a)The previously produced SWNT thin-film is taken from the acetone bath and put in a 1 mL screw cap glass with 1:5 acetonitril:toluene solvent mixture. b) The screw cap glass is placed in a sonication bath, using a foam swimmer. The glass is insulated with parafilm to prevent evaporation of solvent. c) $AuCl_3$ dissolved in acetonitrile:toluene solvent is added in 10 µL steps.

The material for the absorption measurement series and the EPR series were taken from the same stock SWNT suspension and the same stock solution of $AuCl^3$.

Concentration of SWNT suspensions

Quantitative EPR measurements require knowledge of the total amount of SWNT-material present in the sample volume. The SWNT concentration can be determined by absorption spectroscopy as described by Schöppler et al. [166]. With the known molar absorption coefficient and using Lamber-Beer-Law, the following equation can be used to quantify the molar concentration of carbon in a given sample.

$$c_C = B\frac{\Delta_{fwhm} OD}{fd} \tag{5.1}$$

Since we do not probe a free electron, but charges are localized in a carbon-based compound, the measured g-factor differs from the electronic g-factor of 2.00233.

5.2.2 Experimental results and discussion

The EPR experiments were performed by Michael Auth [210], while Florian Oberndorfer carried out the sample preparation and absorption spectroscopy. Both series were conducted in parallel to match the experimental conditions between the measurements as much as possible. The absorption spectra series is shown in figure 5.8.

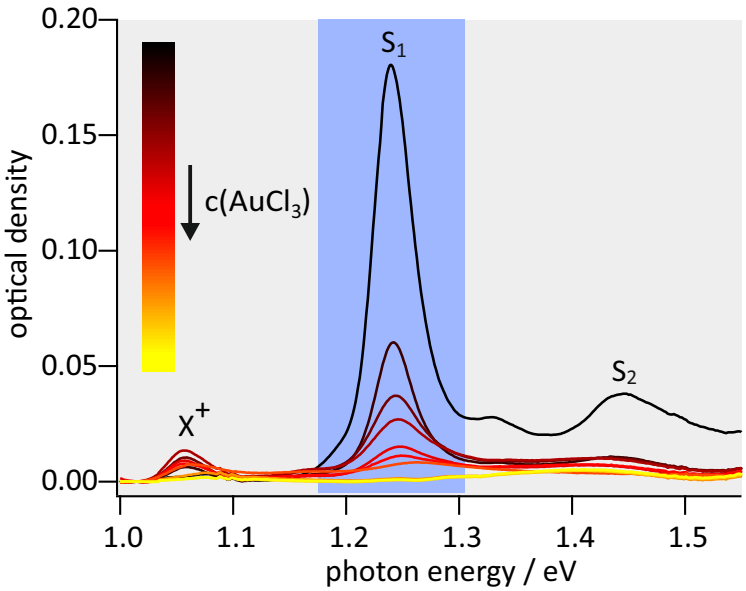

Figure 5.8: Absorption spectra of the SWNT suspension, with increasing $AuCl_3$ concentration. The precise $AuCl_3$ concentration is documented in table 5.3.1. The spectra are zeroed to the intensity at 0.95 eV. A correction has been applied to account for dilution of the suspension during the experiment. The blue are indicates the integral range, that is used to determince the charge density of the SWNTs via phase-filling and localization models.

The expected changes in spectral behaviour are present: A decrease in S_1 exciton absorbance, concurrent with an increase in X^+ trion absorbance. Integration over the absorbance signal can be used to determine the initial SWNT concentration of the suspension, as described in section 5.2.1.
Quantitative EPR spectroscopy directly measures the spin density of a sample. This value is not necessarily identical with the charge density since only charge carriers with a spin $S \neq 0$ can be detected. Therefore a comparison between the charge carrier concentration and the spin density can provide insights into the character of the charges in SWNTs. The detected spin-densities with increasing dopant concentration are shown in figrure 5.9

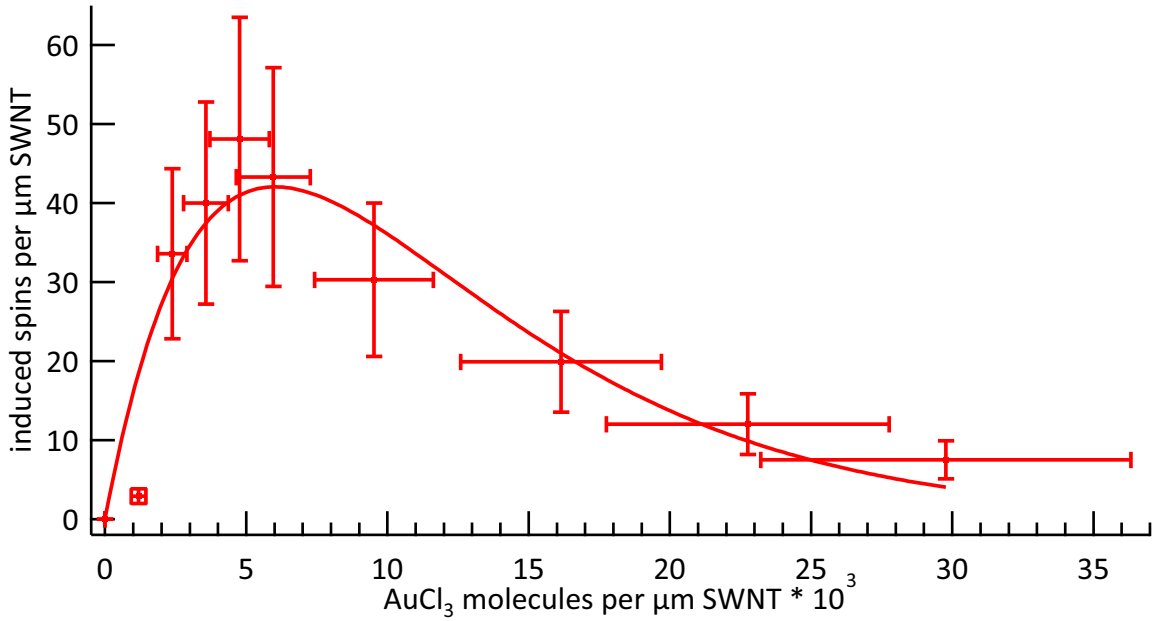

Figure 5.9: EPR-Signal of a (6,5)-PFO-Bpy suspension, with increasing $AuCl3_3$ concentration. By referencing the spectrometer to a sample with known charge density the signal can be correlated to the charge density on the tubes. The signal increases at first, since almost all induced charges also produce an addtional spin. As more charges are added the probablity of isolated spins decreases. Neighboring spins can start to form +1/2 -1/2 spin couple which shows no outward spin and thus produces no signal.

The results are noteworthy in several regards: First of all, the fact that doping induces a detectable spin signal indicates the presence of localized charges under the given experimental conditions (T = 10 K). Free charges would move along the tube, which means their environment would change much quicker than the measurement time, drastically broadening the EPR band, which can then no longer be distinguished from background noise in the EPR spectrum. Thus, a measurable spin signal indicates the localization of electronic spins and, consequently, charge localization. Secondly, the fact that a maximum in spin density is observed indicates that saturating the SWNT with charges changes the character of the charge carrier, making them effectively invisible to EPR measurements. Experimental results of other groups support the notion that charge carriers are predominantly free at room temperature. Ferguson et al. [206] estimated that at least 47 % of all charge carriers are free in percolated SWNT-networks, based on microwave and DC measurements [206].
Nevertheless, the signal of isolated spins on the SWNT is direct evidence of localized charges, which previous experiments could not conclusively prove. The experiments of Ferguson et al.

[206] were carried out at room temperature while EPR spectrometry was performed at 10 K, so charge carriers may become free, provided they have sufficient kinetic energy to escape their charge trap. Applying the phase space-filling and localization model to absorption spectra data can also produce charge densities for the (6,5) SWNT absorption spectra. A comparison of the resulting charge densities and the ESR active spin density is shown in figure 5.10.

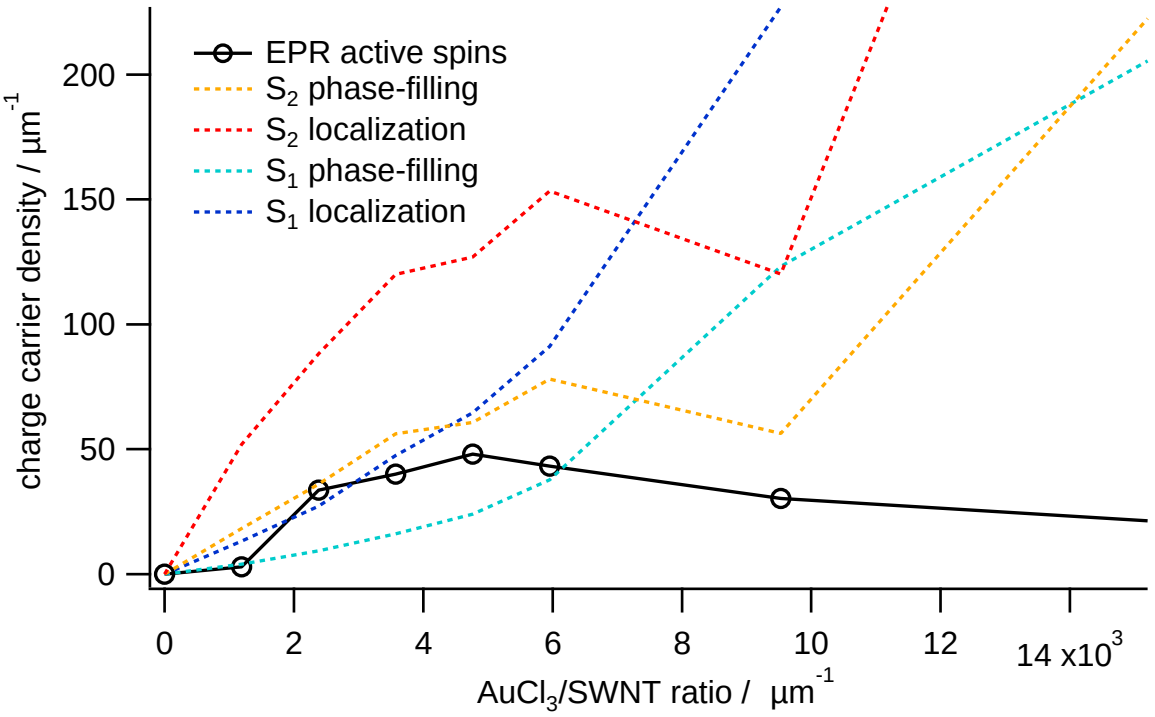

Figure 5.10: Charge carrier densities as determined by absorption spectra and EPR spectroscopy. The charge concentration for absorption spectra were determined by measuring the first and second excitonic transition and application of both a phase space filling and charge localization model. The dotted colored lines show the charge densities, with the different methods. The black line indicates the spin densities, as measured by quantitative EPR.

Until an $AuCl_3$/SWNT ratio of about 50000, the EPR signal and the charge densities follow the same trajectory. After this point, the amount of measurable spins declines, while the charge density, as determined by both models, further increases. Since the amount of dopant is continuously increasing, so should the density of charges and spin signal on the SWNT. It appears that upon reaching higher levels of doping, the localized nature of the spins is lost, making them effectively invisible for EPR experiments. This observation would not necessarily be inconsistent with charge localization models. One possible explanation for this behaviour is that with increasing density of charges, the spins can no longer be considered isolated from other neighbouring spins. Interaction of two neighbouring spins could result in a state with an outward spin of 0. The charges could then no longer be detected by EPR spectroscopy (illustrated in image 5.11). If the doping level becomes high enough, the charge densities become continuous across the entire tube, in which the charges would effectively become delocalized, which also bleaches the EPR signal.

Another possible factor are aggregation processes during the experiment. In reference measurements, suspension with a higher SWNT concentration (and thus more aggregation) curiously produced a weaker maximum spin signal, despite a higher amount of SWNT-material present. Doping an SWNT suspension generally increases agglomeration as well, most likely due to PFO-BPy not being able to stabilize highly charged tubes. Consequently, aggregation may contribute to the decreasing signal strength. However, it is unclear how aggregation might bleach the EPR signal. Most likely, aggregated SWNTs have a smaller exposed surface, on which $AuCl_4^-$ molecules can form charge traps. This would then reduce the activity of the SWNT, as less material is available for the electrochemical reaction with $AuCl_3$.

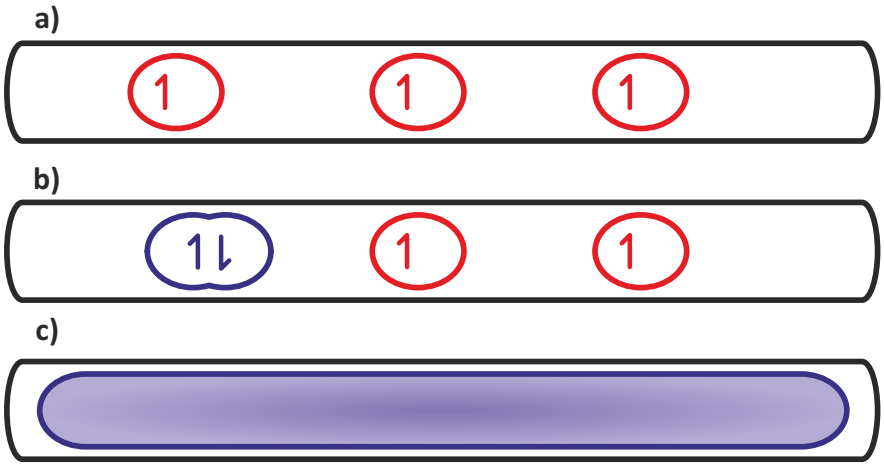

Figure 5.11: Illustration of our model for increasing amount of charges on the SWNT. Initialy every charge introduced in the SWNT results in one additional measurable spin. However at some point the charge density increases to a point where additional charges are likely to interact with existing charges and thus decrease the amount of measurable spin density. At the extreme end charges are delocalized across the entire tube, resulting in no measurable spin density.

Another critical piece of the information is the EPR signal of SWNTs doped to the maximum extent, in the following text referred to as degenerate doping. Curiously the EPR signal is weaker than the signal measured of intrinsic tubes. On closer examination, we can see that there are two signal components at different g-factor values, 2.0024 and 2.0069, as shown in figure 5.12. Degenerate doping bleaches only the signal at g = 2.0024 while the other component remains as is. Given the dependence on dopant concentration, the most likely explanation for the g = 2.0024 signal is that charges induced on the SWNT generate this component. The fact that there is an intrinsic signal can be explained by doping through interaction with ambient water as described by Aguirre et al. [205]. Degenerate doping bleaches this signal compared to the intrinsic state, which suggests that intentional and intrinsic doping have identical origins. The remaining signal at g = 2.0069 can also be found by measurements of the unprocessed CoMoCat SG65i raw material, indicating that it is not, in fact, a result of doping but instead defects in the SWNT like dangling bonds, which are also reported to be the main reason for fluorescence quenching [54].

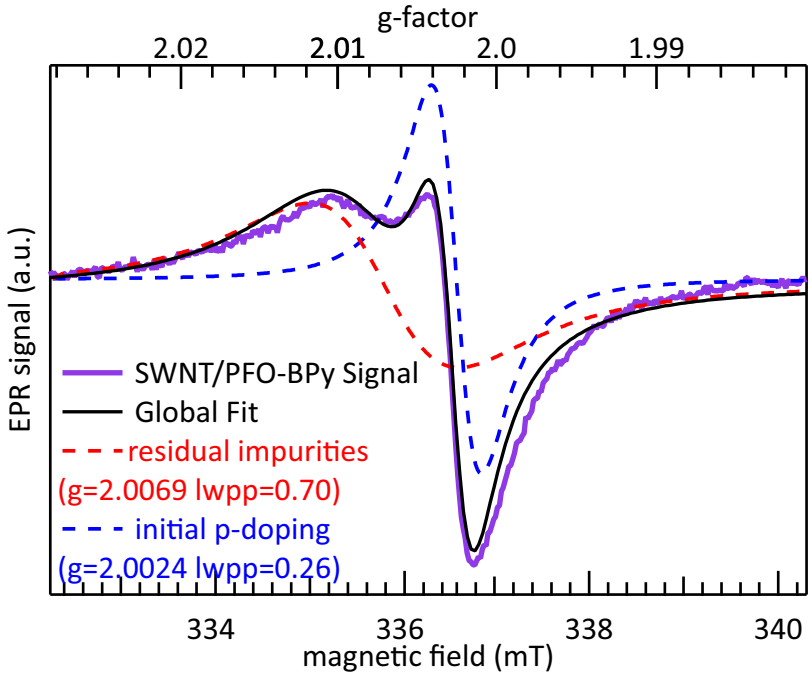

Figure 5.12: The SWNT shows two signal components. The residual impurities (marked red) indicate carbon defects, such as dangling bonds which can produce an EPR-Signal. In addition to that SWNTs are intrinsicly already slighly doped, even without addition of oxidizing agents. This initial p-doping (marked blue) results from in interaction of the tube with ambient water [205].

These results also give information about the number of intrinsic defects in the SWNT/PFP-BPy sample. The total amount of defects per tube is 10.2 μm^{-1}, which translates to an average length for a defect-free nanotube segment of 98.0 nm. This value is somewhat lower than the mean distance between defects, determined by transient absorption spectroscopy (192.1 nm). However, with an average tube length for shear-mixed SWNT suspensions of 1 µm and the fact that the tube ends also act as defects, both values indicate an extremely low defect concentration on the tube themselves. The discrepancy might be due to EPR-active defects, which do not cause non-radiative decay. Since the defect concentration in both cases is minuscule, slight deviations in the degree of intrinsic doping due to environmental effects can also cause considerable relative deviations.

5.3 Raman spectroscopy of doped SWNTs

Investigating doped SWNTs can be a challenging problem. Otherwise, very reliable methods like photoluminescence spectroscopy are not viable since PL signals are quickly quenched at even small charge concentrations. While absorption spectroscopy has yielded a considerable amount of insight into doped SWNTs, supplementing it with other methods can help investigate physical properties that are otherwise difficult to access. Correlating Raman spectra to charge density obtained by absorption spectra can help verify existing models and provide further insights into

how SWNT changes with the introduction of excess charges. The following chapter presents the sample preparation and experimental details for doping SWNT suspensions, followed by absorption and Raman spectroscopy.

5.3.1 Experimental aspects

Sample preparation and doping

(6,5) SWNT dispersed in a 5:1 aceto-nitrile/toluene mixture with PFO-BPy as dispersion agent were successively doped with Gold(III)-chloride dissolved in the same solvent mixture. The procedure to produce the suspensions was identical to the one described in section 5.2.1, except that concentrations after re-dispersion were kept at a lower level, with an optical density of 0.55 at 1000 nm, which corresponds to a mass concentration of 0.8 mg L^{-1}. Throughout the measurement series $AuCl_3$-solution was successively added to the SWNT suspensions in a fully transparent optical cuvette (Hellma 101-QS). After carefully shaking the suspensions for a few seconds, Raman spectra of the sample were taken. In total fifteen $AuCl_3$ concentrations were probed. The precise values for each step are found in table 5.3.1.

Table 5.1: Concentrations of dopant used in the following measurement series.

sample number	0	1	2	3	4	5	6	7	8	9
c($AuCl_3$) / µg L^{-1}	0	0.04	0.06	0.17	0.54	0.89	2.66	4.37	6.02	7.61
sample number	10	11	12	13	14					
c($AuCl_3$) / µg L^{-1}	9.15	10.64	12.08	15.06	17.95					

Charge quantization via absorption spectroscopy

Absorption spectra were taken using the same equipment and parameters as described in section 3.3.1, with the only difference that the previously mentioned fully transparent cuvette (Hellma 101-QS) was used. The SWNT charge concentrations were determined by correlating the excitonic bleach to the phase-space filling charge quantization model, which is described in more detail in section 2.1.3.3. The exciton bleach was measured by integrating the absorption spectra between 1.1945 eV to 1.3037 eV and normalizing them on the value of the initial undoped suspension.

Raman spectroscopy

The Raman measurements were performed using a setup built by Friedrich Schöppler, which illustrated in figure 5.13. As an excitation laser, a Coherent Sapphire LP 50 mW 568 nm laser was used since its laser wavelength is resonant to the second excitonic transition of (6,5)-SWNTs. After passing through a T80/R20 beam-splitter, the excitation laser was focused on the sample via

a 10x Nikon objective. The beam-splitter heavily favours transmission since the Raman scattering intensity is weak compared to the laser beam or Rayleigh scattering. Therefore an asymmetric beam splitter can considerably lower the necessary integration time.

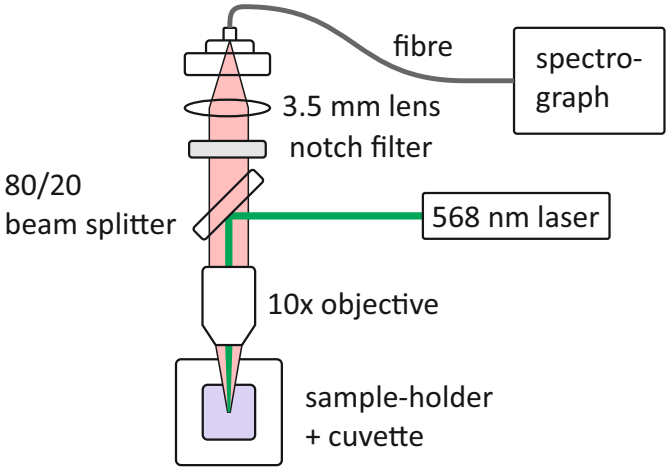

Figure 5.13: Schematic representation of the Raman spectroscopy setup. The green beam is from the excitation laser, while the red beam indicates scattered radtion.

The scattered radiation was captured by the objective and focused into an optical fibre connected to a Princeton spectrograph, alongside the software provided by the manufacturer. A notch filter before the focusing lens eliminates the remaining laser radiation at 568 nm]. For one spectrum, 20 accumulation with an exposure time of 30 s for each were taken.

5.3.2 Results and discussion

In order to correlate the charge density of SWNTs with the changes in their Raman signal, absorption spectra have been taken in tandem with the Raman spectra. As explained in the experimental section of this chapter (5.3.1), correlating the exciton bleach or the peak shift to a band-filling model can yield the charge concentrations. The absorption spectra and corresponding densities are shown in figure 5.14. The precise $AuCl_3$ concentrations are found in table 5.3.1.

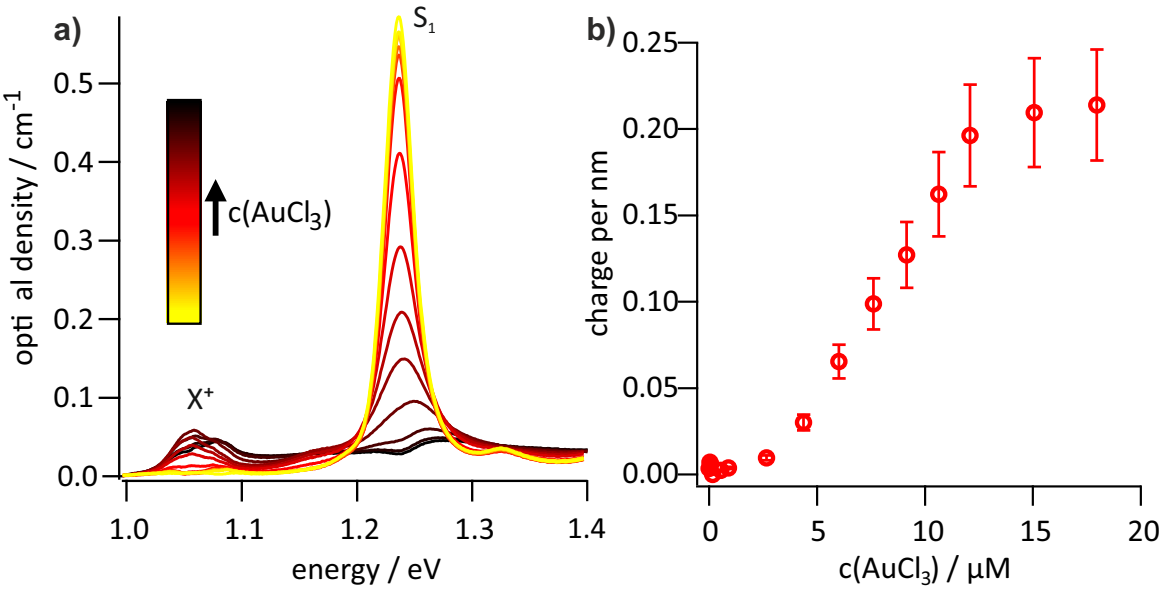

Figure 5.14: Image a) shows a series of 6,5 SWNT spectra with an increasing amount of $AuCl_3$ in the suspension. The precise values can be derived from table 5.3.2. With increasing dopant concentration E_{11} oscillator strength at 1.24 eV decreases while the trionic signal at 1.05 eV increases. At the highest concentrations, the trionic signal appears to decline as well, moving into the H-band regime [76]. In Image b) charge density on the nanotube is quantified using the integral of the absorption spectra from 1.95 eV to 1.30 eV using a method described by Eckstein et al. [94]

The initial few data points are very close to each other, which results in the tight bundle of points in the image 5.14 b). Other than that, the expected changes in the absorption are present: A decrease in S_1 exciton oscillator strength, as well as an increase in the trionic signal X^+.
Figure 5.15 a) shows the corresponding Raman spectra and their changes with increasing dopant concentration. The Raman spectra undergo two significant changes: Firstly, the G^+ band loses sharply in intensity, compared to the relatively minor drop in S_1 absorbance that is seen in the first doping steps. Furthermore, a subtle line shift of the G^+ band is detectable. The correlation with this peak shift to the charge density is illustrated in figure 5.15 b).

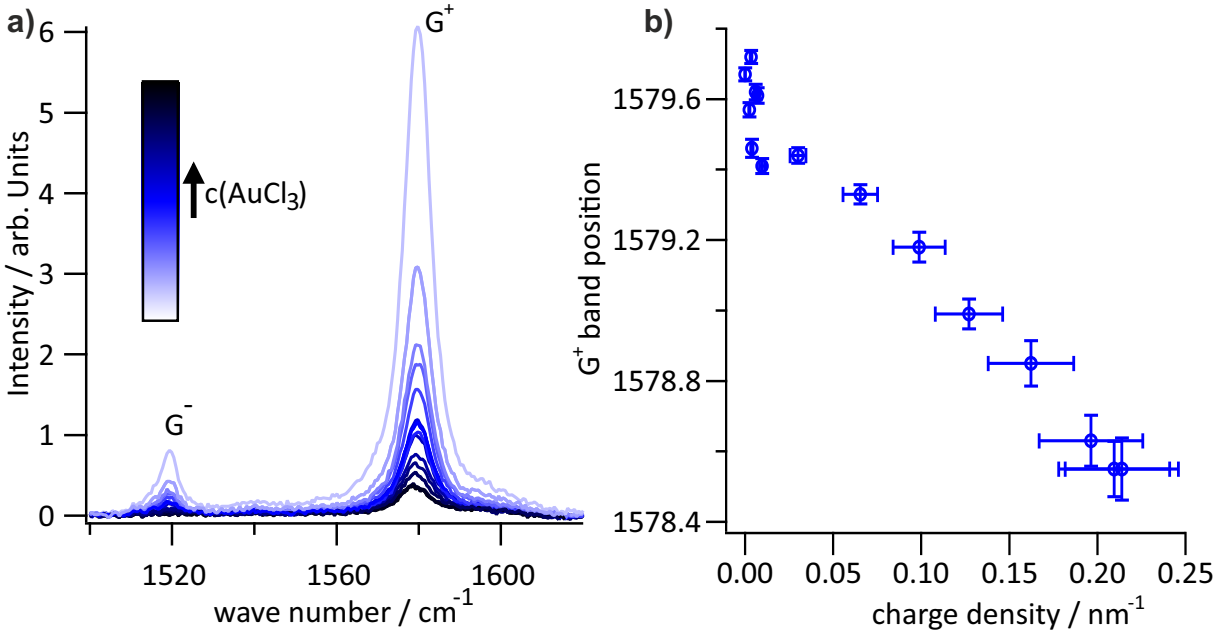

Figure 5.15: a) Raman spectra with increasing $AuCl_3$ concentration. With increasing dopant concentration the G^+ and G^- Raman band decreases in oscillator strength. Furthermore a subtle shift in resonance frequency can be observed. b) illustrates the peak shift in the G^+, correlated with the charge densities derived from absorption spectra as illustrated in image 5.14. Until high dopant regimes an almost linear correlation can be observed.

The Raman band red-shifts with increasing doping levels. However, only when entering the heavy doping regime, the observed changes become significant.Farhat et al. [211] reports that shifting the Fermi level of individual metallic SWNTs decreases the G^+ frequency. This change is attributed to phonon softening due to the Kohn Anomaly. However, they report far more significant shifts of about 5 cm^{-1} to 20 cm^{-1}, compared to the 1.2 cm^{-1} maximum shift that was observed in this experiment. Furthermore, semiconducting SWNTs are not predicted to be impacted by Kohn anomalies since those are distinct features of the phonon dispersion in metallic systems. It is possible that the depletion of valence π bands with decreasing Fermi level weakens the aromatic C-C bonds along the tube axis. This would lower the force constant for vibrations along with these bonds and consequently lower the excitation energy for the G^+ phonon.

The second significant change in Raman spectra is the decrease in G^+ intensity. A significant part of this can be attributed to the loss of the resonance condition. As can be seen in the absorption spectra in image 5.16 the S_2 transition, which is resonant with the 2.18 eV laser, decreases in oscillator strength and red-shifts to 2.10 eV. Furthermore another signal arises are 2.2 eV. While the absorbance at 2.18 eV is only partially lost, it is nevertheless significantly diminished, so a linear proportional decrease in resonant Raman amplification and thus the Raman signal is to be expected.

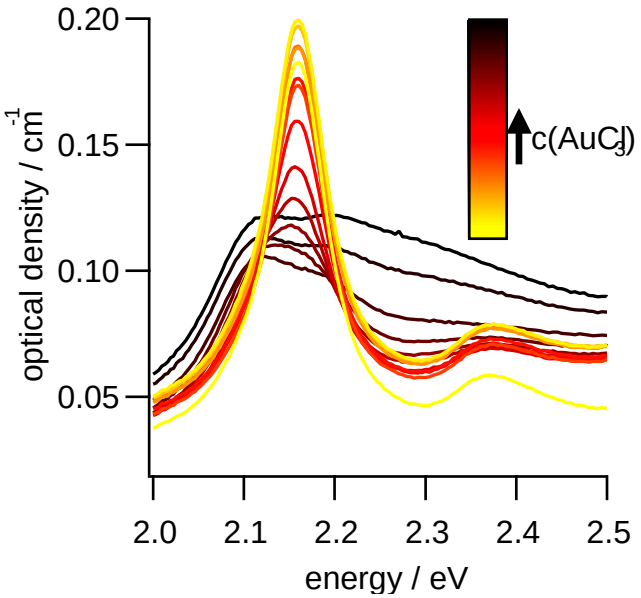

Figure 5.16: Change in S_2 absorbance with increasing dopant concentration. The overall absorbance at 2.18 eV. The loss of oscialltor strength of S_2 exciton is partially offset by a new signal at 2.10 eV.

However, correlating the absorbance at 2.18 eV (or 568 nm) with the G^+ peak does not produce completely linear behaviour. As seen in 5.17 b), there is one anomalous data point (marked in blue), as well as a slightly superlinear increase of the G^+ band with increasing absorbance. The anomalous data point belongs to the undoped Raman spectra. The Raman intensity drops sharply upon initial doping then follows a more linear correlation with the resonance condition.

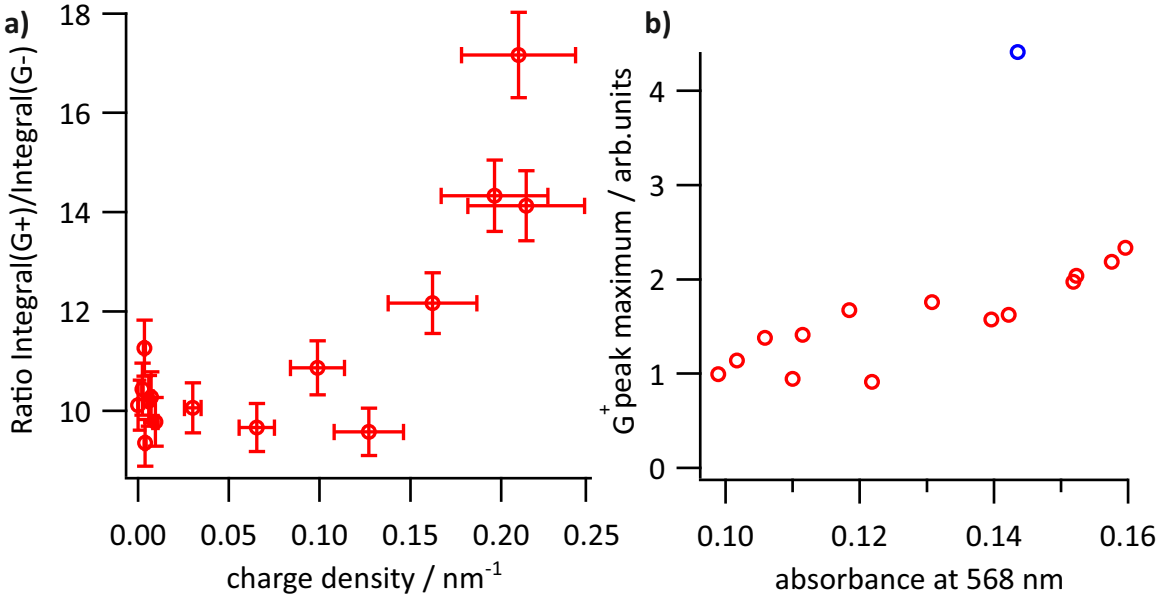

Figure 5.17: a) Ratio between the Integrals of G^+ and G^- bands, with increasing charge density. A sharp increase can be observed at hight doping levels. b) the G^+ band peak maximum with increasing absorbance at 568 nm. The blue marker indicates the undoped spectrum.

One possible reason might be a decrease in exciton lifetime. If the introduction of charges on the tube opens up a faster deactivation pathway for the S_2 exciton, it may decay non-radiatively before a Stokes shift can occur. Doping greatly decreases the exciton lifetime in SWNTs, even at comparatively low doping levels [212]. Matsuda et al. [212] report the nonradiative decay at charge densities of 0.1 nm^{-1} to be in the order of tens of picoseconds. This would still be considerably slower than the vibrational relaxation, that usally takes up to 1 ps. Therefore, a reduction in exciton lifetime doesn't seem to fully explain this intial drop-off, especially since the charge concentration is miniscule after the initial doping step.

However, even when ignoring the first doping step, the Raman resonance effect is not entirely sufficient to explain the changes in G-band intensities. Comparing the relative peak intensities of the G^+ and G^- band reveals a strongly nonlinear behaviour, as shown in figure 5.15. If the Resonance conditions were the only significant factor for the changes in G band intensity, it would have to impact both G^+ and G^- band equally. However, the ratio between the two shifts considerably with increasing doping levels, with G^- being bleached much faster. This divergence in the relative band intensities could also be caused by the introduction of additional exciton deactivation pathways during doping. Another possible cause might be an increase in agglomeration as the doping level increases. Polymer stablized SWNT suspensions become less stable upon doping, with visible flakes forming. If the G^- band is more sensitive towards aggregation than the G^+ band, than it would explain this divergence.

This question could not be further pursued in this dissertation, but the most promising way to do so is likely resonant Raman spectroscopy with tunable excitation wavelength. It might be possible to eliminate the change in scattering intensity caused by the loss of resonance. Second-order processes in SWNTs often involve scattering at defect sites, which makes it possible to determine defect densities in graphene and SWNTs, via the G^+/D ratio [137–139]. Correlating the defect density of doped SWNTs as determined by second-order Raman with the charge densities determined by absorption spectroscopy could provide more insight into how introduced charges impact Raman spectra.

5.4 Carrier Dynamics in Single-Walled-Carbon Nanotubes/Fullerene blend films

Charge transport within SWNTs and other nanomaterials is not as straightforward as bulk semiconductors. While charges inside of tubes can propagate according to a band transport model, charge transport inside the network appears to be far more heterogeneous, with variable hopping [213], tunnelling, and thermal activation models being proposed [214]. The diameter and chirality of the SWNT network also seem to have a profound effect on the pathway charges take,

with metallic and small bandgap tubes dominating charge transfer pathways [214–217]. Consequently, investigation of charge transport properties requires high purity samples, which are free of metallic tubes and other chiralities which might alter the charge behaviour. Fortunately, the previously discussed preparation techniques for SWNTs provide sufficient selectivity to enable experiments to elucidate the charge carrier dynamics between nanoscale semiconductor materials. In cooperation with Jašinskas et al. [202] SWNT and [6,6]-Phenyl-C61-butyric acid methyl ester (PCBM) blend films were probed using time-resolved electric field harmonic generation (TREFISH) in conjunction with other time-resolved methods like transient absorption.
In the following chapter, the experiments and conclusions that can be drawn regarding the exact dynamics of charges in SWNT and SWNT/PCBM blend thin films are shown in detail. Firstly the sample preparation of the SWNT/PCBM blend film on interdigitated electrodes is presented. Then follows a brief overview of the experimental techniques employed to investigate the charge transport between PCBM and SWNT. Finally, the experimental results and their significance for understanding charge transport in this system are presented.

5.4.1 Experimental aspects

5.4.1.1 SWNT/PCBM suspension preparation

Metallic SWNTs dominate charge transfer in percolated networks films if they are present in the sample [217]. Consequently, it is crucial to perform conductivity experiments with samples containing only semiconducting SWNTs. PFO-BPy wrapping is highly selective towards semiconducting (6,5) SWNTs and is currently the best option to prepare high purity suspensions [152, 153]. Polymer wrapping is strongly diameter sensitive and, for reasons that are not well understood, highly selective towards semiconducting tubes.

(6,5)-SWNT suspensions were prepared via tip-sonication in a toluene solution, as previously described in section 3.2. The SWNT-suspensions were used to prepare an SWNT film via vacuum filtration (described in section 5.2.1). The resulting SWNT films were redispersed in fresh chlorobenzene. The sonication parameters were 100 % intensity at 20 °C for 15 min.The redispersion step serves two purposes: Firstly, it reduces the PFO-BPy content to a minimum, allowing finer control of polymer content by adding the desired amount afterwards. Most PFO-BPy molecules are not wrapped around SWNTs but are dissolved in the suspension solvent. This superfluous polymer is washed out during filtration, drastically reducing the polymer to SWNT ratio in the sample. Secondly, it provides an environment where SWNT, PCBM and PFO-BPy are stable, unlike toluene, which can not dissolve PCBM.

In order to investigate charge transfer between PCBM and SWNT, the different current components need to be differentiated. Charge propagation solely inside the percolated SWNT network

or a PCBM film has to be distinguished from signal components, which result from charge transfer between the two materials. Four different kinds of samples have been prepared to make this distinction. The necessary films were prepared using drop-casting from a set of suspensions, which were mixtures of three stock solutions: The suspension of SWNT in chlorobenzene with an optical density of 1.66 (2.6 µg mL^{-1}), a PCBM solution in chlorobenzene with a concentration of 1.89 mg mL^{-1} and PFO-BPY solution with a concentration of 1.90 mg mL^{-1}. An overview of the different target sample properties can be seen in table 5.2.

Table 5.2: Target properties for the four different kinds of samples needed for time-dependent photocurrent measurements.

sample index	1	2	3	4
SWNT	no percolation	no percolation	no percolation	percolation
PCBM	continuous film	no continuous film	—	—

In Sample 1, SWNTs do not produce a percolated network, while PCBM makes a continuous film, so the overall current will be dominated by PCBM propagation through the PCBM environment. In Sample 2, neither component forms a film, which would allow a current to flow exclusively through one material, so charge transfer between the two should be maximized. Sample 3 is a reference that contains predominantly isolated SWNTs, due to the high PFO-BPy content, so only minimal current should be observed, while reference sample 4 is a polymer depleted SWNT film, in which the current is solely the product of tube-to-tube charge propagation.

5.4.1.2 SWNT/PCBM thin film preparation

To enable the photo-current measurements, SWNT/PCBM blend films were produced on interdigitated electrodes (ED-IDE3-Pt, Micrux Technologies) via drop-casting. SWNT-suspensions, PCBM-solutions and PFO-BPy solutions described in section 5.4.1.1 form the basis for four different solvent mixtures, one for each signal component. The exact compositions are listed in table 5.3.

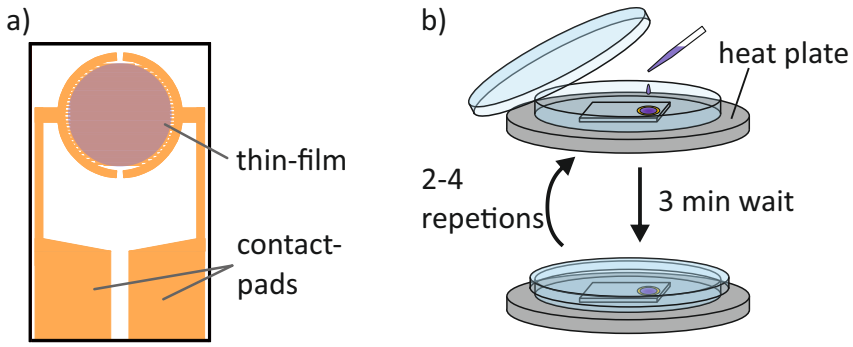

Figure 5.18: a) To-scale illustration of an interdigated electrode. The round thin-film area marks the interdigated area and where the thin-film was deployed b) Schematic illustration of the drop-casting process

The target area of the interdigitated electrodes is a circle with a diameter of about 1.8 mm. Therefore drop-casting can only be done with volumes of about 2 µL to 4 µL. In order to achieve the desired film thickness and optical densities, drop-casting was performed multiple times to accumulate a sufficient amount of material. The precise value for the four different sample types are listed in table 5.3. As illustrated in figure 5.18 the drop-casting was performed on a heat plate, with drying taking place within a closed petri dish. This serves mainly to reduce capillary flow and provide a more homogeneous material deposition. Deposited material outside the IDE was removed by wiping it away with toluene soaked paper towels.

Table 5.3: Drop-casting suspension composition for photocurrent measurements. SWNT, PCBM and PFO-BPy indicate the suspension or solutions as described in section 5.4.1.1. The numeric values indicate how many parts of this solution were taken to produce the target suspension. The dropcasting values indicate how often the given mixtures were dropcast and at what volumes.

sample index	1	2	3	4
SWNT	1	8	4	1
PCBM	2	1	—	—
PFO-BPy	—	4	1	—
drop-casting	$4 \times 2\,\mu L$	$4 \times 2\,\mu L$	$4 \times 4\,\mu L$	$4 \times 4\,\mu L$

The composition of the four different IDE samples types was verified using absorption spectrometry. Using an Agilent Cary 5000 spectrometer with a film module, absorption spectra were taken between 300 nm to 1200 nm. An example spectra for the four different sample types is shown in figure 5.19.

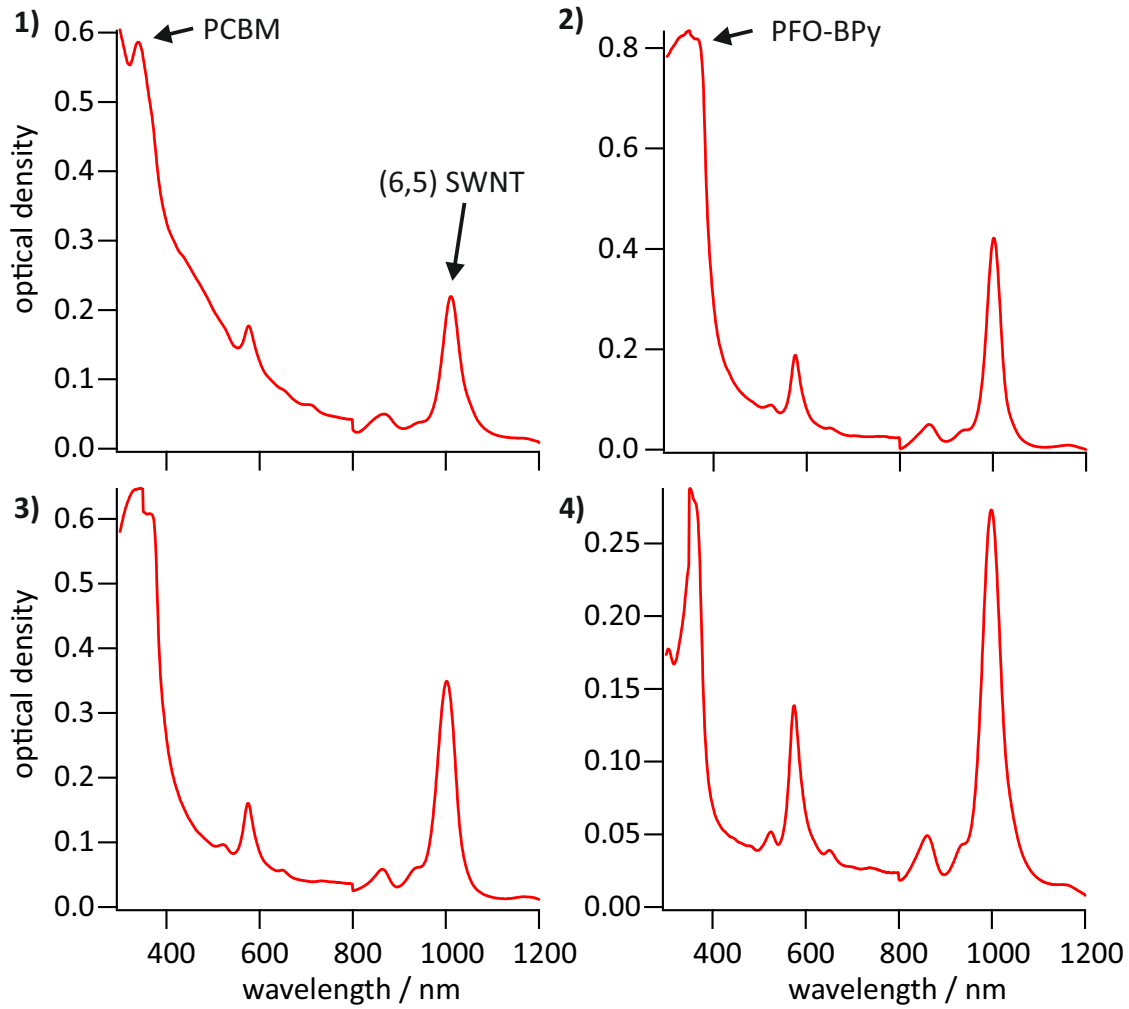

Figure 5.19: Absorption spectra of the four different IDE samples described in table 5.3. **1)** The high relative content of PCBM compared to the other samples produces a discernible peak at 336 nm, alongside the S_1 signal of (6,5) SWNTs at 1000 nm. **2)** The addition of PFO-BPy produces a new signal at 350 nm. The PCBM signal is not visible due to saturation of the absorption spectra in this spectral region. **3)** Similiarly to sample 2 only the PFO-BPy components are visible to the saturation of the UV region with PFO-BPy signal **4)** The final signal is pure SWNT-sample. The PFO-BPy signal at 350 nm stems mostly from PFO-PBy, that is wrapped around the (6,5), since no further polymer was added prior to drop-casting. Consequently the PFO-BPy signal is roughly equal in intensity as the SWNT absorption, which is a signficant decrease compared to the previous two samples.

5.4.1.3 Experimental aspects of the carrier motion dynamics investigation

The transient photocurrent measurements described in this section were performed by Jašinskas et al. [202]. The carrier motion was investigated using time-resolved electric-field-induced second harmonic generation (TREFISH). TREFISH is an established method for probing ultrafast carrier motion in conjugated polymers citeDevizis2009 and organic solar cells [218]. The method has been described in previous publications and will not be elaborated on in detail here [219,

220], but a brief overview of the methodology will be provided.
Electric-field-induced second harmonic generation is a third-order nonlinear process, which results from the interaction between an external electric field with two incident photons [221]. By applying an electric bias, the sample capacitance is charged. In a time-resolved experiment, an ultrashort excitation pulse induces a photocurrent inside the sample, causing a discharge of the capacitance. The subsequent probe pulse is delayed by a variable amount and thus probes the kinetics of the electric field.

The sample consists of an integrating capacitor formed by a thin film on the combs of an interdigated electrode as described in the previous section 5.4.1.2. The transient photo-current kinetics were probed by measuring the voltage drop across an integrating capacitor formed by the IDE- sample and oscilloscope capacitances connected in parallel. Excitonic transitions were pumped at 1000 nm via an parametric amplifier Topas-C (Light Conversion Ltd.) and a femtosecond Ti:Sapphire laser Integra-C from Quantronix Inc. (λ = 800 nm. τ_{pulse} = 130 fs). The voltage was recorded with an Agilent Technologies DS05054A oscilloscope with a 1 MΩ input resistance.

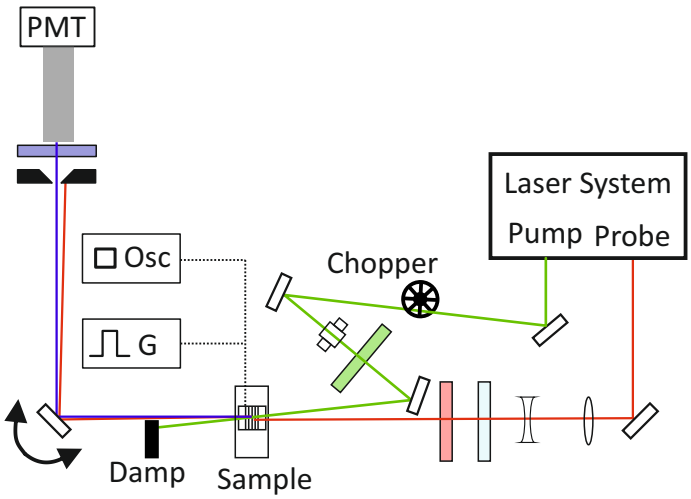

Figure 5.20: Image adapted from Jašinskas et al. [202]. Experimental setup for the carrier motion dynamic investigation. The setup can perform transient absorption spectroscopy as well as TREFISH.

The photo-current measurements were supplemented by transient absorption spectroscopy using a pump-probe spectrometer based on Pharos femtosecond laser (Light Conversion) generating pulses at 1030 nm with a duration of 250 fs at a 5 kHz repetition rate.

5.4.2 Results and discussion

Generally, the photo-conductivity of SWNT/PCBM blends stems from electron transfer from photo-excited SWNTs to adjacent PCBM molecules as free charge carriers [222, 223]. In pure SWNT films, oxygen or other defects act as electron acceptors instead [224]. However, the photocurrent in pure SWNT-films is generally dominated by hole motion within the percolated SWNT network.
In contrast to PCBM-free samples, PCBM:SWNT blend films show a long-lived signal component, which can be attributed to efficient ultrafast electron transfer from excited SWNT to PCBM and generation of free charge carriers, which prevent a complete recovery of the transient absorption signal. Transient absorption spectroscopy, under excitation at 1000 nm shows a fast recovery in a few tens of picoseconds due to exciton decay, as shown in figure 5.21. Another weaker and longer-lived component can be attributed to free charge carrier generation. Notably, this long-lived signal is much more pronounced in samples with high PCBM content, which suggests that the generation of charge carriers is more efficient in those samples.

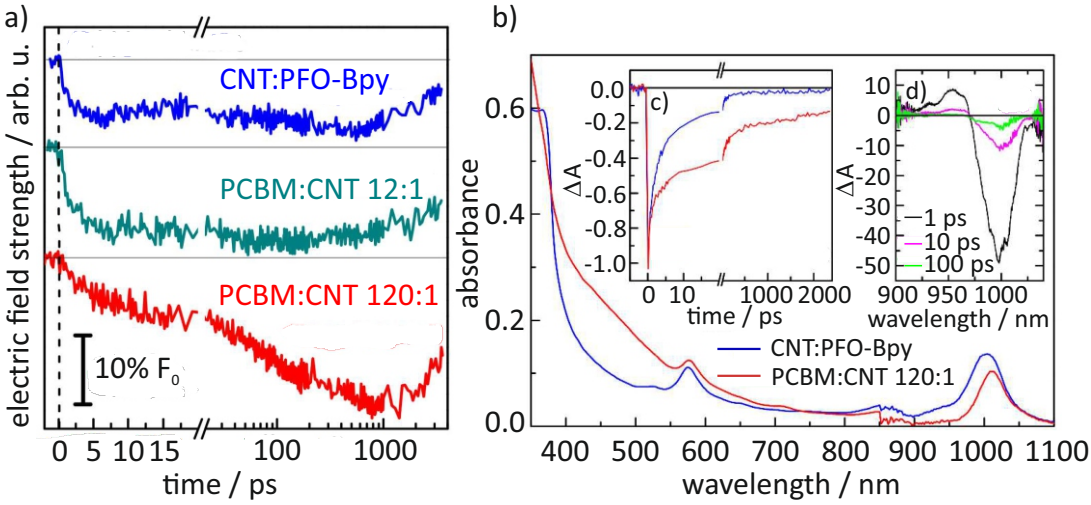

Figure 5.21: Image reproduced from Jašinskas et al. [202] a) Electric field kinetics for SWNT:PFO-Bpy (blue: sample 4) films and SWNT/PCBM blend films (green: sample 2, red: sample 1). b) Absorption spectrum of sample 1 and 4. The inset c) shows the absorption signal bleaching at 1000 nm. d) shows the transient absorption spectra at different delay times.

In samples without PCBM or low PCBM content, excitation of neutral excitons usually results in a sharp drop in the electric field strength as seen in figure 5.21 a). The field partially recovers within 5 ps to 20 ps, because of the high polarizability of neutral excitons, which increases the dielectric constant inside the material. This, in turn, decreases the electric field strength and capacity of the charged sample. At longer delay times, the current of photogenerated charge carriers seems to compensate for that effect.
High PCBM concentrations increase the carrier generation efficiency by approximately an order

of magnitude, compared to samples without PCBM [225]. Consequently, the charge carrier generation overpowers the recovery due to neutral exciton decay, leading to a further decline in electric field strength until 1000 ps. There is also no observable initial drop in samples with high PCBM concentration, suggesting that neutral excitons are either not generated or are almost immediately quenched. This would be consistent with observations made during fluorescence spectroscopy, which drops rapidly in intensity upon the introduction of defects into the sample (see section 2.1.2.2). Contact points with PCBM could similarly provide a non-radiative path of decay for excitons.
Furthermore, the absence of a fast drop in field strength also suggests low polarizability of the charge-transfer (CT) excitons between PCBM and SWNTs. This is expected due to the strong localization of electrons in the comparatively small PCBM molecules and the localization of holes on the SWNT due to Coulomb interactions. A similar effect has been reported for $AuCl_3$ doped SWNTs [10, 76].
After the initial drop, the electric field dynamics are determined by the free carrier generation and motion. In high PCBM content samples, these two processes dominate due to the negligible amount of neutral excitons. TREFISH cannot distinguish between the two, so only an upper limit for both processes of 200 ps to 1000 ps can be established.
At several nanosecond delay time the electric field recovers somewhat, which can be attributed to geminate charge recombination. This process has only been observed in transient absorption experiments. A similar recombination rate was reported for charge carriers generated at the SWNT/C_{60} interface [226].

In summary, four processes dominate the excited state in dynamics in SWNT and SWNT/PCBM blend films, as depicted in figure 5.22. a) The generation and subsequent recombination of neutral excitons in SWNTs, b) creation of a CT exciton with simultaneous creation of a free charge carrier in the SWNT c) dissociation of a neutral exciton into a CT exciton and free charge carrier and d) recombination of charge carriers and propagation through the SWNT percolated network.

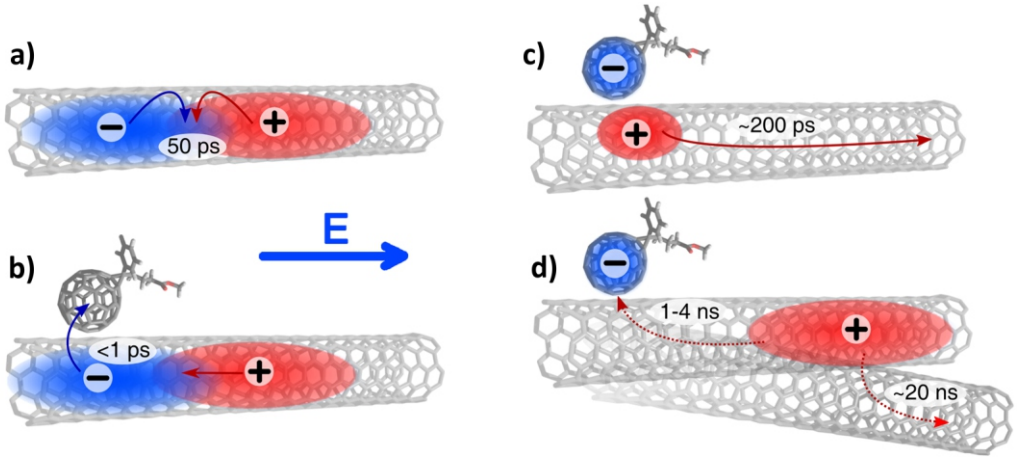

Figure 5.22: Image reproduced from Jašinskas et al. [202]. Illustration of the four different effects in excited SWNTs. a) recombination of neutral excitons in isolated SWNTs, b) charge transfer from SWNTs on PCBM, leading to localized positive charge on the SWNT, c) dissociation of the afformentioned CT state into free charge carriers, d) recombination of carriers and interchain hole transfer.

The results also indicate that 30 % to 50 % of all generated charge carriers recombine within the measurement interval of 3.6 ns.

5.5 Summary

In this chapter, several different measurement series have been presented, which all aimed to investigate the behaviour of charge carriers in SWNTs.
Firstly, the changes in relative resistivity with increasing doping levels were quantified. SWNT thin films were produced via filtration and transferred on ITO interdigitated electrodes. The films were pre-treated with benzene-viologen to remove any intrinsic p-doping. Then the samples were doped by submerging them into $AuCl_3$ in toluene/acetonitrile solutions. Absorption spectra and the resistance between the two IDE electrodes were recorded. The initial doping step drastically reduces the resistance of the thin film. Afterwards, the resistance decreases double-logarithmically with increasing dopant concentration. The initial drop-off might be due to a decrease in contact resistance between the tubes, although this could not be determined in this thesis.
Next, charge carrier concentrations of SWNTs in suspension were quantified using EPR spectroscopy. The EPR measurements were performed by our cooperation partners Michael Auth

and Andreas Sperlich from the Dyakonov Group (Experimental Physics VI, Julius-Maximilians-Universität, Würzburg). The sample preparation and absorption spectroscopy were the subject of this thesis. The SWNT suspensions were doped by adding $AuCl_3$ solution to the suspension. Parallel to the EPR series, absorption spectra were recorded under the same conditions. Charge densities as obtained from absorption spectra by band-filling and confinement models were compared with direct observations from EPR. The EPR experiments produced strong evidence for localized charge carriers. At first, the observed spin densities matched the values predicted by the models mentioned earlier. At higher doping levels the measurable spin densities starts to decline, which starkly deviates from the continuously increasing charge carrier density. This is attributed to interactions between neighbouring spins, making them effectively invisible to EPR spectroscopy.
Furthermore, a series of Raman spectra of $AuCl_3$ doped SWNT suspensions were taken. Just like the EPR series, absorption spectra were recorded in parallel. The intensity of the G^+ band was expected to decrease with falling oscillator strength in the absorption at 568 nm, which is the laser excitation wavelength. The loss of the resonance condition of incoming and outgoing photons should substantially decrease the observed Raman intensity. However, the actual trend deviates in two ways: Firstly, the initial doping step causes a much steeper decrease in Raman intensity than all remaining steps, similar to the resistance measurements in secion 5.1. Secondly, even after the initial drop-off, the Raman intensity decreases slightly faster than a loss of resonance would explain. Therefore another yet unknown factor impacts the Raman intensity of doped SWNTs, possibly a decrease in exciton lifetime.
Finally, the charge-transfer characteristics between SWNTs and PCBM have been investigated. The sample preparation, absorption spectra and initial resistance measurements were performed by our group. The TREFISH and transient absorption measurements were performed by our co-operation partner Jašinskas et al. from the V. Gulbinas group (Center for Physical Sciences and Technology, Vilnius, Lithuania). The samples were produced via drop-casting blends of SWNT suspensions and PCBM solutions. The resistance and absorption spectra of each sample were measured to ensure that it meets the specification of Jašinskas et al. [202]. The composition of these samples was optimized to distinguish between different charge transport mechanisms as easily as possible. The measurements showed that there are four mechanisms that can occur after photo-excitation: the recombination of neutral excitons (< 50 ps), the electron transfer from carbon nanotubes to PCBM molecules (< 1 ps), the decay of charge-transfer excitons (≈200 ps), the recombination of charge carriers between charge-transfer excitons (1 ns to 4 ns) and finally, the propagation through the SWNT network (≈20 ns).

6 Summary

This thesis includes measurements that were recorded by cooperation partners. The EPR spectrosa mentioned in section 5.2 were recorded by Michael Auth from the Dyakonov Group (Experimental Physics VI, Julius-Maximilians-Universität, Würzburg). The TREFISH experiments and transient absorption in section 5.4 spectra were performed by Jašinskas et al. from the V. Gulbinas group (Center for Physical Sciences and Technology, Vilnius, Lithuania).

This dissertation investigated the interactions of semiconducting single-walled carbon nanotubes (SWNTs) of (6,5) chirality with their environment. Shear-mixing provided high-quality SWNT suspensions, which was complemented by various film preparation techniques. These techniques were in turn used to prepare heterostructures with MoS_2 and hBN, which were examined with a newly constructed photoluminescence microscope specifically for this purpose. Finally, the change of spectral properties of SWNTs upon doping was investigated in more detail, as well as the behaviour of charge carriers in the tubes themselves.

To optimise the SWNT sample preparation techniques that supplied the other experiments, the sample quality of shear-mixed preparations was compared with that of sonicated samples. It was found that the quantum efficiency of sheared suspensions exceeds that of sonicated suspensions as soon as the sonication time exceeds 30 min. The higher PLQY is due to the lower defect concentration in shear-mixed samples. Via transient absorption, a mean lifetime of 17.3 ps and a mean distance between defects of 192.1 nm could be determined. Furthermore, it was found that the increased efficiency of horn sonication is probably not only due to higher shear forces acting on the SWNT bundles but also that the shortening of PFO-BPy strands plays a significant role. Sonication of very long polymer strands significantly increased their effectiveness in shear mixing. While previous approaches could only achieve very low concentrations of SWNTs in suspensions, pre-sonicated polymer yielded results which were comparable with much shorter PFO-BPy batches. Reference experiments also showed that different aggregation processes are relevant during production and further processing. Initial reprocessing of carbon nanotube raw material requires 7 h sonication time and over 24 h shear mixing before no increase in carbon nano concentration is detectable. However, only a few minutes of sonication or shear mixing are required when reprocessing the residue produced during the separation of the slurry. This discrepancy indicates that different aggregates are present, with markedly different aggregation properties.

To study low-dimensional heterostructures, a PL microscope was set up with the ability to observe single SWNTs as well as monolayers of other low-dimensional systems. Furthermore, samples were prepared which bring single SWNTs into contact with 2D materials such as h-BN and

MoS_2 layers and the changes in the photoluminescence spectrum were documented. For h-BN, it was observed whether previous methods for depositing SWNTs could be transferred for photoluminescence spectroscopy. SWNTs were successfully deposited on monolayers via a modified drip coating, with the limitation that SWNTs aggregate more at the edges of the monolayers.
Upon contact of SWNTs with MoS_2, significant changes in the emission properties of the monolayers were observed. The fluorescence, which was mainly dominated by excitons, was shifted towards trion emission. Reference experiments excluded PFO-BPy and toluene as potential causes. Based on the change in the emission behaviour of MoS_2, the most plausible explanation is a photoinduced charge transfer leading to delocalised charge carriers on MoS_2. In contrast, on SWNTs, the introduction of additional charges would constitute a quenching centre, which would quench their PL emission, making them undetectable in the PL image.

In the last chapter, the electronic properties of doped SWNTs and the behaviour of charge carriers inside the tubes should be investigated.
First, the change in the conductivity of SWNT films with increasing doping levels was documented. The resistance of the films drops drastically at minimum doping. After the initial introduction of charges, the resistance drops with increasing dopant concentration according to a double logarithmic curve. The initial drop could be due to a reduction of contact resistances within the SWNT network film, but this could not be further investigated within the scope of this PhD thesis.
In cooperation with Andreas Sperlich and Michael Auth, the spin concentration of SWNTs at different doping levels was determined. The obtained concentrations were compared with the carrier concentrations determined from PL and absorption spectra. At low spin densities, good agreement with previous models was found. Furthermore, the presence of isolated spins strongly suggests a localised charge carrier distribution at temperatures around 10 K. When the charge density is increased, the spin density deviates significantly from the charge carrier concentration. This discrepancy is attributed to the increasing delocalisation of charge carriers at high charge densities and the interactions of neighbouring spins. These results strongly indicate the existence of localised charge carriers in SWNTs at low temperatures.
Next, the effect of doping on the Raman spectra of SWNT suspensions was investigated. In general, doping is expected to reduce the intensity of the Raman bands, i.e. a consequence of the reduced resonance gain due to bleaching of the S_2 transition. However, similar to the resistivity measurements, the oscillator strength of the G^+ band drops sharply in the first doping steps. It was also found that the G^+ band decreases more than would be expected due to loss of resonance condition. Furthermore, the G^- is bleached faster than the G^+ band. All these anomalies suggest that resonance enhancement is not the only relevant effect. Another much faster deactivation path for the excitons may be introduced by doping. This would leave less time for the scattering process to occur and reduce the oscillator strength of the Raman bands.
In cooperation with Vidmantas et al., the photoinduced charge carrier behaviour of SWNT/PCBM films was investigated. The required films were prepared by drop coating. The SWNT suspensions required for this were obtained from sheared SWNT preparations. Using transient absorption and TREFISH, a number of charge transfer effects were identified and their dynamics investigated: the recombination of neutral excitons (< 50 ps), the electron transfer from carbon nanotubes to PCBM molecules (< 1 ps), the decay of charge-transfer excitons ($\sim$200 ps), the recombination of charge carriers between charge-transfer excitons (1 ns to 4 ns) and finally the

propagation through the SWNT network ($\sim$20 ns)

7 Zusammenfassung

Diese Arbeit beinhaltet Messungen, die von Kooperationspartnern durchgeführt wurden. Die in Abschnitt 5.2 erwähnten EPR-Spektren wurden von Michael Auth aufgenommen. Die TREFISH-Experimente und die transiente Absorption im Abschnitt 5.4-Spektren wurden von Jašinskas et al. durchgeführt.

Im Rahmen dieser Dissertation wurden die Wechselwirkungen von halbleitenden, einwandigen Kohlenstoffnanoröhren (SWNTs) der (6,5) Chiralität mit ihrer Umgebung untersucht. Dies wurde durch Einsatz von Schermischen als Präparationsmethode, sowie einer Reihe von Filmpräparationstechniken ermöglicht. Diese Techniken wurden wiederum eingesetzt, um Heterostrukturen mit MoS_2 und hBN herzustellen, welche mit einem eigens dafür aufgebauten Photolumineszenzmikroskop untersucht wurden. Schlussendlich wurde die Änderung der spektralen Eigenschaften von SWNTs bei Dotierung näher untersucht, ebenso wie das Verhalten von Ladungsträgern in den Röhren selbst. Die EPR Spektren die im Abschnitt 5.2 aufgeführt sind wurden von Michael Auth aufgenommen. Die TREFISH Experimente und die dazugehörigen transienten Absorptions Spektren wurde von Jašinskas et al. durchgeführt.

Für die Herstellung der benötigten SWNT-Proben wurde die Probenqualität von geschermischten Ansätzen mit deren von beschallten Proben verglichen. Dabei wurde festgestellt, dass die Quanteneffizienz von geschermischten die von beschallten deutlich übersteigt, sobald die Beschallungszeit 30 min überschreitet. Dies ist auf die geringere Defektkonzentration in geschermischten Proben zurückzuführen. Über transiente Absorption konnte eine mittlere Lebensdauer von 17.3 ps und ein mittlerer Abstand zwischen Defekten von 192.1 nm bestimmt werden. Ferner wurde festgestellt, dass die erhöhte Effizienz von Horn-Beschallung wahrscheinlich nicht nur auf höhere Scherwirkung an den SWNT-Bündeln liegt, sondern auch die Verkürzung von PFO-BPy Strängen eine erhebliche Rolle spielt. Die Beschallung von sehr langen Polymer-Strängen hat deren Effektivität bei Schermischen deutlich erhöht. Während bei vorherigen Ansätzen nur sehr geringe Konzentration an SWNTs in Suspensionen erreicht werden könnten, konnte mit vor-beschallten Polymer vergleichbare Ergebnisse wie mit wesentlich kürzeren PFO-BPy Chargen erreicht werden. Referenzexperimente zeigten außerdem, dass verschiedene Aggregationsprozesse bei der Herstellung und Weiterverarbeitung relevant sind. Bei der initialen Aufarbeitung von Kohlenstoffnanorohr Rohmaterial sind 7 h Beschallungszeit und über 24 h Schermischen erforderlich, bevor keine Erhöhung der Kohlenstoffnano-Konzentration mehr feststellbar ist. Bei Wiederaufarbeitung des bei der Abtrennung des Suspension entstandenen Rückstands sind allerdings nur wenige Minuten Beschallung oder Schermischen notwendig. Dies deutet

darauf hin, dass grundlegend unterschiedliche Aggregate vorliegen, mit deutlich anderen Aggregationseigenschaften.

Um nieder-dimensionale Heterostrukturen zu untersuchen wurde ein PLE-Mikroskop aufgebaut, mit der Fähigkeit einzelne SWNTs, sowie Monolagen andere nieder-dimensionale Systeme zu untersuchen. Weiterhin wurde Proben hergestellt welche einzelne SWNTs mit 2D-Materialien wie h-BN und MoS_2 Schichten in Kontakt bringen und der Änderungen im Photolumineszenz Spektrum dokumentiert. Für h-BN wurde beobachtet, ob bisherige Methoden zur Ablagerung von SWNTs für Photolumineszenz-Spektroskopie übertragen werden können. Dabei wurde beobachtet, dass über eine modifizierte Tropfbeschichtung SWNTs auf Monolagen abgelagert werden können, mit der Einschränkung, dass an den Kanten der Monolagen SWNT verstärkt aggregieren.
Bei Kontakt von SWNTs mit MoS_2 wurden erhebliche Änderungen in den Emissionseigenschaften der Monolagen beobachtet. Die hauptsächlich von Exzitonen dominierte Fluoreszenz wurde hin zu Trion-Emission verschoben. Referenzexperimente schlossen PFO-BPy und Toluol als potenzielle Ursachen aus. Basierend auf der Änderung des Emissionsverhaltens von MoS_2, ist die plausibelste Erklärung ein photoinduzierter Ladungstransfer, welcher zu delokalisierten Ladungsträgern auf MoS_2 führt. Hingegen auf SWNTs würde die Einführung zusätzlicher Ladungen ein Löschzentrum darstellen, was deren PL Emission weitestgehend unterdrücken würde.

Im letzten Kapitel sollten die elektronischen Eigenschaften von dotierten SWNTs und das Verhalten von Ladungsträgern innerhalb der Röhren untersucht werden.
Zunächst wurden die Veränderung in der Leitfähigkeit von SWNT-Filmen bei zunehmenden Dotierungsgrad dokumentiert. Dabei wurde beobachtet, dass der Widerstand der Filme bei minimaler Dotierung drastisch abfällt. Nach dem ersten Einbringen von Ladungen fällt der Widerstand mit steigender Dotiermittelkonzentration gemäß eines doppel-logarithmischen Verlaufs. Der initiale Abfall könnte an einer Verringerung von Kontaktwiderständen innerhalb des SWNT-Netzwerk-Films liegen, allerdings konnte dies nicht in Rahmen dieser Doktorarbeit geklärt werden.
Im Rahmen einer Kooperation mit Andreas Sperlich und Michael Auth wurde dabei die Spinkonzentration von SWNTs bei verschiedene Dotierungsgraden untersucht. Die erhaltenen Konzentrationen wurden mit den Ladungsträger-Konzentration, die aus PL und Absorptionsspektren bestimmt wurden, verglichen. Bei niedrigen Spin-Dichten zeigte sich eine gute Übereinstimmung mit bisherigen Modellen. Ferner, deutet die Präsenz von isolierten Spins stark auf eine lokalisierte Ladungsträger-Verteilung bei Temperaturen um 10 K hin. Bei Erhöhung der Ladungsdichte weicht die Spindichte erheblich von der Ladungsträger-Konzentration. Diese Diskrepanz wird auf die zunehmende Delokalisierung der Ladungsträger bei hohen Ladungsdichten zurückgeführt. Delokalisierte Spins sind nicht detektierbar in EPR Methoden. Diese Resultate sind ein starkes Indiz für das Vorhandensein von lokalisierten Ladungsträgern in SWNTs bei niedrigen Temperaturen.
Als Nächstes wurde der Effekt von Dotierung auf die Raman Spektren von SWNT Suspensionen untersucht. Generell wird erwartet, dass Dotierung die Intensität der Raman-Banden verringert, also Folge der verringerten Resonanzverstärkung durch Bleichen des S_2 Übergangs. Allerdings wurde ähnlich wie bei den Widerstandsmessungen ein starker Abfall in der Oszillatorstärke der G^+-Bande bei den ersten Dotierungsschritten festgestellt. Weiterhin wurde festgestellt, dass die G^+ Band stärker abnimmt, als durch Verlust der Resonanzbedingung zu erwarten wäre. Außerdem wird die G^- stärker gebleicht als die G^+ Bande. All diese Anomalien deuten darauf hin, dass die Resonanzverstärkung nicht der einzige relevante Effekt ist. Möglicherweise spielt eine

beschleunigte Deaktivierung der Exzitonen über durch Dotierung eingebrachte Defekte eine entscheidende Rolle.
In Kooperation mit der Gruppe um Vidmantas et al. wurde das photoinduzierte Ladungsträger-Verhalten von SWNT/PCBM Filmen untersucht. Die dazu benötigten Filme wurden über Tropfbeschichtung hergestellt. Die dazu notwendingen SWNT-Suspensionen stammen aus geschermischten SWNT-Ansätzen. Über transiente Absorption und TREFISH konnten eine Reihe von Ladungstransfer-Effekten identifiziert un deren Dynamik untersucht werden: die Rekombination von neutralen Exzitonen (50 ps, den Elektronentransfer von Kohlenstoffnanoröhren auf PCBM Moleküle ($<$ 1 ps), den Zerfall von Ladungstransfer-Exzitonen ($\sim$200 ps), die Rekombination von Ladungsträgern zwischen Ladungstransfer-Exzitonen (1 ns to 4 ns) und schließlich die Propagation durch das SWNT-Netzwerk ($\sim$20 ns))

Bibliography

[1] J. C. Meyer, A. K. Geim, M. I. Katsnelson, K. S. Novoselov, T. J. Booth, S. Roth, *Nature* **2007**, *446*, 60–63, DOI 10.1038/nature05545.

[2] https://www.nobelprize.org/prizes/physics/2010/summary/.

[3] Y. Cao, J. M. Park, K. Watanabe, T. Taniguchi, P. Jarillo-Herrero, *Nature* **2021**, *595*, 526–531, DOI 10.1038/s41586-021-03685-y.

[4] M. M. Shulaker, G. Hills, R. S. Park, R. T. Howe, K. Saraswat, H.-S. P. Wong, S. Mitra, *Nature* **2017**, *547*, 74–78, DOI 10.1038/nature22994.

[5] A. D. Franklin, M. Luisier, S.-J. Han, G. Tulevski, C. M. Breslin, L. Gignac, M. S. Lundstrom, W. Haensch, *Nano letters* **2012**, *12*, 758–762, DOI 10.1021/nl203701g.

[6] G. J. Brady, A. J. Way, N. S. Safron, H. T. Evensen, P. Gopalan, M. S. Arnold, *Science advances* **2016**, *2*, e1601240, DOI 10.1126/sciadv.1601240.

[7] Q. H. Wang, K. Kalantar-Zadeh, A. Kis, J. N. Coleman, M. S. Strano, *Nature Nanotechnology* **2012**, *7*, 699–712, DOI 10.1038/nnano.2012.193.

[8] M. Yankowitz, J. Xue, D. Cormode, J. D. Sanchez-Yamagishi, K. Watanabe, T. Taniguchi, P. Jarillo-Herrero, P. Jacquod, B. J. LeRoy, *Nature Physics* **2012**, *8*, 382–386, DOI 10.1038/nphys2272.

[9] C. Dean, A. F. Young, L. Wang, I. Meric, G.-H. Lee, K. Watanabe, T. Taniguchi, K. Shepard, P. Kim, J. Hone, *Solid State Communications* **2012**, *152*, 1275–1282, DOI 10.1016/j.ssc.2012.04.021.

[10] S. M. Kim, K. K. Kim, Y. W. Jo, M. H. Park, S. J. Chae, D. L. Duong, C. W. Yang, J. Kong, Y. H. Lee, *ACS nano* **2011**, *5*, 1236–1242, DOI 10.1021/nn1028532.

[11] F. Li, H. M. Cheng, S. Bai, G. Su, M. S. Dresselhaus, *Applied Physics Letters* **2000**, *77*, 3161–3163, DOI 10.1063/1.1324984.

[12] R. Saito, M. Fujita, G. Dresselhaus, M. S. Dresselhaus, *Applied Physics Letters* **1992**, *60*, 2204–2206, DOI 10.1063/1.107080.

[13] M. S. Dresselhaus, G. Dresselhaus, R. Saito, *Carbon* **1995**, *33*, 883–891, DOI 10.1016/0008-6223(95)00017-8.

[14] M. S. Dresselhaus, G. Dresselhaus, R. Saito, A. Jorio, *Physics Reports* **2005**, *409*, 47–99, DOI 10.1016/j.physrep.2004.10.006.

[15] R. Saito, G. Dresselhaus, M. S. Dresselhaus, *Physical properties of carbon nanotubes*, Imperial College Press, London, **1998**.

[16] S. N. Kim, Z. Kuang, J. G. Grote, B. L. Farmer, R. R. Naik, *Nano letters* **2008**, *8*, 4415–4420, DOI 10.1021/nl802332v.

[17] S. Iijima, *Physica B: Condensed Matter* **2002**, *323*, 1–5, DOI 10.1016/S0921-4526(02)00869-4.

[18] R. B. Weisman, J. Kono in *Handbook of Carbon Nano Materials*, (Eds.: F. D'Souza, K. M. Kadish), World Scientific Series on Carbon Nanoscience, World Scientific, **2012**, pp. 1–43, DOI 10.1142/9789813235465{\textunderscore}0001.

[19] Leon Van Hove, L. van Hove, *Physical Review* **1953**, *89*, 1189–1193, DOI 10.1103/PhysRev.89.1189.

[20] T. Ando, *Journal of the Physical Society of Japan* **1997**, 1066–1073.

[21] J. Lefebvre, P. Finnie, *Nano letters* **2008**, *8*, 1890–1895, DOI 10.1021/nl080518h.

[22] H. Hartleb, F. Spath, T. Hertel, *ACS nano* **2015**, *9*, 10461–10470, DOI 10.1021/acsnano.5b04707.

[23] F. Wang, G. Dukovic, L. E. Brus, T. F. Heinz, *Science (New York N.Y.)* **2005**, *308*, 838–841, DOI 10.1126/science.1110265.

[24] J. Maultzsch, R. Pomraenke, S. Reich, E. Chang, D. Prezzi, A. Ruini, E. Molinari, M. S. Strano, C. Thomsen, C. Lienau, *physica status solidi (b)* **2006**, *243*, 3204–3208, DOI 10.1002/pssb.200669131.

[25] M. A. Green, *AIP Advances* **2013**, *3*, 112104, DOI 10.1063/1.4828730.

[26] D. M. Guldi, N. Martín, *Carbon Nanotubes and Related Structures*, Wiley, **2010**, DOI 10.1002/9783527629930.

[27] C. D. Spataru, S. Ismail-Beigi, R. B. Capaz, S. G. Louie, *Physical review letters* **2005**, *95*, 247402, DOI 10.1103/PhysRevLett.95.247402.

[28] T. Ando, *Journal of the Physics Society Japan* **2006**, *75*, 024707, DOI 10.1143/JPSJ.75.024707.

[29] C. D. Spataru, S. Ismail-Beigi, L. X. Benedict, S. G. Louie, *Physical review letters* **2004**, *92*, 077402, DOI 10.1103/PhysRevLett.92.077402.

[30] V. Perebeinos, J. Tersoff, P. Avouris, *Physical review letters* **2004**, *92*, 257402, DOI 10.1103/PhysRevLett.92.257402.

[31] E. Chang, G. Bussi, A. Ruini, E. Molinari, *Physical review letters* **2004**, *92*, 196401, DOI 10.1103/PhysRevLett.92.196401.

[32] H. Zhao, S. Mazumdar, *Physical review letters* **2004**, *93*, 157402, DOI 10.1103/PhysRevLett.93.157402.

[33] H. Zhao, S. Mazumdar, C.-X. Sheng, M. Tong, Z. V. Vardeny, *Physical Review B* **2006**, *73*, DOI 10.1103/PhysRevB.73.075403.

[34] I. B. Mortimer, R. J. Nicholas, *Physical review letters* **2007**, *98*, 027404, DOI 10.1103/PhysRevLett.98.027404.

[35] E. B. Barros, R. B. Capaz, A. Jorio, G. G. Samsonidze, A. G. Souza Filho, S. Ismail-Beigi, C. D. Spataru, S. G. Louie, G. Dresselhaus, M. S. Dresselhaus, *Physical Review B* **2006**, *73*, DOI 10.1103/PhysRevB.73.241406.

[36] R. Matsunaga, K. Matsuda, Y. Kanemitsu, *Physical review letters* **2011**, *106*, 037404, DOI 10.1103/PhysRevLett.106.037404.

[37] J. S. Park, Y. Hirana, S. Mouri, Y. Miyauchi, N. Nakashima, K. Matsuda, *Journal of the American Chemical Society* **2012**, *134*, 14461–14466, DOI 10.1021/ja304282j.

[38] M. A. Lampert, *Physical review letters* **1958**, *1*, 450–453, DOI 10.1103/PhysRevLett.1.450.

[39] R. T. Cox, R. B. Miller, K. Saminadayar, T. Baron, *Physical Review B* **2004**, *69*, DOI 10.1103/PhysRevB.69.235303.

[40] T. F. Rønnow, T. G. Pedersen, H. D. Cornean, *Physics Letters A* **2009**, *373*, 1478–1481, DOI 10.1016/j.physleta.2009.02.049.

[41] T. F. Rønnow, T. G. Pedersen, H. D. Cornean, *Physical Review B* **2010**, *81*, DOI 10.1103/PhysRevB.81.205446.

[42] S. M. Santos, B. Yuma, S. Berciaud, J. Shaver, M. Gallart, P. Gilliot, L. Cognet, B. Lounis, *Physical review letters* **2011**, *107*, 187401, DOI 10.1103/PhysRevLett.107.187401.

[43] M. J. O'Connell, S. M. Bachilo, C. B. Huffman, V. C. Moore, M. S. Strano, E. H. Haroz, K. L. Rialon, P. J. Boul, W. H. Noon, C. Kittrell, J. Ma, R. H. Hauge, R. B. Weisman, R. E. Smalley, *Science (New York N.Y.)* **2002**, *297*, 593–596, DOI 10.1126/science.1072631.

[44] P. J. F. Harris, *Carbon nanotubes and related structures: New materials for the twenty-first century*, Repr, Cambridge University Press, Cambridge, **2004**, DOI 10.1017/CBO9780511605819

[45] C. Manzoni, A. Gambetta, E. Menna, M. Meneghetti, G. Lanzani, G. Cerullo, *Physical review letters* **2005**, *94*, 207401, DOI 10.1103/PhysRevLett.94.207401.

[46] T. Hertel, V. Perebeinos, J. Crochet, K. Arnold, M. Kappes, P. Avouris, *Nano letters* **2008**, *8*, 87–91, DOI 10.1021/nl0720915.

[47] L. Lüer, J. Crochet, T. Hertel, G. Cerullo, G. Lanzani, *ACS nano* **2010**, *4*, 4265–4273, DOI 10.1021/nn100674h.

[48] F. Wang, G. Dukovic, L. E. Brus, T. F. Heinz, *Physical review letters* **2004**, *92*, 177401, DOI 10.1103/PhysRevLett.92.177401.

[49] A. Hagen, M. Steiner, M. B. Raschke, C. Lienau, T. Hertel, H. Qian, A. J. Meixner, A. Hartschuh, *Physical review letters* **2005**, *95*, 197401, DOI 10.1103/PhysRevLett.95.197401.

[50] H. Hirori, K. Matsuda, Y. Miyauchi, S. Maruyama, Y. Kanemitsu, *Physical review letters* **2006**, *97*, 257401, DOI 10.1103/PhysRevLett.97.257401.

[51] C. Voisin, S. Berger, S. Berciaud, H. Yan, J.-S. Lauret, G. Cassabois, P. Roussignol, J. Hone, T. F. Heinz, *physica status solidi (b)* **2012**, *249*, 900–906, DOI 10.1002/pssb.201100085.

[52] S. Berciaud, L. Cognet, B. Lounis, *Physical review letters* **2008**, *101*, 077402, DOI 10.1103/PhysRevLett.101.077402.

[53] A. Graf, L. Tropf, Y. Zakharko, J. Zaumseil, M. C. Gather, *Nature communications* **2016**, *7*, 13078, DOI 10.1038/ncomms13078.

[54] T. Hertel, S. Himmelein, T. Ackermann, D. Stich, J. Crochet, *ACS nano* **2010**, *4*, 7161–7168, DOI 10.1021/nn101612b.

[55] J. Crochet, M. Clemens, T. Hertel, *Journal of the American Chemical Society* **2007**, *129*, 8058–8059, DOI 10.1021/ja071553d.

[56] L. J. Carlson, S. E. Maccagnano, M. Zheng, J. Silcox, T. D. Krauss, *Nano letters* **2007**, *7*, 3698–3703, DOI 10.1021/nl072014.

[57] X. Wei, T. Tanaka, S. Li, M. Tsuzuki, G. Wang, Z. Yao, L. Li, Y. Yomogida, A. Hirano, H. Liu, H. Kataura, *Nano letters* **2020**, *20*, 410–417, DOI 10.1021/acs.nanolett.9b04095.

[58] R. Kawabe, H. Takaki, T. Ibi, Y. Maeda, K. Nakagawa, H. Maki, *ACS Applied Nano Materials* **2020**, *3*, 682–690, DOI 10.1021/acsanm.9b02209.

[59] D. R. McCulley, M. J. Senger, A. Bertoni, V. Perebeinos, E. D. Minot, *Nano letters* **2020**, *20*, 433–440, DOI 10.1021/acs.nanolett.9b04151.

[60] M. Gao, H. Liu, S. Yu, S. Louisia, Y. Zhang, D. P. Nenon, A. P. Alivisatos, P. Yang, *Journal of the American Chemical Society* **2020**, *142*, 8871–8879, DOI 10.1021/jacs.0c02000.

[61] J. T. Flach, J. Wang, M. S. Arnold, M. T. Zanni, *The journal of physical chemistry letters* **2020**, *11*, 6016–6024, DOI 10.1021/acs.jpclett.0c01555.

[62] B. J. Gifford, S. Kilina, H. Htoon, S. K. Doorn, S. Tretiak, *Accounts of chemical research* **2020**, *53*, 1791–1801, DOI 10.1021/acs.accounts.0c00210.

[63] V. Perebeinos, P. Avouris, *Physical review letters* **2008**, *101*, 057401, DOI 10.1103/PhysRevLett.101.057401.

[64] S. Mouri, Y. Miyauchi, K. Matsuda, *Nano letters* **2013**, *13*, 5944–5948, DOI 10.1021/nl403036h.

[65] Y. Miyauchi, H. Hirori, K. Matsuda, Y. Kanemitsu, *Physical Review B* **2009**, *80*, DOI 10.1103/PhysRevB.80.081410.

[66] Y. Miyauchi, K. Matsuda, Y. Yamamoto, N. Nakashima, Y. Kanemitsu, *The Journal of Physical Chemistry C* **2010**, *114*, 12905–12908, DOI 10.1021/jp1027492.

[67] T. Liu, Z. Xiao, *The Journal of Physical Chemistry C* **2011**, *115*, 16920–16927, DOI 10.1021/jp205458t.

[68] J. Wang, M. J. Shea, J. T. Flach, T. J. McDonough, A. J. Way, M. T. Zanni, M. S. Arnold, *The Journal of Physical Chemistry C* **2017**, *121*, 8310–8318, DOI 10.1021/acs.jpcc.7b01005.

[69] L. Cognet, D. A. Tsyboulski, J.-D. R. Rocha, C. D. Doyle, J. M. Tour, R. B. Weisman, *Science (New York N.Y.)* **2007**, *316*, 1465–1468, DOI 10.1126/science.1141316.

[70] L. Lüer, S. Hoseinkhani, D. Polli, J. Crochet, T. Hertel, G. Lanzani, *Nature Physics* **2009**, *5*, 54–58, DOI 10.1038/nphys1149.

[71] C. Georgi, A. A. Green, M. C. Hersam, A. Hartschuh, *ACS nano* **2010**, *4*, 5914–5920, DOI 10.1021/nn101443d.

[72] S. Moritsubo, T. Murai, T. Shimada, Y. Murakami, S. Chiashi, S. Maruyama, Y. K. Kato, *Physical review letters* **2010**, *104*, 247402, DOI 10.1103/PhysRevLett.104.247402.

[73] I. Heller, J. Kong, K. A. Williams, C. Dekker, S. G. Lemay, *Journal of the American Chemical Society* **2006**, *128*, 7353–7359, DOI 10.1021/ja061212k.

[74] Y. Miyauchi, H. Ajiki, S. Maruyama, *Physical Review B* **2010**, *81*, DOI 10.1103/PhysRevB.81.121415.

[75] T. F. Rønnow, T. G. Pedersen, B. Partoens, K. K. Berthelsen, *Physical Review B* **2011**, *84*, DOI 10.1103/PhysRevB.84.035316.

[76] K. H. Eckstein, H. Hartleb, M. M. Achsnich, F. Schöppler, T. Hertel, *ACS nano* **2017**, DOI 10.1021/acsnano.7b05543.

[77] H. Haug, S. W. Koch, *Quantum theory of the optical and electronic properties of semiconductors*, Fifth edition, World Scientific, Hackensack, NJ, **2009**.

[78] Ogawa, Takagahara, *Physical review. B Condensed matter* **1991**, *44*, 8138–8156, DOI 10.1103/physrevb.44.8138.

[79] E. Malic, J. Maultzsch, S. Reich, A. Knorr, *Physical Review B* **2010**, *82*, DOI 10.1103/PhysRevB.82.035433.

[80] V. Perebeinos, J. Tersoff, P. Avouris, *Physical review letters* **2005**, *94*, 027402, DOI 10.1103/PhysRevLett.94.027402.

[81] O. N. Torrens, M. Zheng, J. M. Kikkawa, *Physical review letters* **2008**, *101*, 157401, DOI 10.1103/PhysRevLett.101.157401.

[82] P. M. Vora, X. Tu, E. J. Mele, M. Zheng, J. M. Kikkawa, *Physical Review B* **2010**, *81*, DOI 10.1103/PhysRevB.81.155123.

[83] N. Akizuki, M. Iwamura, S. Mouri, Y. Miyauchi, T. Kawasaki, H. Watanabe, T. Suemoto, K. Watanabe, K. Asano, K. Matsuda, *Physical Review B* **2014**, *89*, DOI 10.1103/PhysRevB.89.195432.

[84] Kheng, Cox, M. Y. d'Aubigné, Bassani, Saminadayar, Tatarenko, *Physical review letters* **1993**, *71*, 1752–1755, DOI 10.1103/PhysRevLett.71.1752.

[85] B. Yuma, S. Berciaud, J. Besbas, J. Shaver, S. Santos, S. Ghosh, R. B. Weisman, L. Cognet, M. Gallart, M. Ziegler, B. Hönerlage, B. Lounis, P. Gilliot, *Physical Review B* **2013**, *87*, DOI 10.1103/PhysRevB.87.205412.

[86] M. Yoshida, A. Popert, Y. K. Kato, *Physical Review B* **2016**, *93*, DOI 10.1103/PhysRevB.93.041402.

[87] T. Koyama, S. Shimizu, Y. Miyata, H. Shinohara, A. Nakamura, *Physical Review B* **2013**, *87*, DOI 10.1103/PhysRevB.87.165430.

[88] T. Nishihara, Y. Yamada, Y. Kanemitsu, *Physical Review B* **2012**, *86*, DOI 10.1103/PhysRevB.86.075449.

[89] Y. Kimoto, M. Okano, Y. Kanemitsu, *Physical Review B* **2013**, *87*, DOI 10.1103/PhysRevB.87.195416.

[90] A. D. Avery, B. H. Zhou, J. Lee, E.-S. Lee, E. M. Miller, R. Ihly, D. Wesenberg, K. S. Mistry, S. L. Guillot, B. L. Zink, Y.-H. Kim, J. L. Blackburn, A. J. Ferguson, *Nature Energy* **2016**, *1*, 16033, DOI 10.1038/nenergy.2016.33.

[91] Schmitt-Rink, Chemla, Miller, *Physical review. B Condensed matter* **1985**, *32*, 6601–6609, DOI 10.1103/physrevb.32.6601.

[92] Greene, Orenstein, Millard, Williams, *Physical review letters* **1987**, *58*, 2750–2753, DOI 10.1103/PhysRevLett.58.2750.

[93] B. I. Greene, J. Orenstein, S. Schmitt-Rink, *Science (New York N.Y.)* **1990**, *247*, 679–687, DOI 10.1126/science.247.4943.679.

[94] K. H. Eckstein, F. Oberndorfer, M. M. Achsnich, F. Schöppler, T. Hertel, *The Journal of Physical Chemistry C* **2019**, *123*, 30001–30006, DOI 10.1021/ACS.JPCC.9B08663.

[95] M. S. Hofmann, J. T. Glückert, J. Noé, C. Bourjau, R. Dehmel, A. Högele, *Nature Nanotechnology* **2013**, *8*, 502–505, DOI 10.1038/nnano.2013.119.

[96] C. Mann, T. Hertel, *The journal of physical chemistry letters* **2016**, *7*, 2276–2280, DOI 10.1021/acs.jpclett.6b00797.

[97] S. Mouri, Y. Miyauchi, M. Iwamura, K. Matsuda, *Physical Review B* **2013**, *87*, DOI 10.1103/PhysRevB.87.045408.

[98] V. Perebeinos, J. Tersoff, P. Avouris, *Nano letters* **2005**, *5*, 2495–2499, DOI 10.1021/nl051828s.

[99] T. Cheiwchanchamnangij, W. R. L. Lambrecht, *Physical Review B* **2012**, *85*, DOI 10.1103/PhysRevB.85.205302.

[100] B. Spivak, S. V. Kravchenko, S. A. Kivelson, X. P. A. Gao, *Reviews of Modern Physics* **2010**, *82*, 1743–1766, DOI 10.1103/RevModPhys.82.1743.

[101] Ruckenstein, Schmitt-Rink, *Physical review. B Condensed matter* **1987**, *35*, 7551–7557, DOI 10.1103/physrevb.35.7551.

[102] Hawrylak, *Physical review. B Condensed matter* **1991**, *44*, 3821–3828, DOI 10.1103/physrevb.44.3821.

[103] B. A. Ruzicka, R. Wang, J. Lohrman, S. Ren, H. Zhao, *Physical Review B* **2012**, *86*, DOI 10.1103/PhysRevB.86.205417.

[104] B. Schönfeld, J. J. Huang, S. C. Moss, *Acta Crystallographica Section B Structural Science* **1983**, *39*, 404–407, DOI 10.1107/S0108768183002645.

[105] A. Kumar, P. K. Ahluwalia, *Modelling and Simulation in Materials Science and Engineering* **2013**, *21*, 065015, DOI 10.1088/0965-0393/21/6/065015.

[106] A. Eftekhari, *Journal of Materials Chemistry A* **2017**, *5*, 18299–18325, DOI 10.1039/C7TA04268J.

[107] T. Li, G. Galli, *The Journal of Physical Chemistry C* **2007**, *111*, 16192–16196, DOI 10.1021/jp075424v.

[108] W. Ho, J. C. Yu, J. Lin, J. Yu, P. Li, *Langmuir : the ACS journal of surfaces and colloids* **2004**, *20*, 5865–5869, DOI 10.1021/la049838g.

[109] E. Gourmelon, O. Lignier, H. Hadouda, G. Couturier, J. C. Bernède, J. Tedd, J. Pouzet, J. Salardenne, *Solar Energy Materials and Solar Cells* **1997**, *46*, 115–121, DOI 10.1016/S0927-0248(96)00096-7.

[110] Z. Y. Zhu, Y. C. Cheng, U. Schwingenschlögl, *Physical Review B* **2011**, *84*, DOI 10.1103/PhysRevB.84.153402.

[111] Coehoorn, Haas, Dijkstra, Flipse, R. A. de Groot, Wold, *Physical review. B Condensed matter* **1987**, *35*, 6195–6202, DOI 10.1103/physrevb.35.6195.

[112] Coehoorn, Haas, R. A. de Groot, *Physical review. B Condensed matter* **1987**, *35*, 6203–6206, DOI 10.1103/physrevb.35.6203.

[113] A. Splendiani, L. Sun, Y. Zhang, T. Li, J. Kim, C.-Y. Chim, G. Galli, F. Wang, *Nano letters* **2010**, *10*, 1271–1275, DOI 10.1021/nl903868w.

[114] W. Chen, S. Chen, D. C. Qi, X. Y. Gao, A. T. S. Wee, *Journal of the American Chemical Society* **2007**, *129*, 10418–10422, DOI 10.1021/ja071658g.

[115] C. Coletti, C. Riedl, D. S. Lee, B. Krauss, L. Patthey, K. von Klitzing, J. H. Smet, U. Starke, *Physical Review B* **2010**, *81*, DOI 10.1103/PhysRevB.81.235401.

[116] K. F. Mak, K. He, C. Lee, G. H. Lee, J. Hone, T. F. Heinz, J. Shan, *Nature materials* **2013**, *12*, 207–211, DOI 10.1038/nmat3505.

[117] C. Elias, P. Valvin, T. Pelini, A. Summerfield, C. J. Mellor, T. S. Cheng, L. Eaves, C. T. Foxon, P. H. Beton, S. V. Novikov, B. Gil, G. Cassabois, *Nature communications* **2019**, *10*, 2639, DOI 10.1038/s41467-019-10610-5.

[118] G. Cassabois, P. Valvin, B. Gil, *Nature Photonics* **2016**, *10*, 262–266, DOI 10.1038/nphoton.2015.277.

[119] T. Q. P. Vuong, S. Liu, A. van der Lee, R. Cuscó, L. Artús, T. Michel, P. Valvin, J. H. Edgar, G. Cassabois, B. Gil, *Nature materials* **2018**, *17*, 152–158, DOI 10.1038/nmat5048.

[120] T. Q. P. Vuong, G. Cassabois, P. Valvin, V. Jacques, R. Cuscó, L. Artús, B. Gil, *Physical Review B* **2017**, *95*, DOI 10.1103/physrevb.95.045207.

[121] G. Cassabois, P. Valvin, B. Gil, *Physical Review B* **2016**, *93*, DOI 10.1103/physrevb.93.035207.

[122] R. Schuster, C. Habenicht, M. Ahmad, M. Knupfer, B. Büchner, *Physical Review B* **2018**, *97*, DOI 10.1103/physrevb.97.041201.

[123] Blase, Rubio, Louie, Cohen, *Physical review. B Condensed matter* **1995**, *51*, 6868–6875, DOI 10.1103/physrevb.51.6868.

[124] F. Paleari, T. Galvani, H. Amara, F. Ducastelle, A. Molina-Sánchez, L. Wirtz, *2D Materials* **2018**, *5*, 045017, DOI 10.1088/2053-1583/aad586.

[125] P. Beiss, R. Ruthardt, H. Warlimont, *Numerical data and functional relationships in science and technology: New series, Vol. 2*, Springer, Berlin, **2002**, DOI 10.1007/b83029.

[126] K. Watanabe, T. Taniguchi, H. Kanda, *Nature materials* **2004**, *3*, 404–409, DOI 10.1038/nmat1134.

[127] O. A. Ajayi, J. V. Ardelean, G. D. Shepard, J. Wang, A. Antony, T. Taniguchi, K. Watanabe, T. F. Heinz, S. Strauf, X.-Y. Zhu, J. C. Hone, *2D Materials* **2017**, *4*, 031011, DOI 10.1088/2053-1583/aa6aa1.

[128] M. Buscema, G. A. Steele, H. S. J. van der Zant, A. Castellanos-Gomez, *Nano Research* **2014**, *7*, 561–571, DOI 10.1007/s12274-014-0424-0.

[129] C. R. Dean, A. F. Young, I. Meric, C. Lee, L. Wang, S. Sorgenfrei, K. Watanabe, T. Taniguchi, P. Kim, K. L. Shepard, J. Hone, *Nature nanotechnology* **2010**, *5*, 722–726, DOI 10.1038/nnano.2010.172.

[130] D. G. Purdie, N. M. Pugno, T. Taniguchi, K. Watanabe, A. C. Ferrari, A. Lombardo, *Nature communications* **2018**, *9*, 5387, DOI 10.1038/s41467-018-07558-3.

[131] L. Novotny, B. Hecht, *Principles of nano-optics*, Cambridge University Press, Cambridge, **2006**, DOI 10.1017/CBO9780511813535.

[132] B. D. Guenther, D. Steel, *Encyclopedia of Modern Optics*, 2nd ed., Elsevier Science & Technology, San Diego, **2018**.

[133] Zeiss, Highlights from the History of Immersion Objectives.

[134] *Introductory Raman spectroscopy*, 2nd ed., (Eds.: J. R. Ferraro, C. W. Brown, K. Nakamoto), Academic Press, Amsterdam and Boston, **2003**.

[135] R. Saito, M. Hofmann, G. Dresselhaus, A. Jorio, M. S. Dresselhaus, *Advances in Physics* **2011**, *60*, 413–550, DOI 10.1080/00018732.2011.582251.

[136] P. Y. Yu, M. Cardona, *Fundamentals of Semiconductors: Physics and Materials Properties*, 4. ed., Springer-Verlag Berlin Heidelberg, Berlin, Heidelberg, **2010**, DOI 10.1007/978-3-642-00710-1.

[137] D. S. Knight, W. B. White, *Journal of Materials Research* **1989**, *4*, 385–393, DOI 10.1557/JMR.1989.0385.

[138] M. S. Dresselhaus, A. Jorio, A. G. Souza Filho, R. Saito, *Philosophical transactions. Series A Mathematical physical and engineering sciences* **2010**, *368*, 5355–5377, DOI 10.1098/rsta.2010.0213.

[139] C. Georgi, A. Hartschuh, *Applied Physics Letters* **2010**, *97*, 143117, DOI 10.1063/1.3499752.

[140] C. P. Poole, *Electron spin resonance: A comprehensive treatise on experimental techniques*, 2. ed., Dover ed., Dover Publications, Mineola, N.Y, **1996**.

[141] L. Vaisman, H. D. Wagner, G. Marom, *Advances in colloid and interface science* **2006**, *128-130*, 37–46, DOI 10.1016/j.cis.2006.11.007.

[142] A. M. Rao, J. Chen, E. Richter, U. Schlecht, P. C. Eklund, R. C. Haddon, U. D. Venkateswaran, Y. K. Kwon, D. Tománek, *Physical review letters* **2001**, *86*, 3895–3898, DOI 10.1103/PhysRevLett.86.3895.

[143] M. F. Islam, E. Rojas, D. M. Bergey, A. T. Johnson, A. G. Yodh, *Nano letters* **2003**, *3*, 269–273, DOI 10.1021/nl025924u.

[144] S. Iijima, *Nature* **1991**, *354*, 56–58, DOI 10.1038/354056a0.

[145] T. W. Ebbesen, P. M. Ajayan, *Nature* **1992**, *358*, 220–222, DOI 10.1038/358220a0.

[146] T. Guo, P. Nikolaev, A. Thess, D. T. Colbert, R. E. Smalley, *Chemical Physics Letters* **1995**, *243*, 49–54, DOI 10.1016/0009-2614(95)00825-O.

[147] T. Guo, P. Nikolaev, A. G. Rinzler, D. Tomanek, D. T. Colbert, R. E. Smalley, *The Journal of Physical Chemistry* **1995**, *99*, 10694–10697, DOI 10.1021/j100027a002.

[148] O. Smiljanic, B. L. Stansfield, J.-P. Dodelet, A. Serventi, S. Désilets, *Chemical Physics Letters* **2002**, *356*, 189–193, DOI 10.1016/S0009-2614(02)00132-X.

[149] M. José–Yacamán, M. Miki–Yoshida, L. Rendón, J. G. Santiesteban, *Applied Physics Letters* **1993**, *62*, 657–659, DOI 10.1063/1.108857.

[150] Sigma Aldrich documentation, Characterization and Properties of CoMoCAT® Carbon Nanotubes.

[151] H. Ozawa, N. Ide, T. Fujigaya, Y. Niidome, N. Nakashima, *Chemistry Letters* **2011**, *40*, 239–241, DOI 10.1246/cl.2011.239.

[152] K. S. Mistry, B. A. Larsen, J. L. Blackburn, *ACS nano* **2013**, *7*, 2231–2239, DOI 10.1021/nn305336x.

[153] A. Nish, J.-Y. Hwang, J. Doig, R. J. Nicholas, *Nature nanotechnology* **2007**, *2*, 640–646, DOI 10.1038/nnano.2007.290.

[154] W. Gomulya, J. Gao, M. A. Loi, *The European Physical Journal B* **2013**, *86*, DOI 10.1140/epjb/e2013-40707-9.

[155] J. Gao, M. A. Loi, E. J. F. de Carvalho, M. C. Dos Santos, *ACS nano* **2011**, *5*, 3993–3999, DOI 10.1021/nn200564n.

[156] J. Chen, H. Liu, W. A. Weimer, M. D. Halls, D. H. Waldeck, G. C. Walker, *Journal of the American Chemical Society* **2002**, *124*, 9034–9035, DOI 10.1021/ja026104m.

[157] Kerstin Müller, Dissertation, Julius-Maximilians-Universität, Würzburg, **2020**.

[158] O. Matarredona, H. Rhoads, Z. Li, J. H. Harwell, L. Balzano, D. E. Resasco, *The journal of physical chemistry. B* **2003**, *107*, 13357–13367, DOI 10.1021/jp0365099.

[159] S. L. Peshkovsky, A. S. Peshkovsky, *Ultrasonics Sonochemistry* **2008**, *15*, 618–628, DOI 10.1016/j.ultsonch.2007.07.006.

[160] Y. Y. Huang, E. M. Terentjev, *Polymers* **2012**, *4*, 275–295, DOI 10.3390/polym4010275.

[161] M. D. Rossell, C. Kuebel, G. Ilari, F. Rechberger, F. J. Heiligtag, M. Niederberger, D. Koziej, R. Erni, *Carbon* **2013**, *61*, 404–411, DOI 10.1016/j.carbon.2013.05.024.

[162] A. Akyüz, H. Catalgil-Giz, A. T. Giz, *Macromolecular Chemistry and Physics* **2008**, *209*, 801–809, DOI 10.1002/macp.200700533.

[163] A. M. Basedow, K. H. Ebert in *Physical Chemistry*, (Eds.: H.-J. Cantow, G. Dall'Asta, K. Dušek, J. D. Ferry, H. Fujita, M. Gordon, W. Kern, G. Natta, S. Okamura, C. G. Overberger, T. Saegusa, G. V. Schulz, W. P. Slichter, J. K. Stille), Advances in Polymer Science, Springer, Berlin and Heidelberg, **1977**, pp. 83–148, DOI 10.1007/3-540-07942-4{\textunderscore}6.

[164] A. V. Naumov, D. A. Tsyboulski, S. M. Bachilo, R. B. Weisman, *Chemical Physics* **2013**, *422*, 255–263, DOI 10.1016/j.chemphys.2012.12.033.

[165] A. Graf, Y. Zakharko, S. P. Schießl, C. Backes, M. Pfohl, B. S. Flavel, J. Zaumseil, *Carbon* **2016**, *105*, 593–599, DOI 10.1016/j.carbon.2016.05.002.

[166] F. Schöppler, C. Mann, T. C. Hain, F. M. Neubauer, G. Privitera, F. Bonaccorso, D. Chu, A. C. Ferrari, T. Hertel, *The Journal of Physical Chemistry C* **2011**, *115*, 14682–14686, DOI 10.1021/jp205289h.

[167] Tilman Hain, Dissertation, Julius-Maximilians-Universität, Würzburg, **2015**.

[168] K. S. LARSSON, *Studies on the closure of the secondary palate. V. Attempts to study the teratogenic action of cortisone in mice*, *Vol. 20*, **1962**, DOI 10.3109/00016356209167174.

[169] A. V. Mohod, P. R. Gogate, *Ultrasonics Sonochemistry* **2011**, *18*, 727–734, DOI 10.1016/j.ultsonch.2010.11.002.

[170] B. Miller, A. Steinhoff, B. Pano, J. Klein, F. Jahnke, A. Holleitner, U. Wurstbauer, *Nano letters* **2017**, *17*, 5229–5237, DOI 10.1021/acs.nanolett.7b01304.

[171] M. Baranowski, A. Surrente, L. Klopotowski, J. M. Urban, N. Zhang, D. K. Maude, K. Wiwatowski, S. Mackowski, Y. C. Kung, D. Dumcenco, A. Kis, P. Plochocka, *Nano letters* **2017**, *17*, 6360–6365, DOI 10.1021/acs.nanolett.7b03184.

[172] P. Nagler, M. V. Ballottin, A. A. Mitioglu, F. Mooshammer, N. Paradiso, C. Strunk, R. Huber, A. Chernikov, P. C. M. Christianen, C. Schüller, T. Korn, *Nature communications* **2017**, *8*, 1551, DOI 10.1038/s41467-017-01748-1.

[173] J. Kiemle, F. Sigger, M. Lorke, B. Miller, K. Watanabe, T. Taniguchi, A. Holleitner, U. Wurstbauer, *Physical Review B* **2020**, *101*, DOI 10.1103/PhysRevB.101.121404.

[174] C. Jiang, W. Xu, A. Rasmita, Z. Huang, K. Li, Q. Xiong, W.-B. Gao, *Nature communications* **2018**, *9*, 753, DOI 10.1038/s41467-018-03174-3.

[175] C. Zhang, C. Gong, Y. Nie, K.-A. Min, C. Liang, Y. J. Oh, H. Zhang, W. Wang, S. Hong, L. Colombo, R. M. Wallace, K. Cho, *2D Materials* **2017**, *4*, 015026, DOI 10.1088/2053-1583/4/1/015026.

[176] P. Rivera, J. R. Schaibley, A. M. Jones, J. S. Ross, S. Wu, G. Aivazian, P. Klement, K. Seyler, G. Clark, N. J. Ghimire, J. Yan, D. G. Mandrus, W. Yao, X. Xu, *Nature communications* **2015**, *6*, 6242, DOI 10.1038/ncomms7242.

[177] J. Kang, S. Tongay, J. Zhou, J. Li, J. Wu, *Applied Physics Letters* **2013**, *102*, 012111, DOI 10.1063/1.4774090.

[178] K. Kośmider, J. Fernández-Rossier, *Physical Review B* **2013**, *87*, DOI 10.1103/PhysRevB.87.075451.

[179] H. Terrones, F. López-Urías, M. Terrones, *Scientific reports* **2013**, *3*, 1549, DOI 10.1038/srep01549.

[180] P. K. Nayak, Y. Horbatenko, S. Ahn, G. Kim, J.-U. Lee, K. Y. Ma, A.-R. Jang, H. Lim, D. Kim, S. Ryu, H. Cheong, N. Park, H. S. Shin, *ACS nano* **2017**, *11*, 4041–4050, DOI 10.1021/acsnano.7b00640.

[181] F. Ceballos, M. Z. Bellus, H.-Y. Chiu, H. Zhao, *ACS nano* **2014**, *8*, 12717–12724, DOI 10.1021/nn505736z.

[182] E. M. Alexeev, A. Catanzaro, O. V. Skrypka, P. K. Nayak, S. Ahn, S. Pak, J. Lee, J. I. Sohn, K. S. Novoselov, H. S. Shin, A. I. Tartakovskii, *Nano letters* **2017**, *17*, 5342–5349, DOI 10.1021/acs.nanolett.7b01763.

[183] D. H. Luong, H. S. Lee, G. P. Neupane, S. Roy, G. Ghimire, J. H. Lee, Q. an Vu, Y. H. Lee, *Advanced Materials* **2017**, *29*, 1701512, DOI 10.1002/adma.201701512.

[184] F. Ceballos, M. Z. Bellus, H.-Y. Chiu, H. Zhao, *Nanoscale* **2015**, *7*, 17523–17528, DOI 10.1039/C5NR04723D.

[185] K. Zhang, T. Zhang, G. Cheng, T. Li, S. Wang, W. Wei, X. Zhou, W. Yu, Y. Sun, P. Wang, D. Zhang, C. Zeng, X. Wang, W. Hu, H. J. Fan, G. Shen, X. Chen, X. Duan, K. Chang, N. Dai, *ACS nano* **2016**, *10*, 3852–3858, DOI 10.1021/acsnano.6b00980.

[186] S. Mouri, W. Zhang, D. Kozawa, Y. Miyauchi, G. Eda, K. Matsuda, *Nanoscale* **2017**, *9*, 6674–6679, DOI 10.1039/C7NR01598D.

[187] M. Z. Bellus, F. Ceballos, H.-Y. Chiu, H. Zhao, *ACS nano* **2015**, *9*, 6459–6464, DOI 10.1021/acsnano.5b02144.

[188] P. Nagler, G. Plechinger, M. V. Ballottin, A. Mitioglu, S. Meier, N. Paradiso, C. Strunk, A. Chernikov, P. C. M. Christianen, C. Schüller, T. Korn, *2D Materials* **2017**, *4*, 025112, DOI 10.1088/2053-1583/aa7352.

[189] X. Hong, J. Kim, S.-F. Shi, Y. Zhang, C. Jin, Y. Sun, S. Tongay, J. Wu, Y. Zhang, F. Wang, *Nature Nanotechnology* **2014**, *9*, 682–686, DOI 10.1038/nnano.2014.167.

[190] NKT, SuperK Exteme Product Guide.

[191] A. Castellanos-Gomez, M. Buscema, R. Molenaar, V. Singh, L. Janssen, H. S. J. van der Zant, G. A. Steele, *2D Materials* **2014**, *1*, 011002, DOI 10.1088/2053-1583/1/1/011002.

[192] *Astronomical Optics*, Elsevier, **2000**, DOI 10.1016/B978-0-12-629810-9.X5000-2.

[193] Z. Liu, M. Amani, S. Najmaei, Q. Xu, X. Zou, W. Zhou, T. Yu, C. Qiu, A. G. Birdwell, F. J. Crowne, R. Vajtai, B. I. Yakobson, Z. Xia, M. Dubey, P. M. Ajayan, J. Lou, *Nature communications* **2014**, *5*, 5246, DOI 10.1038/ncomms6246.

[194] S. Tongay, J. Zhou, C. Ataca, J. Liu, J. S. Kang, T. S. Matthews, L. You, J. Li, J. C. Grossman, J. Wu, *Nano letters* **2013**, *13*, 2831–2836, DOI 10.1021/nl4011172.

[195] W. Bao, N. J. Borys, C. Ko, J. Suh, W. Fan, A. Thron, Y. Zhang, A. Buyanin, J. Zhang, S. Cabrini, P. D. Ashby, A. Weber-Bargioni, S. Tongay, S. Aloni, D. F. Ogletree, J. Wu, M. B. Salmeron, P. J. Schuck, *Nature communications* **2015**, *6*, 7993, DOI 10.1038/ncomms8993.

[196] A. M. van der Zande, P. Y. Huang, D. A. Chenet, T. C. Berkelbach, Y. You, G.-H. Lee, T. F. Heinz, D. R. Reichman, D. A. Muller, J. C. Hone, *Nature materials* **2013**, *12*, 554–561, DOI 10.1038/nmat3633.

[197] L. V. Keldysh, *Soviet Journal of Experimental and Theoretical Physics Letters* **1979**, *29*, 658.

[198] N. S. Rytova, Screened potential of a point charge in a thin film, **2018**.

[199] Hartleb, Holger Edgar Heinz Erich, PhD thesis, Julius-Maximilians-Universität, Würzburg, **2015**.

[200] C. H. Lui, Z. Ye, C. Ji, K.-C. Chiu, C.-T. Chou, T. I. Andersen, C. Means-Shively, H. Anderson, J.-M. Wu, T. Kidd, Y.-H. Lee, R. He, *Physical Review B* **2015**, *91*, DOI 10.1103/PhysRevB.91.165403.

[201] R. W. Keyes, *Proceedings of the IEEE* **2001**, *89*, 227–239, DOI 10.1109/5.915372.

[202] V. Jašinskas, F. Oberndorfer, V. Pakštas, T. Hertel, V. Gulbinas, *The Journal of Physical Chemistry C* **2018**, *122*, 16424–16430, DOI 10.1021/acs.jpcc.8b04672.

[203] Imge Namal, **2017**.

[204] S. M. Kim, J. H. Jang, K. K. Kim, H. K. Park, J. J. Bae, W. J. Yu, I. H. Lee, G. Kim, D. D. Loc, U. J. Kim, E.-H. Lee, H.-J. Shin, J.-Y. Choi, Y. H. Lee, *Journal of the American Chemical Society* **2009**, *131*, 327–331, DOI 10.1021/ja807480g.

[205] C. M. Aguirre, P. L. Levesque, M. Paillet, F. Lapointe, B. C. St-Antoine, P. Desjardins, R. Martel, *Advanced Materials* **2009**, *21*, 3087–3091, DOI 10.1002/adma.200900550.

[206] A. J. Ferguson, O. G. Reid, S. U. Nanayakkara, R. Ihly, J. L. Blackburn, *The journal of physical chemistry letters* **2018**, *9*, 6864–6870, DOI 10.1021/acs.jpclett.8b03074.

[207] F. Mousty, P. Ostoja, L. Passari, *Journal of Applied Physics* **1974**, *45*, 4576–4580, DOI 10.1063/1.1663091.

[208] A. J. Ferguson, A.-M. Dowgiallo, D. J. Bindl, K. S. Mistry, O. G. Reid, N. Kopidakis, M. S. Arnold, J. L. Blackburn, *Physical Review B* **2015**, *91*, DOI 10.1103/PhysRevB.91.245311.

[209] H. Hu, B. Zhao, M. A. Hamon, K. Kamaras, M. E. Itkis, R. C. Haddon, *Journal of the American Chemical Society* **2003**, *125*, 14893–14900, DOI 10.1021/ja0356737.

[210] M. T. Auth, PhD thesis, Universität Würzburg, **2020**, DOI 10.25972/OPUS-18951.

[211] H. Farhat, H. Son, G. G. Samsonidze, S. Reich, M. S. Dresselhaus, J. Kong, *Physical review letters* **2007**, *99*, 145506, DOI 10.1103/PhysRevLett.99.145506.

[212] K. Matsuda, Y. Miyauchi, T. Sakashita, Y. Kanemitsu, *Physical Review B* **2010**, *81*, DOI 10.1103/PhysRevB.81.033409.

[213] M. Jaiswal, W. Wang, K. A. Shiral Fernando, Y.-P. Sun, R. Menon, *Journal of Physics: Condensed Matter* **2007**, *19*, 446006, DOI 10.1088/0953-8984/19/44/446006.

[214] M. Salvato, M. Cirillo, M. Lucci, S. Orlanducci, I. Ottaviani, M. L. Terranova, F. Toschi, *Physical review letters* **2008**, *101*, 246804, DOI 10.1103/PhysRevLett.101.246804.

[215] M. Rother, S. P. Schießl, Y. Zakharko, F. Gannott, J. Zaumseil, *ACS applied materials & interfaces* **2016**, *8*, 5571–5579, DOI 10.1021/acsami.6b00074.

[216] M. Brohmann, F. J. Berger, M. Matthiesen, S. P. Schießl, S. Schneider, J. Zaumseil, *ACS nano* **2019**, *13*, 7323–7332, DOI 10.1021/acsnano.9b03699.

[217] S. Ravi, A. B. Kaiser, C. W. Bumby, *physica status solidi (b)* **2013**, *250*, 1463–1467, DOI 10.1002/pssb.201300033.

[218] D. Amarasinghe Vithanage, A. Devižis, V. Abramavičius, Y. Infahsaeng, D. Abramavičius, R. C. I. MacKenzie, P. E. Keivanidis, A. Yartsev, D. Hertel, J. Nelson, V. Sundström, V. Gulbinas, *Nature communications* **2013**, *4*, 2334, DOI 10.1038/ncomms3334.

[219] A. Devizis, A. Serbenta, K. Meerholz, D. Hertel, V. Gulbinas, *Physical review letters* **2009**, *103*, 027404, DOI 10.1103/PhysRevLett.103.027404.

[220] A. Devizis, K. Meerholz, D. Hertel, V. Gulbinas, *Physical Review B* **2010**, *82*, DOI 10.1103/PhysRevB.82.155204.

[221] S. Chen, K. F. Li, G. Li, K. W. Cheah, S. Zhang, *Light: Science & Applications* **2019**, *8*, 17, DOI 10.1038/s41377-019-0128-z.

[222] M. S. Arnold, J. D. Zimmerman, C. K. Renshaw, X. Xu, R. R. Lunt, C. M. Austin, S. R. Forrest, *Nano letters* **2009**, *9*, 3354–3358, DOI 10.1021/nl901637u.

[223] D. M. Guldi, R. D. Costa, *The journal of physical chemistry letters* **2013**, *4*, 1489–1501, DOI 10.1021/jz4001714.

[224] I. A. Levitsky, W. B. Euler, *Applied Physics Letters* **2003**, *83*, 1857–1859, DOI 10.1063/1.1606099.

[225] A. Eckstein, V. Bertašius, V. Jašinskas, I. Namal, T. Hertel, V. Gulbinas, *Nanoscale* **2017**, *9*, 12441–12448, DOI 10.1039/c7nr03813e.

[226] A.-M. Dowgiallo, K. S. Mistry, J. C. Johnson, J. L. Blackburn, *ACS nano* **2014**, *8*, 8573–8581, DOI 10.1021/nn503271k.

List of Figures

List of Tables

Acknowledgements

No project is truly the work of a single person. We all build our success on those who came before us. We all need help every once in a while. We all educate each other about things we were ignorant before. Therefore the following chapter is dedicated to the many people who helped me over the course of my dissertation.

My thanks go to Prof. Dr. ***Tobias Hertel*** for giving me the opportunity to work with his group and provide me with a position as a Phd-student.

Secondly I'd like to express my gratitude ***Friedrich Schöppler***. I suspect there is a Florian shaped hole in Freddis visitor chair, from the countless times I came by to consult with him.

I would like to especially thank ***Pascal Kunkel***, who shared my office for the entire duration of both of our time in the group. Many thanks for listening, constructive discussion and bravely enduring the wide variety of poor jokes about your size.

My gratitude also goes to ***Kolja Thonik*** and ***Lucas Fuhl*** likewise shared the office with me and Pascal and contributed to a relaxed and productive work atmosphere. (Although I'm not sure if Pascal would always agree)

Special thanks also go to ***Simon Kießling*** for helping me with the difficult process of sample preparation for two-dimensional materials. As with most scientific endeavors, it sounds easy but it most certainly wasn't. Going beyond the scientific help I would also like to thank him for the moral support in the difficult last experimental weeks of my dissertation.

I also owe thanks to ***Kerstin Müller*** for being the genuine optimist that she is. Always upbeat and ready to smile, she could even cheer up a embittered cynic like me.

I would like to thank ***Matthias Kastner*** for introducing me to fluorescence microscopy and teaching me how to make IgorPro do what it is supposed to do. He never failed to give good advice how to solve the various IT problems and many of his procedures formed the basis for my own developments.

My thanks also go to ***Andreas Sperlich*** and ***Michael Auth***. After disappointing experiences with a previous cooperation I was initially not excited about another cooperation project. I will gladly admit that I was wrong and learned that, if properly executed, cooperations can be educational, productive and fun. To a large extent that was thanks to the optimism and competence of these two scientists.

Often unjustly overlooked I would like to thank our ***technical staff***: ***Sabine Stahl***, ***Sabine Fuchs*** and ***Belinda Böhm***. ***Sabine Stahl*** also deserves credit for organizing events of our group. Many of those helped form the team spirit which is on of this group's biggest strengths.

I would also like to thank the ***workshop and electronics*** departments with all its personnel, who always helped realizing (and usually improving) the ideas me and the other scientists come up with. Things would certainly have been a lot harder and a lot more time-consuming without their help.

Special thanks also go the my family who was always supportive, especially towards the end of the dissertation and the tougher and more stressful periods within.